

POLITECNICO DI TORINO

Master's degree in Mechanical Engineering

Master's thesis

**Development of a torque-vectoring
logic for a hybrid vehicle**



Academic supervisors

Prof. Alessandro Vigliani

Ing. Antonio Tota

Company supervisors

Ing. Salvatore Calanna

Ing. Claudio Ricci

Author

Vincenzo Sorrentino

Academic year 2019/2020

Alla mia famiglia

ABSTRACT

This master thesis deals with a torque-vectoring (TV) structure implemented on a hybrid vehicle, a project of *Danisi Engineering* company (Nichelino, Torino, Italy) where this work was carried out. The powertrain of this car is an All-Wheel-Drive (AWD): at the front each wheel is connected to an on-board electric motor, while at the rear there is an internal combustion engine (ICE).

Three driving modes are available, each of them designed to improve the vehicle's behaviour compared to its passive configuration: in *Normal* mode, identical steady state action and better dynamic behaviour are obtained, in *Sport* greater performance is achieved in both stationary and transient conditions and in *Wet* stability and safety are guaranteed with low friction.

At the same time, the control is organized in three parts. In the *reference generator (RG)* the objectives of each driving configuration are translated into a specific understeer characteristic. In the *high level controller (HLC)* from the error of the control variable in a proportional-integral (PI) controller a yaw moment is generated, which is exploited to manage the torque allocation to the wheels in the *low level controller (LLC)*.

The operation of the TV was verified by means of steady state and transient numerical simulations, carrying out a co-simulation between VI-CarRealTime (VI-CRT) and MATLAB/Simulink, respectively where the vehicle model and the control were built.

Contents

| | |
|--|------------|
| List of figures | vii |
| List of tables | xii |
| 1. Introduction..... | 1 |
| 1.1. Thesis structure | 2 |
| 2. Vehicle model | 4 |
| 2.1. 14-DOF vehicle model | 4 |
| 2.2. Ride model | 5 |
| 2.3. Lateral dynamics | 7 |
| 2.3.1. <i>Single track model</i> | 7 |
| 2.3.2. <i>Double track model</i> | 10 |
| 2.4. Tire characteristics..... | 14 |
| 2.4.1. <i>Pacejka's Magic Formula</i> | 17 |
| 2.5. Handling diagrams | 18 |
| 3. VI-CarRealTime..... | 21 |
| 3.1. Environment | 21 |
| 3.2. Virtual model vehicle | 22 |
| 3.2.1. <i>Reference system and model configuration</i> | 22 |
| 3.2.2. <i>Body</i> | 24 |
| 3.2.3. <i>Powertrain</i> | 25 |
| 3.2.4. <i>Brakes</i> | 27 |
| 3.2.5. <i>Wheels</i> | 27 |

| | |
|---|-----------|
| 3.2.6. <i>Suspensions</i> | 28 |
| 3.3. Test mode | 31 |
| 3.4. Co-simulation VI-CRT and Simulink | 32 |
| 4. Torque-vectoring | 35 |
| 4.1. History and state of art..... | 35 |
| 4.2. Control strategies | 38 |
| 5. Control system | 42 |
| 5.1. Reference generator | 43 |
| 5.2. High level controller | 49 |
| 5.3. Low level controller | 50 |
| 5.3.1. <i>Front</i> | 51 |
| 5.3.2. <i>Rear</i> | 54 |
| 6. Simulation results | 56 |
| 6.1. Ramp steer..... | 56 |
| 6.2. Step steer..... | 64 |
| 6.3. Sweep steer..... | 68 |
| 6.4. PowerOn on cornering | 72 |
| 6.5. Braking in turn..... | 79 |
| 7. Conclusions | 85 |
| 7.1. Future works..... | 86 |
| Acknowledgments | 88 |
| Bibliography | 89 |

List of figures

| | |
|--|----|
| Figure 2.1: DOF of the vehicle model (adapted from [1])..... | 4 |
| Figure 2.2: 7 DOF of ride model [2] | 5 |
| Figure 2.3: Cornering of a bicycle model [3]..... | 8 |
| Figure 2.4: Change of SWA with speed [3]..... | 10 |
| Figure 2.5: 7 DOF of double track model (adapted from [5])..... | 10 |
| Figure 2.6: Pitch motion due to longitudinal acceleration [1]..... | 12 |
| Figure 2.7: Free body diagram of the sprung mass [4] | 12 |
| Figure 2.8: Lateral load transfer (adapted from [4])..... | 13 |
| Figure 2.9: Wheel free body diagram [4]..... | 13 |
| Figure 2.10: Nomenclature and reference system of the tire [4]..... | 14 |
| Figure 2.11: Effect of α and F_z on lateral force F_y [4]..... | 15 |
| Figure 2.12: Cornering stiffness C_k (left) and C_α (right) in function of vertical load F_z [4] | 16 |
| Figure 2.13: Influence of k and μ on longitudinal force F_x [4]..... | 16 |
| Figure 2.14: Influence of k and α on longitudinal F_x and lateral F_y forces [4]..... | 17 |
| Figure 2.15: Curve produced by the original sine version of the Magic Formula [6]..... | 18 |
| Figure 2.16: Example of understeer characteristic in steady state [7] | 19 |
| Figure 2.17: Sideslip angle in a low-speed turn (left) and a high-speed turn (right) [3] | 19 |
| Figure 2.18: Example of sideslip angle characteristic in steady state [7]..... | 20 |
| Figure 2.19: Example of roll angle characteristic in steady state [7] | 20 |
| Figure 3.1: VI-CRT reference frames [8]..... | 23 |
| Figure 3.2: VI-CRT <i>Build Mode</i> and subsystem definition | 24 |

| | |
|---|----|
| Figure 3.3: Driveline layout | 25 |
| Figure 3.4: Rear engine and front electric motor torque map | 26 |
| Figure 3.5: Calipers drawing to the front (at left) and to the rear (at right) [9] | 27 |
| Figure 3.6: Damper characteristic | 29 |
| Figure 3.7: PWT suspension test | 29 |
| Figure 3.8: Toe and camber angle [8]..... | 31 |
| Figure 3.9: VI-CRT <i>Test Mode</i> | 31 |
| Figure 3.10: VI-CRT <i>Event Builder</i> | 32 |
| Figure 3.11: Block of VI-CRT in Simulink [8] | 33 |
| Figure 3.12: Window for <i>vicrt_inputfile</i> [8]..... | 33 |
| Figure 3.13: Window to select I/O channels [8]..... | 34 |
| Figure 4.1: Examples of vehicle layouts with one to four electric powertrains [12] | 36 |
| Figure 4.2: Active safety activation using ABS, TCS and ESC. At right also including TV [14]..... | 37 |
| Figure 4.3: Typical structure of a TV controller (adapted from [15])..... | 38 |
| Figure 4.4: Potential modifications of vehicle understeer characteristic achievable through TV [18] | 39 |
| Figure 4.5: Scheme of TV application for a 4WD FEV with individual onboard electric motors [11] | 40 |
| Figure 5.1: TV controller Simulink model | 42 |
| Figure 5.2: Steering pad on the passive vehicle – Lateral acceleration and longitudinal velocity..... | 45 |
| Figure 5.3: Ramp steer on the passive vehicle – Dynamic understeer characteristic | 45 |
| Figure 5.4: Desired dynamic understeer characteristics | 47 |
| Figure 5.5: Reference generator..... | 47 |

| | |
|--|----|
| Figure 5.6: Map of the desired yaw rate – Normal mode..... | 48 |
| Figure 5.7: Comparison between map of the desired yaw rate | 48 |
| Figure 5.8: Scheme of vehicle in various scenarios and adopted sign conventions [22] | 49 |
| Figure 5.9: High level controller..... | 50 |
| Figure 5.10: Low level controller..... | 51 |
| Figure 5.11: Front – Low level controller | 51 |
| Figure 5.12: Drivability controller – Front – Low level controller..... | 52 |
| Figure 5.13: The comparison of understeer (at left) and oversteer (at right) manoeuvre without (in blue) and with (in green) TV control system (adapted from [19]) | 53 |
| Figure 5.14: Rear yaw moment calculation – Front – Low level controller..... | 54 |
| Figure 5.15: Rear – Low level controller..... | 55 |
| Figure 5.16: Braking pressure – Rear – Low level controller..... | 55 |
| Figure 6.1: Ramp steer – SWA and longitudinal velocity..... | 57 |
| Figure 6.2: Ramp steer – Yaw rate and error | 57 |
| Figure 6.3: Ramp steer – Yaw moment and electric motors torque | 58 |
| Figure 6.4: Ramp steer – Dynamic understeer characteristic..... | 60 |
| Figure 6.5: Ramp steer – Trajectory | 60 |
| Figure 6.6: Ramp steer – Sideslip, roll and yaw angle characteristic..... | 61 |
| Figure 6.7: Ramp steer – Longitudinal forces..... | 62 |
| Figure 6.8: Ramp steer – Comparison between desired and actual yaw moment..... | 62 |
| Figure 6.9: Ramp steer – Lateral forces | 63 |
| Figure 6.10: Step steer – SWA and longitudinal velocity | 64 |
| Figure 6.11: Step steer – Sideslip angle | 64 |
| Figure 6.12: Step steer – Yaw rate and error..... | 65 |

| | |
|---|----|
| Figure 6.13: Step steer – Yaw moment and electric motors torque | 66 |
| Figure 6.14: Step steer – Rear braking torques | 67 |
| Figure 6.15: Step steer – Comparison between desired and actual yaw moment..... | 67 |
| Figure 6.16: Sweep steer – SWA and longitudinal velocity | 68 |
| Figure 6.17: Sweep steer – Lateral acceleration..... | 69 |
| Figure 6.18: Sweep steer – Sideslip angle..... | 69 |
| Figure 6.19: Sweep steer – Yaw rate and error..... | 70 |
| Figure 6.20: Sweep steer – Yaw moment and electric motors torque | 71 |
| Figure 6.21: Sweep steer – Rear braking torques | 71 |
| Figure 6.22: Sweep steer – Comparison between desired and actual yaw moment..... | 72 |
| Figure 6.23: PowerOn on cornering – SWA and driver throttle demand | 73 |
| Figure 6.24: PowerOn on cornering – Longitudinal velocity and acceleration | 73 |
| Figure 6.25: PowerOn on cornering – Sideslip angle | 74 |
| Figure 6.26: PowerOn on cornering – Trajectory and lateral acceleration | 75 |
| Figure 6.27: PowerOn on cornering – Yaw rate and error | 76 |
| Figure 6.28: PowerOn on cornering – Yaw moment and electric motors torque..... | 77 |
| Figure 6.29: PowerOn on cornering – Electric motors speed | 77 |
| Figure 6.30: PowerOn on cornering – Rear braking torques..... | 78 |
| Figure 6.31: PowerOn on cornering – Comparison between desired and actual yaw moment..... | 78 |
| Figure 6.32: Braking in turn – SWA and driver brake demand..... | 79 |
| Figure 6.33: Braking in turn – Longitudinal velocity and acceleration | 80 |
| Figure 6.34: Braking in turn – Sideslip angle..... | 80 |
| Figure 6.35: Braking in turn – Yaw rate and error..... | 81 |

| | |
|--|----|
| Figure 6.36: Braking in turn – Trajectory and lateral acceleration | 81 |
| Figure 6.37: Braking in turn – Yaw moment and electric motors torque | 82 |
| Figure 6.38: Braking in turn – Braking torques | 83 |
| Figure 6.39: Braking in turn – Comparison between desired and actual yaw moment. | 84 |

List of tables

| | |
|--|----|
| Table 3.1: Sprung mass properties..... | 24 |
| Table 3.2: Position sensors, passengers and fuel..... | 25 |
| Table 3.3: Engine and motors data..... | 26 |
| Table 3.4: Brake specifics..... | 27 |
| Table 3.5: Unsprung mass data | 28 |
| Table 3.6: Pacejka tire model scaling coefficients | 28 |
| Table 3.7: Suspension properties..... | 30 |
| Table 5.1: Understeer characteristic parameters for each driving mode..... | 46 |
| Table 6.1: Ramp steer – Resulting dynamic understeer gradient..... | 61 |
| Table 6.2: Sweep steer – Parameters of the manoeuvre..... | 68 |

1. Introduction

The automotive world has always been in constant evolution, influenced by new technological discoveries, market demands and stringent regulations concerning mainly polluting emissions and consumption.

A sign of continuous innovation are the electronic systems present on the vehicles: these not only monitor and inform about the state of the car while driving, but can also give active assistance to the driver both to prevent accidents and to improve the dynamic behaviour of the vehicle. Instead, to reduce environmental and efficiency problems, vehicles with electric motors are the most important alternative to those equipped with internal combustion engines (ICE). Today there are not only electric vehicles (EV), but also hybrid EV in order not to lose the performance of the ICE and overcome the issues of the batteries (autonomy and recharging).

Regardless of the powertrain structure, the implementation of electric motors offers the possibility of tuning the vehicle dynamic characteristics in steady state and transient conditions because of their intrinsic high controllability. If several motors are present, each of them can be independently controlled with a different torque request. Torque-vectoring (TV) exploits this advantage, i.e. it generates different torques between the wheels of the same axle starting from a certain yaw moment.

The use of electric motors is only one way to get TV: the alternatives are represented by expensive active differentials or the braking system. An active system based on brakes is already available on the market: Electronic Stability Control (ESC). When the ESC detects a loss of steering control, it generates a yaw moment via the brake effect so that the driver takes the desired curve. However, this action only leads to an improvement in vehicle safety, while the intervention fields of the TV also concern all aspects of lateral dynamics, as well as being a more energy efficient solution.

This thesis focuses on the design of a TV logic to be implemented on an All-Wheel-Drive (AWD) hybrid vehicle, consisting of an ICE positioned at the rear and two electric motors connected to the front wheels. The control provides three different configurations, which can be activated on board by the driver. Each of these pursues a different objective: the *Normal* mode guarantees the same behaviour in steady state and improves that in transient, the *Sport* position increases performance in all conditions and the *Wet* version ensures stability and safety in low grip.

1.1. Thesis structure

This work is structured as follows.

- Chapter 2 illustrates the dynamic model of the 14 DOF vehicle, whose equations include two theories: ride model and double track model, derived from the bicycle model. Furthermore, considerations on tire behaviour and handling parameters are reported.
- Chapter 3 presents the environment of VI-CarRealTime (VI-CRT), the software where the virtual vehicle was developed. Subsequently, the specifications of the car were detailed, in the various subsystems of the *Build mode*. In the last part the operation of the co-simulation between VI-CRT and MATLAB/Simulink was described. In Simulink the TV control has been virtually realized.
- Chapter 4 devotes entirely to TV. First the evolution of technology from when it was conceived to today is narrated, after the various TV strategies are outlined, based on the objectives to be realized and the layout of the vehicle.
- Chapter 5 shows the Simulink model of the TV based on the hybrid vehicle mentioned above. The system consists of three parts: in the *reference generator (RG)* the desired trajectory is established, in the *high level controller (HLC)* the corrective action is calculated and in the *low level controller (LLC)* the wheel torques are differentiated.

- Chapter 6 reports the results of the numerical simulations carried out with the co-simulation. The TV was tested in the various driving modes with manoeuvres both steady state and transient, at constant speed and variable longitudinal acceleration.
- Chapter 7 summarizes the objectives and results achieved in this thesis, providing an outlook for possible future works.

2. Vehicle model

The design of an accurate yaw moment control system requires the description of an exhaustive vehicle dynamic model. In this chapter first it is reported a description of degrees of freedom (DOF): 14-DOF are used, as in VI-CarRealTime. Clearly, one with more DOF could also be chosen but the more complex model is not always the most appropriate, it depends on the context. Later motion equations will be detailed, applying two theories: *ride model* and *double track model*. Moreover, it will be explained the main tire characteristics: their modelling is essential because from the contact of the wheels with the road, forces and moments develop to move the car. Finally, the handling diagrams will be illustrated, helpful for analysing the lateral performance of the vehicle.

2.1. 14-DOF vehicle model

The 14-DOF describe the dynamic behaviour of a simplified car and consists of five rigid parts: one is the vehicle body (sprung mass) and the other four are the wheels (unsprung mass).

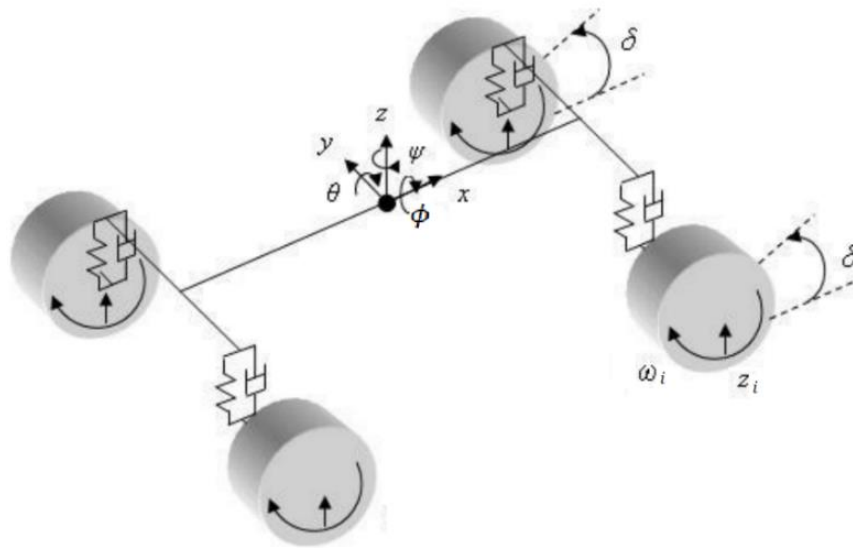


Figure 2.1: DOF of the vehicle model (adapted from [1])

As it is shown in Figure 2.1, the vehicle body has 6 DOF that allows it to displace in the longitudinal (x), lateral (y) and vertical direction (z) as well as to roll (θ), pitch (ϕ) and yaw (ψ). Each wheel has 2 DOF: one allows it to move in vertical direction respect to the vehicle body (z_i) and the other grants it to rotate around the y axle (ω_i) [1].

2.2. Ride model

This theory has 7 DOF: the vehicle body comprises 3 DOF consisting of vertical, roll and pitch motion, while the remaining 4 DOF contain of vertical displacement of each wheel; indeed, there is a spring and a damper at each corner in Figure 2.2.

There are several assumptions made in this model. The vehicle aerodynamic effect is neglected and is also assumed to be rigid where the load transfer from one point to another is hundred percent effective. Tire stiffness, spring stiffness and damper coefficient are also assumed to be constant throughout the simulation process. The road is assumed to be level except for road disturbance [2].

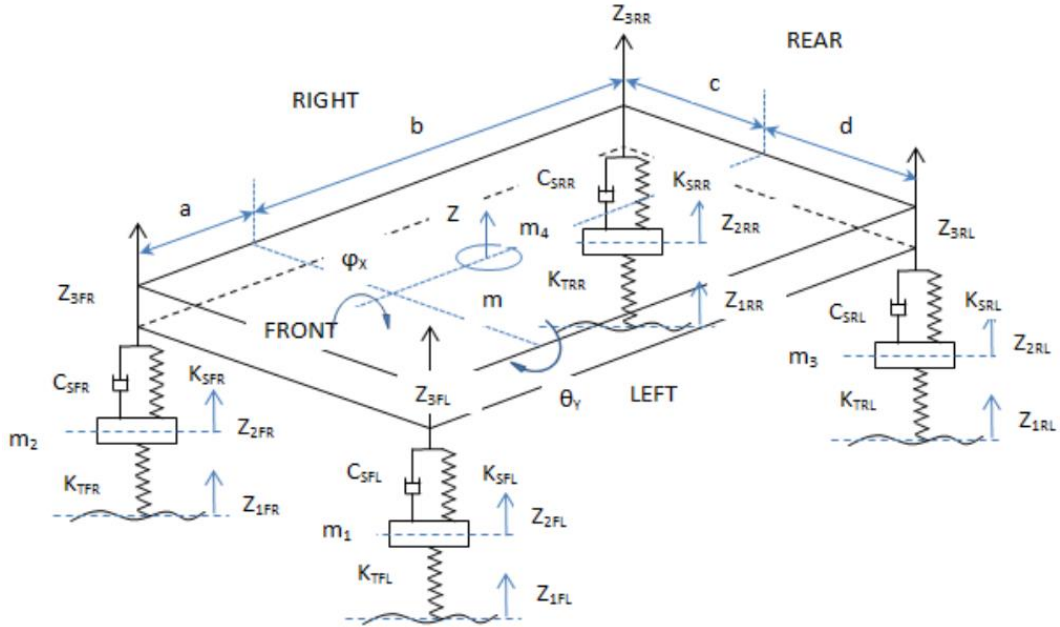


Figure 2.2: 7 DOF of ride model [2]

The displacement Z of sprung mass is defined by:

$$m \ddot{Z} = -F_{SFL} - F_{DFL} - F_{SFR} - F_{DFR} - F_{SRL} - F_{DRL} - F_{SRR} - F_{DRR} \quad (2.1)$$

With m the mass of the vehicle, \ddot{Z} is the body acceleration and F is the force acting on vehicle model (S for spring, D for damper, FL for front left, FR for front right, RL for rear left, RR for rear right).

The spring forces F_{Sij} (i for front or rear and j for left or right) that operate on the suspension are given by:

$$F_{Sij} = K_{Sij} (Z_{Bij} - Z_{Uij}) \quad (2.2)$$

Where Z_{Bij} is the sprung vertical displacement, Z_{Uij} is the unsprung mass vertical displacement and K_{Sij} is the suspension spring stiffness.

Then the damper forces F_{Dij} of suspension are provided by:

$$F_{Dij} = C_{Sij} (\dot{Z}_{Bij} - \dot{Z}_{Uij}) \quad (2.3)$$

\dot{Z}_{Bij} is the sprung vertical velocity, \dot{Z}_{Uij} is the unsprung mass vertical velocity and C_{Sij} is the suspension damper coefficient. Acceleration at unsprung mass is specified by:

$$m_{Uij} \ddot{Z}_{Uij} = F_{Sij} + F_{Dij} - F_{Tij} \quad (2.4)$$

Where m_{Uij} is the unsprung mass, \ddot{Z}_{Uij} is the vertical acceleration at unsprung mass and F_{Tij} is the dynamic tire forces, defined as:

$$F_{Tij} = K_{Tij} (Z_{Uij} - Z_{Rij}) \quad (2.5)$$

With K_{Tij} the tire stiffness and Z_{Rij} is the road profile where the disturbance on the road act.

The pitch effect of the vehicle is provided by:

$$J_y \ddot{\theta} = - (F_{SFL} + F_{DFL} + F_{SFR} + F_{DFR}) a + (F_{SRL} + F_{DRL} + F_{SRR} + F_{DRR}) b \quad (2.6)$$

J_y is the moment of inertia about y-axis and $\ddot{\theta}$ is the pitch acceleration, while a is the length of vehicle from the centre of gravity to the front end and b is the length of vehicle from the centre of gravity to the rear end of the vehicle.

The roll effect of the vehicle can be specified as follows:

$$J_x \ddot{\phi} = - (F_{SFL} + F_{DFL} + F_{SRL} + F_{DRL}) c + (F_{SFR} + F_{DFR} + F_{SRR} + F_{DRR}) d \quad (2.7)$$

Where J_x is the moment of inertia about x-axis and ϕ is the pitch acceleration, while c is the length of the vehicle from the centre of gravity to the right end and d is the length of vehicle from the centre of gravity to the left end of the vehicle.

2.3. Lateral dynamics

This paragraph describes the equations that govern the dynamic behaviour of a vehicle during cornering and more generally during changes of direction: aspects of lateral dynamics are the basis for handling and stability. The discussion begins with the *single track model* and then extends to a more complex one where there are 7 DOF and some of the simplifying assumptions of the previous theory are removed: the *double track model*.

2.3.1. Single track model

Also known as “bicycle model”, the *single track model* is the most common theory in the literature for lateral vehicle control. The driver and car constitute a “closed loop” system because the first continuously controls the vehicle to correct its direction or position. “Open loop” refers to car behaviour to characterize how this responds to a given steering input. Understeer gradient is a measure of performance in steady state conditions but can be used also in quasi-steady state conditions [3].

The functioning of a vehicle can be analysed at low/high speeds. At low speeds, the motion of the vehicle during cornering is determined by the pure rolling of the wheels, there are no tire slip angle α and lateral forces are null. At high speeds, the steering is dynamic and the previous aspects are not applicable: the trajectory of the vehicle is the result of a balance of forces acting on it.

In the study of this part the following simplifying hypotheses are adopted [4]:

- the vehicle moves on a horizontal plane at constant speed (there is a complete decoupling between longitudinal and lateral dynamics);
- the wheels of each axle are condensed into a single equivalent wheel;

- the radius of curvature of the trajectory is much greater than wheelbase;
- the vehicle sideslip angle β is assumed to be small;
- the tires slip angles α_f and α_r are considered small and, therefore, the lateral force is given by Equation 2.28;
- no aerodynamic and effects of load transfer, rolling and pitching are considered.

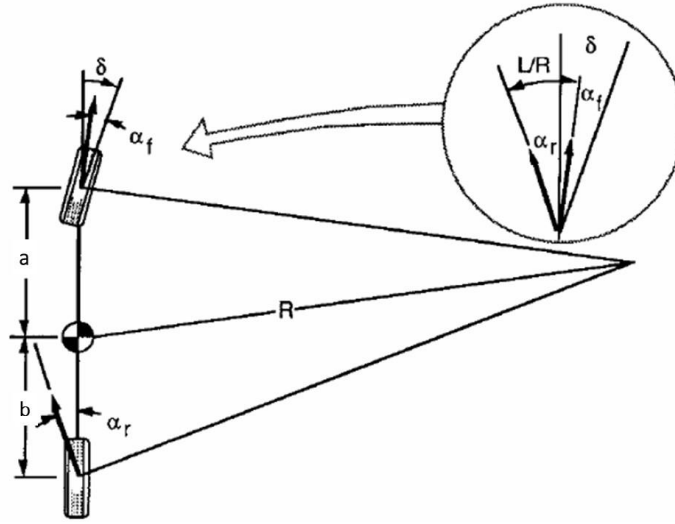


Figure 2.3: Cornering of a bicycle model [3]

From these premises the vehicle can be schematized as in the Figure 2.3. In [3], applying Newton's Second Law, Equation 2.8 is used to describe the behaviour of the vehicle in steady state. In lateral direction, for a car traveling forward with a speed v :

$$F_{y_f} + F_{y_r} = m \frac{v^2}{R} \quad (2.8)$$

Where F_y are lateral cornering forces at the front (f) and at the rear (r), m is mass of vehicle and R is radius of the turn.

Instead, from an equation of equilibrium to rotation around the centre of gravity:

$$F_{y_f} = F_{y_r} \frac{b}{a} \quad (2.9)$$

Substituting back in Equation 2.8, considering the lateral force $F_y = C_\alpha \alpha$ and acceleration $a_y = v^2/R$, the slip angles at the front and rear wheel are defined as:

$$\begin{aligned}\alpha_f &= m \frac{b}{l} \frac{a_y}{C_{\alpha_f}} \\ \alpha_r &= m \frac{a}{l} \frac{a_y}{C_{\alpha_r}}\end{aligned}\quad (2.10)$$

Where C_{α_i} is the cornering stiffness. From geometric and purely kinematic considerations it is obtained the steering wheel angle (SWA) δ_{sw} :

$$\delta_{sw} = \delta_0 + (\alpha_r - \alpha_f) \quad (2.11)$$

$\delta_0 = l/R$ is the Ackermann angle. Equation 2.11 can be rewritten using 2.10:

$$\delta_{sw} = \frac{l}{R} + K_U a_y \quad (2.12)$$

Equation 2.12 is crucial to the cornering response properties of a vehicle: it shows how SWA can be changed with R (or a_y), but depends also on the understeer gradient K_U :

$$K_U = \frac{m}{l} \left(\frac{b}{C_{\alpha_f}} - \frac{a}{C_{\alpha_r}} \right) \quad (2.13)$$

From the value of K_U there are three possibilities during on a constant radius turn [3]:

1. Neutral steer, $K_U = 0 \rightarrow \alpha_f = \alpha_r$. No change of SWA is necessary when speed is varied, but only the Ackerman angle.
2. Understeer, $K_U > 0 \rightarrow \alpha_f > \alpha_r$. In this case the increase of a_y , which depends on v^2 , causes a bigger slip angle on the front wheels α_f : therefore, to maintain vehicle's stability in cornering is required a greater δ_{sw} .
3. Oversteer, $K_U < 0 \rightarrow \alpha_f < \alpha_r$. The rear wheels develop a higher slip angle α_r than the front ones. To obtain a stable behaviour, δ_{sw} must decrease when the v is risen.

In Figure 2.4 is illustrated the way in which SWA changes with speed to maintain a constant curve radius. With a neutral steer vehicle, δ_{sw} corresponds to δ_0 at any speed, while in the understeer case SWA increases with the square of the speed, achieving twice the initial angle at the "characteristics speed". With oversteer, δ_{sw} decreases with the v^2 and becomes zero at the "critical speed".

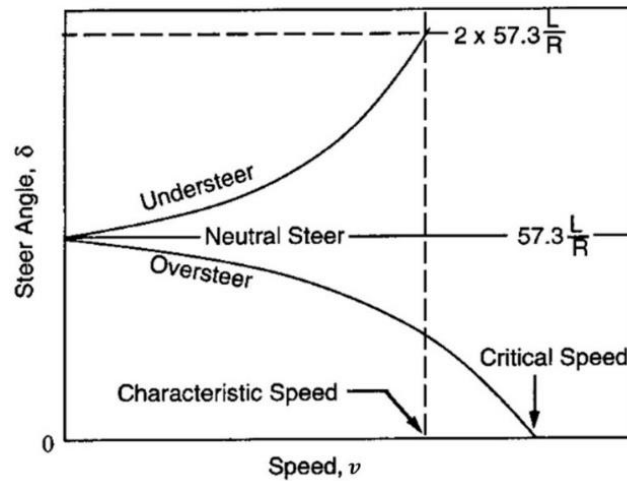


Figure 2.4: Change of SWA with speed [3]

However, the directional behaviour of the vehicle not only depends on the response to the steering, but also on external forces, moments, load transfers and convergence.

2.3.2. Double track model

To observe the influence of TV on the dynamic behaviour of the vehicle, wheels capable of rotating around their own axis and generating forces independently of each other must be implemented in the model. In addition, this it forces to insert a further equation relating to the displacement along the longitudinal axis: therefore, from the *bicycle model* with 2 DOF it switches to *double track model* with 7 DOF.

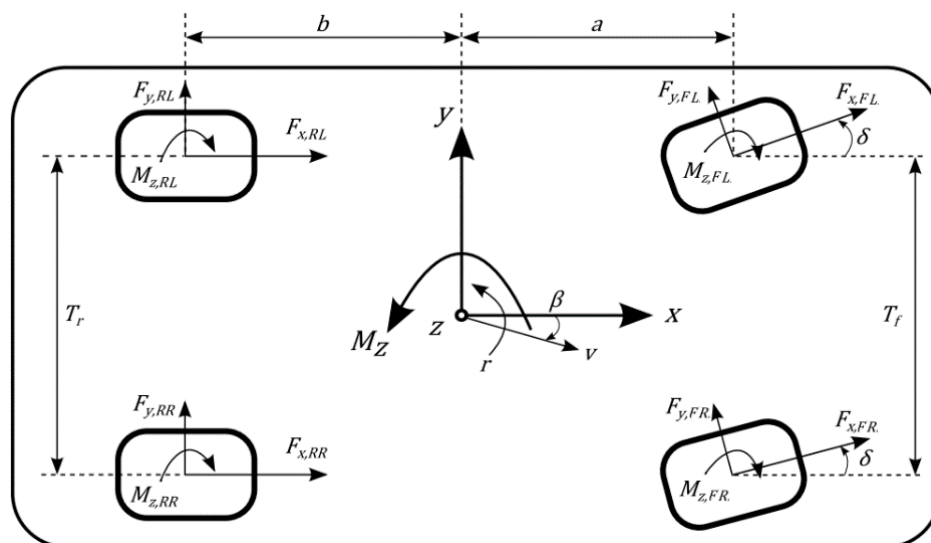


Figure 2.5: 7 DOF of double track model (adapted from [5])

From Figure 2.5 it is possible to write the following equilibrium equations for lateral translation y and longitudinal translation x [1]:

$$m a_x = (F_{x,FL} + F_{x,FR}) \cos \delta_{sw} - (F_{y,FL} + F_{y,FR}) \sin \delta_{sw} + F_{x,RL} + F_{x,RR} - 0.5 \rho C_x S v_x^2 \quad (2.14)$$

$$m a_y = (F_{y,FL} + F_{y,FR}) \cos \delta_{sw} + (F_{x,FL} + F_{x,FR}) \sin \delta_{sw} + F_{y,RL} + F_{y,RR} \quad (2.15)$$

Where ρ is the density of the air, C_x is the drag coefficient and S is the cross-sectional area. In a similar way the yaw acceleration \dot{r} is calculated considering all the contributions to the moment around z -axis passing through the vehicle centre of mass:

$$\begin{aligned} \dot{r} J_Z = & [(-F_{y,FR} + F_{y,FL}) \sin \delta_{sw} + (F_{x,FR} - F_{x,FL}) \cos \delta_{sw}] \frac{T_f}{2} + (F_{x,RR} - F_{x,RL}) \frac{T_r}{2} + \\ & + [(F_{y,FL} + F_{y,FR}) \cos \delta_{sw} + (F_{x,FL} + F_{x,FR}) \sin \delta_{sw}] a - (F_{y,RL} + F_{y,RR}) b + \\ & - M_{z,FR} - M_{z,FL} - M_{z,RR} - M_{z,RL} \end{aligned} \quad (2.16)$$

By integrating Equation 2.16 it is possible to get the yaw rate r . $M_{z,ij}$ is the self-aligning moment, a contribution due to the lateral force acting at a certain distance from the centre of contact patch of the tire. This moment tends to neutralize the tire slip angle and the centrifugal force, bringing the longitudinal wheel direction toward that of the velocity.

The components of the acceleration of the vehicle in the local coordinate system are expressed by:

$$\begin{cases} v_x = \int (a_x + r v_y) dt \\ v_y = \int (a_y - r v_x) dt \end{cases} \quad (2.17)$$

From Equations 2.17 the absolute value of velocity of the vehicle can be derived:

$$v = \sqrt{v_x^2 + v_y^2} \quad (2.18)$$

With the *double track model*, load transfers caused by accelerations can also be considered. The longitudinal acceleration a_x produces a pitch acceleration $\ddot{\theta}$ that can be determined from Figure 2.6 [1]:

$$m a_x h_{CG} + m g e - K_\theta \theta - C_\theta \dot{\theta} = J_y \ddot{\theta} \quad (2.19)$$

With K_θ and C_θ that are respectively the suspension pitch stiffness and the damping pitch coefficient and h_{CG} is the height of the centre of gravity (CG). The load transfer due to a_x is the following:

$$\Delta F_{z a_x} = \frac{m a_x h_{CG}}{l} \quad (2.20)$$

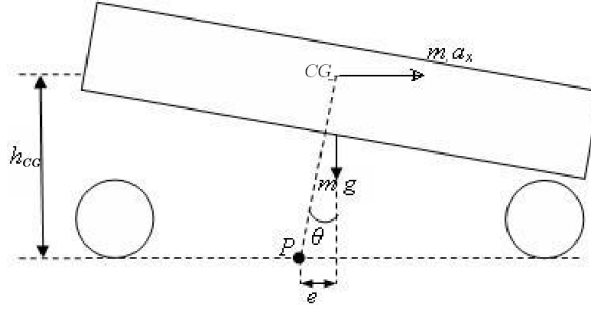


Figure 2.6: Pitch motion due to longitudinal acceleration [1]

Lateral acceleration is present when there is a change of direction and thus a centrifugal force causes a rotation of the sprung mass of a certain angle ϕ around the roll centre, the point where each force applied does not cause any rotation.

With Figure 2.7 it is possible to obtain the differential equation which defines the roll dynamics of the sprung mass subject to a_y [4]:

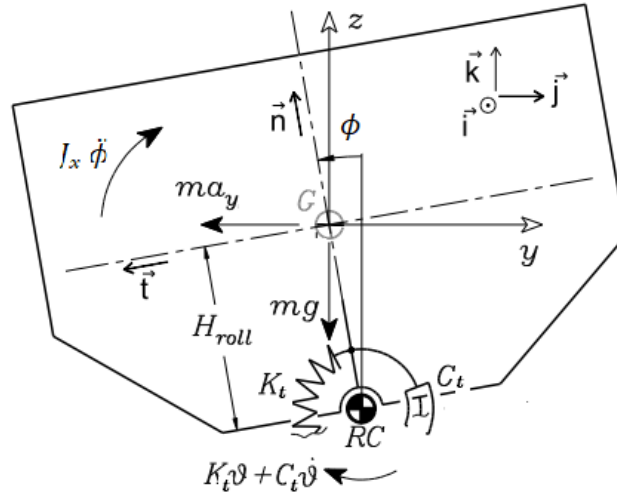


Figure 2.7: Free body diagram of the sprung mass [4]

$$(J_x + mH_{roll}^2 \cos \phi) \ddot{\phi} = m a_y H_{roll} \cos \phi + m g H_{roll} \sin \phi - K_t \phi - C_t \dot{\phi} \quad (2.21)$$

Where H_{roll} is the height of the roll centre respect to the CG, K_t and C_t are respectively the sum of the front and rear suspension roll stiffness and the damping roll coefficient.

Given the non-coincidence between the roll centre and the CG, the presence of lateral acceleration and a consequent roll motion determine a lateral load transfer. Therefore $\Delta F_{z,lat,ij}$ between the inner left wheels and the outer right wheels is defined as:

$$\Delta F_{z,lat,ij} = m a_y \frac{H_{RC}}{T_i} + \frac{K_i \phi + C_i \dot{\phi}}{T_i} \quad (2.22)$$

Where $H_{RC} = H_{CG} - H_{roll}$, K_i and C_i the suspension roll stiffness and the damping roll coefficient on the axle i (Figure 2.8).

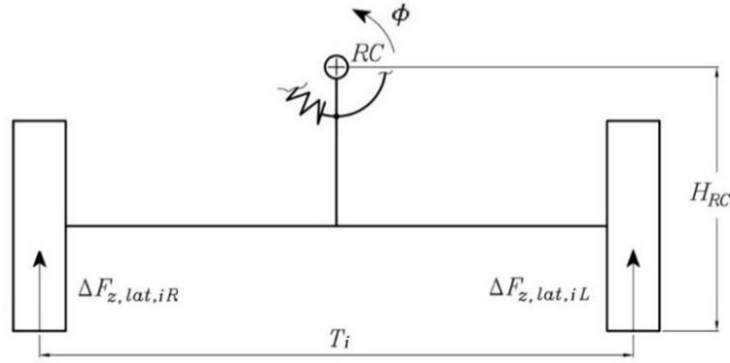


Figure 2.8: Lateral load transfer (adapted from [4])

The single DOF of each wheel is calculated from an equilibrium rotation with force and moments acting on it (Figure 2.9) [4]:

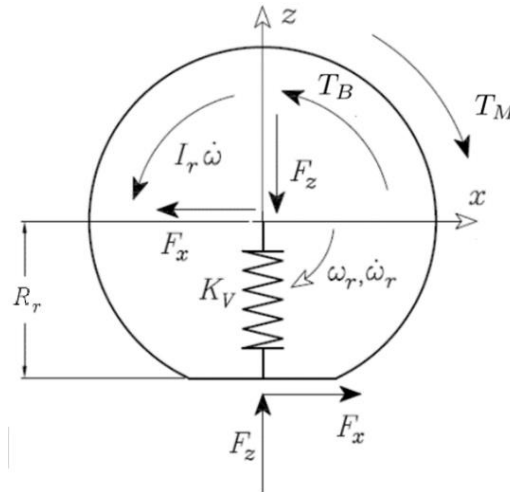


Figure 2.9: Wheel free body diagram [4]

$$\omega_r = \frac{T_M - T_B - F_z (f_0 + K_V R_e^2 \omega_r^2) - F_x R_r}{I_r} \quad (2.23)$$

Where T_M is the driving torque, T_B is the braking torque, F_z and F_x represent respectively the vertical and longitudinal force acting on the tire, f_0 is the constant coefficient of rolling resistance, K_V is the tire vertical stiffness and R_r is the loaded tire radius which is obtained as follows:

$$R_r = R - \frac{F_z}{K_V} \quad (2.24)$$

With R is the undeformed tire radius. The accelerations a_x and a_y cause load transfers between front and rear axles, left and right wheels: to reach a better dynamic, these transfers must be minimized.

2.4. Tire characteristics

It is essential to consider the tire characteristics for their important role in the dynamic behaviour of the vehicle. The main parameters are the longitudinal slip k and slip angle α [6]. The absence of driving torque may be defined as the starting situation with all components of slip equal to zero, where the wheel rolls freely. When a torque is applied about the wheel spin axis a longitudinal slip k arises that is defined as:

$$k = -\frac{v_x - R_e \omega}{v_x} = -\frac{\omega_0 - \omega}{\omega_0} \quad (2.25)$$

With v_x being the longitudinal component of velocity vector v of the wheel centre, $R_e = v_x/\omega_0$ the effective rolling radius and ω_0 the angular speed of revolution. The sign of k is positive when there is a driving longitudinal force F_x : in that case the actual wheel angular velocity ω becomes bigger with respect to ω_0 . During braking, the fore and aft slip becomes negative.

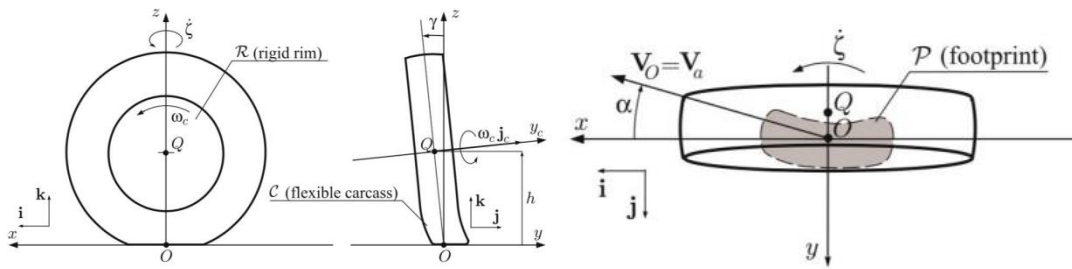


Figure 2.10: Nomenclature and reference system of the tire [4]

Lateral wheel slip is defined as the ratio of the lateral and the forward velocity of the wheel. This corresponds to minus the tangent of the slip angle α (Figure 2.10):

$$\tan \alpha = -\frac{v_y}{v_x} \quad (2.26)$$

Again, the sign has been chosen such that the lateral force becomes positive at $\alpha > 0$.

Hence, the forces F_x and F_y are results of the input k and α . Moreover, also the vertical load F_z and friction coefficient μ affect these quantities [4].

$$F_x = F_x(k, \alpha, F_z, \mu), \quad F_y = F_y(k, \alpha, F_z, \mu) \quad (2.27)$$

The dependency of longitudinal and lateral forces from these parameters is conventionally expressed by the slip curve.

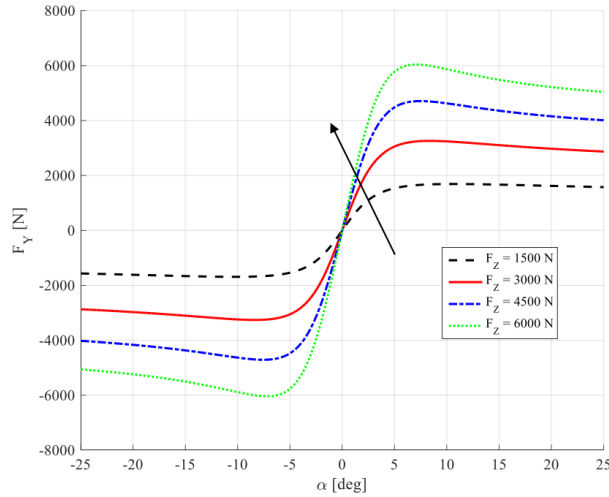


Figure 2.11: Effect of α and F_z on lateral force F_y [4]

Entering contact with the ground the wheel is deformed. The increase of F_z causes an extension in both the contact area with the road and the maximum specific pressure acting on the tire. These factors modify the trend of the tangential tensions τ_y and τ_x which are calculated the lateral and longitudinal forces through the *brush model*. In Figure 2.11 is shown as F_y grows with F_z ; the same is also true for F_x as a function of k .

For each curve around the origin, a direct proportional relationship between lateral force and slip angle can be highlighted: it is the cornering stiffness C_α (for longitudinal force is C_k) and represents the angular coefficient of the line tangent in the origin to the characteristic F_y as a function of the α . For small value of α is valid:

$$F_y = C_\alpha \alpha \quad (2.28)$$

The Figure 2.11 indicates that the slope rises with the vertical load, but the maximum value of F_y remains at the same slip angle α .

The trend of cornering stiffness C_α with F_z is not linear, as displayed in Figure 2.12: while C_k increases more than in proportion, C_α rises less than in proportion to the increasing vertical load: this outcome is of crucial importance to understand the load transfers and the function of the anti-roll bars in the lateral dynamics of a vehicle.

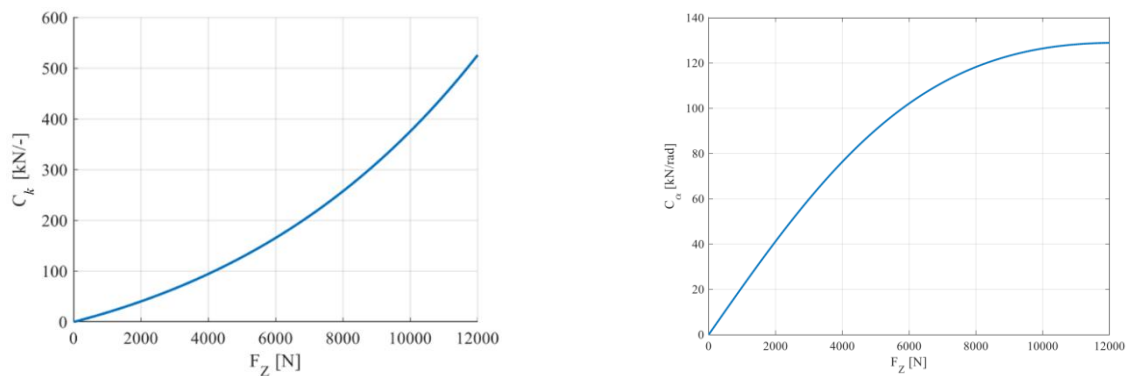


Figure 2.12: Cornering stiffness C_k (left) and C_α (right) in function of vertical load F_z [4]

Returning to the slip curves, in Figure 2.11 after the maximum value there is a reduction of the force: this is because the tire enters sliding [4].

Another variable that changes these curves is the friction coefficient μ , depending on the conditions of the road surface. Figure 2.13 shows how the longitudinal force changes when μ is different: the same characteristic applies to F_y .

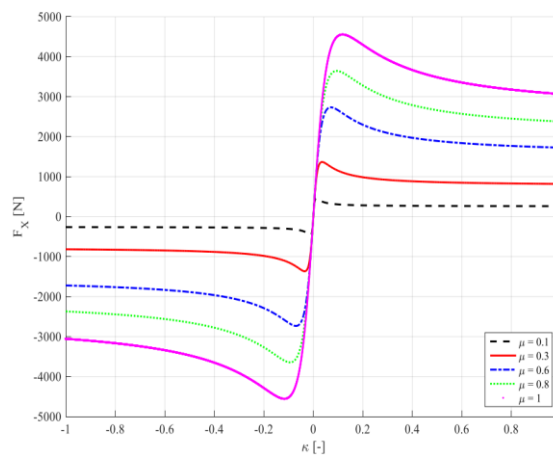


Figure 2.13: Influence of k and μ on longitudinal force F_x [4]

In general, the larger the μ coefficient, the more force is available. All curves start with the same slope in the origin for small longitudinal slip, while the maximum occurs for k higher as the coefficient of friction increases. Instead, a change of μ determines a minimum variation of cornering and longitudinal stiffness (the gradient of the curves near to the nominally null values) [4].

The combined slip theory is valid when there is a simultaneous presence of lateral and longitudinal forces that lead to deformation of the tire in both directions. To evaluate the mutual interaction between these forces, diagrams are used that plot the trend of the forces F_y for constant values of α together with the trends of the forces F_x for constant values of k : the envelope of these curves identifies the friction ellipse (Figure 2.14). An increase in longitudinal forces therefore decreases the lateral ones that can be developed on the ground (and vice versa) [4].

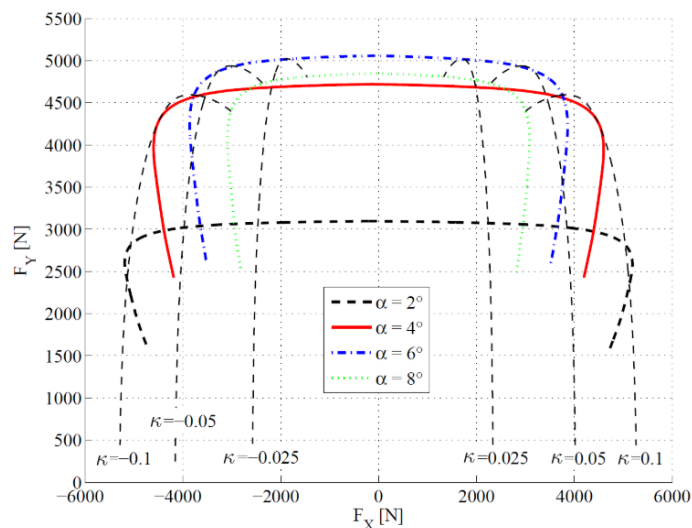


Figure 2.14: Influence of k and α on longitudinal F_x and lateral F_y forces [4]

2.4.1. Pacejka's Magic Formula

The previous theories of the tire force are based on physical models. In literature there are many mathematical descriptions of the relationship between the tire and the road surface: this part is important to evaluate the amount of F_x and F_y generated. Pacejka composed a semi-empirical model that needs a deep experimental characterization which has found great success in the field of simulations due to its accuracy [6].

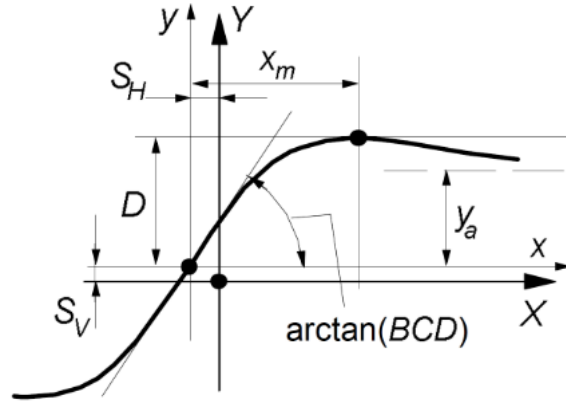


Figure 2.15: Curve produced by the original sine version of the Magic Formula [6]

With Figure 2.15 it is possible to interpret the general form of the formula that holds for given values of vertical load and camber angle reads:

$$\begin{cases} Y = D \sin[C \arctan\{Bx - E(Bx - \arctan Bx)\}] \\ Y(X) = y(x) + S_V \\ x = X + S_H \end{cases} \quad (2.29)$$

Where Y is the output variable F_x , F_y or M_z , X is the input variable $\tan \alpha$ or k , B is the stiffness factor, C is the shape factor, D is the peak value, E is the curvature factor, S_H is the horizontal shift and S_V is the vertical shift.

Pacejka's modelling is a good reference to estimate the system of actions received from a tire but is basically an average of experimental results obtained in bench testing under various conditions. Therefore, is not enough satisfactory to introduce a cause-effect relationship sufficient to make extrapolations to conditions other than those of the test: if more precision is sought, more sophisticated models must be used [4].

2.5. Handling diagrams

The capability of a car in handling is assessed through a variety of steady state directional control test: the most used are constant radius – variable speed test and the constant speed – variable radius test.

When these tests are carried out with a full complement of instruments the data is often reduced to response ratios. The most common are the understeer (from δ_{sw}),

sideslip β and roll θ gradient in function of lateral acceleration expressed in “g” units. These gradients are measured as slopes of the response curves g in the linear range of tire performance [7].

These ratios are reported in diagrams: an example is understeer characteristic in the Figure 2.16. The considerations are those discussed during the description of the *single track model* (in paragraph 2.3.1), with the understeer gradient K_U .

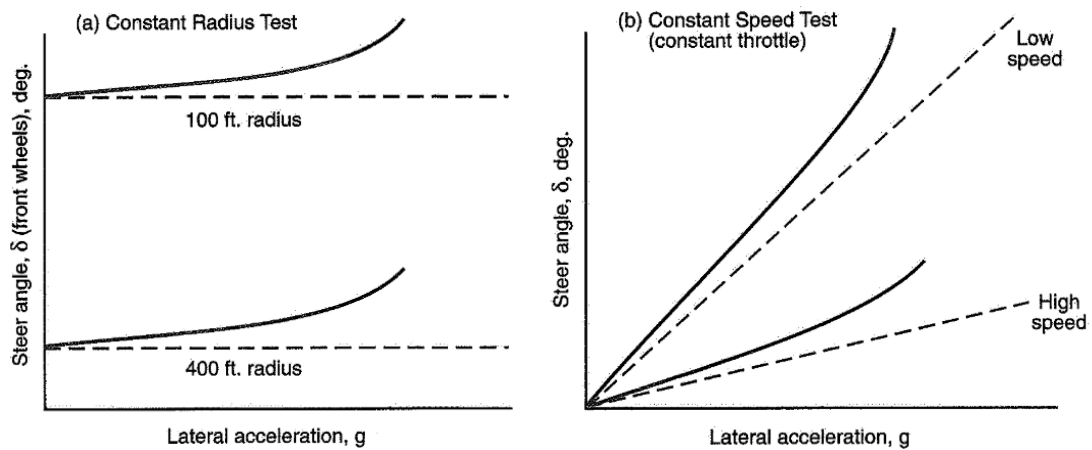


Figure 2.16: Example of understeer characteristic in steady state [7]

Another variable to evaluate the stability in cornering is the sideslip angle β : when the lateral acceleration increases, the rear of the vehicle must drift outboard to develop the necessary α_r . Equation 2.30 contains this phenomenon:

$$\beta - \beta_0 = -\alpha_r = -\frac{m a}{l C_{\alpha_r}} a_y = K_{\beta} a_y \tag{2.30}$$

Where $\beta_0 = b/R$ is the kinematic sideslip and K_{β} is the sideslip gradient, which depends only on the parameters of the rear axle (unlike K_U) and always has a descending characteristic with the lateral acceleration that increases [4].

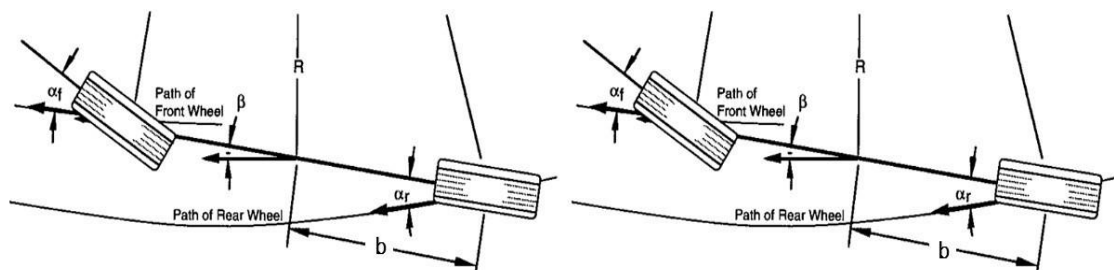


Figure 2.17: Sideslip angle in a low-speed turn (left) and a high-speed turn (right) [3]

In general, β can be different at every point on a car during cornering. In Figure 2.17 is considered from the centre of gravity: at low-speed turn sideslip angle is defined as positive when the direction of travel is oriented clockwise from the longitudinal axis, vice versa at high speeds it is directed in the other direction and is negative [3]. The sideslip gradient K_β can be measured, for example, through Figure 2.18, where β is estimated in function of lateral acceleration in “g” units.

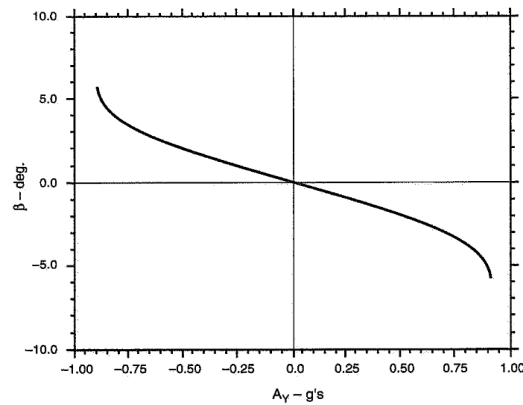


Figure 2.18: Example of sideslip angle characteristic in steady state [7]

The roll angle represents 1 DOF of the chassis and has been used in the equations of the *double track model*, observing its role in lateral load transfers. More roll moment M_ϕ on the front axle contributes to understeer, whereas more M_ϕ on the rear axle contributes to oversteer. With the antiroll bar it is possible to alter handling performance through this mechanism applied to the front axle for understeer and to the rear for oversteer [3]. In Figure 2.19, the roll is evaluated in function of the lateral acceleration.

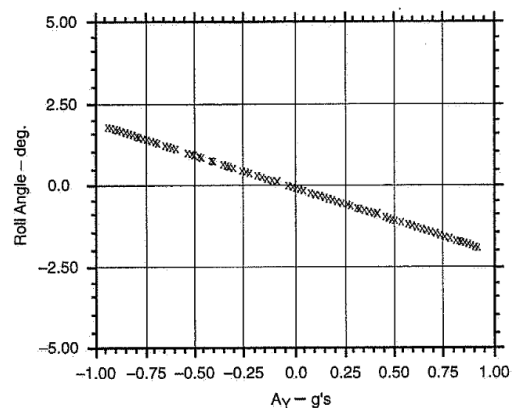


Figure 2.19: Example of roll angle characteristic in steady state [7]

3. VI-CarRealTime

The virtual vehicle model and the tests were created with VI-CarRealTime 19.0 (VI-CRT). This software is an innovative product for engineers who want to quickly evaluate the handling performance of a certain vehicle configuration, develop a vehicle controller and test a prototype.

In this section will be delineated the software's architecture and detailed the framework of the vehicle created in VI-CRT for this thesis. On this model the TV controller was actuated, using the co-simulation with Simulink: a paragraph will be dedicated to the description of this mode. All information in this chapter that does not concern the vehicle model created for TV control has been taken from [8].

3.1. Environment

VI-CRT is a virtual modelling and simulation environment targeted to a simplified four wheels vehicle. Its functionalities include the ability to assemble the vehicle system by collecting its fundamental subsystems, specifying dynamic manoeuvre schedules, launching standalone or MATLAB/Simulink embedded simulations, postprocessing the obtained results. The environment based on underlying solver consists of:

- Symbolically derived parameterized equations of motion;
- Pacejka tire model;
- Sophisticated, virtual driver model.

The framework is divided into following modes:

- Build 

The *Build mode* allows to edit model data and change system configuration, also working on multiple models at once. The vehicle model was created in this section, as explained in paragraph 3.2.

- Test 

The *Test mode* permits to run the model, organizing an event from bookshelf or building it. More information about this environment will be given in paragraph 3.3: here the manoeuvres to evaluate the behaviour of the vehicle have been edited.

- Review 

The *Review mode* lets to visualize analysis results using VI-Animator. Postprocessing has two formats: animation and plots. The latter can derive from about 900 output variables that the user can track over.

- Investigation 

The *Investigation mode* allows to run multiple simulations based on one or more events, while modifying a set of model parameters.

The VI-CRT window has a consistent design in each mode. These elements include: “Menubar”, “Toolbar”, “Treeview” and “Property Editor”. The logical of “Treeview” is useful when creating/modifying a model or an event: there is a hierarchical listing of objects in the current session.

3.2. Virtual model vehicle

The hybrid vehicle configuration was carried out in the *Build Mode*, modifying the various subsystems to comply with the required characteristics. To better understand some settings, it is first necessary to discuss the DOF and reference systems implemented in VI-CRT.

3.2.1. Reference system and model configuration

VI-CRT model includes 14 DOF, distributed as discussed in paragraph 2.1: the vehicle chassis has 6 DOF while each wheel has 2. Other DOF could have been considered for

each suspension or body chassis torsional compliances, but these alternatives are not considered in this thesis.

The reference frames and coordinate systems used in VI-CRT have been established considering the DOF just mentioned: these are shown in the Figure 3.1.

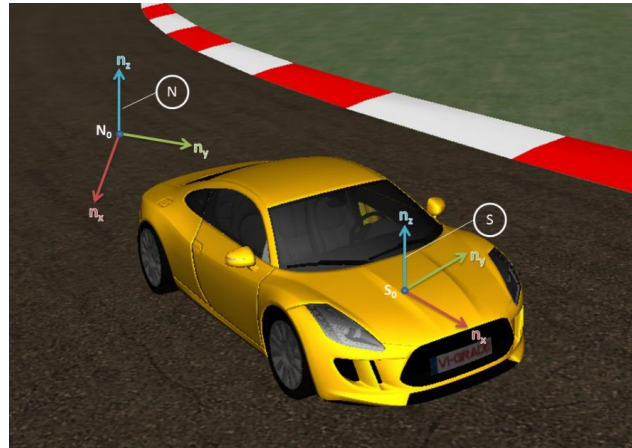


Figure 3.1: VI-CRT reference frames [8]

The reference systems used, consistent with the standards ISO 8855 Road vehicles and SAE Recommended Practice J670f, are the following:

- *Global Reference Frame*, the system n_x , n_y and n_z , with origin point N_0 in the vehicle chassis. N denotes Newtonian (or inertial frame): this means that it does not accelerate in translation and does not rotate;
- *Vehicle Reference System*, with origin point S_0 at half front vehicle track. It is defined by a triad having the $Z +$ axis oriented as the road normal vector, the $X +$ axis as the vehicle forward direction and the $Y +$ axis accordingly;
- *Wheel Location Reference System*, it is fixed by a triad positioned at the wheel centre (left and right, at design time). The orientation is the same as *Global Reference Frame* with $X+$ forward, $Y+$ left and $Z+$ vertical up.

VI-CRT *Build mode* allows to edit model data and change system configuration. In his tree view on the left and in subsystem definition on the right the components of vehicle are shown (Figure 3.2).

The list of vehicle subsystem files is formed from: *Front Suspension*, *Rear Suspension*, *Steering System*, *Body*, *Powertrain*, *Front Wheel/Tires*, *Rear Wheel/Tires* and *Brakes*.

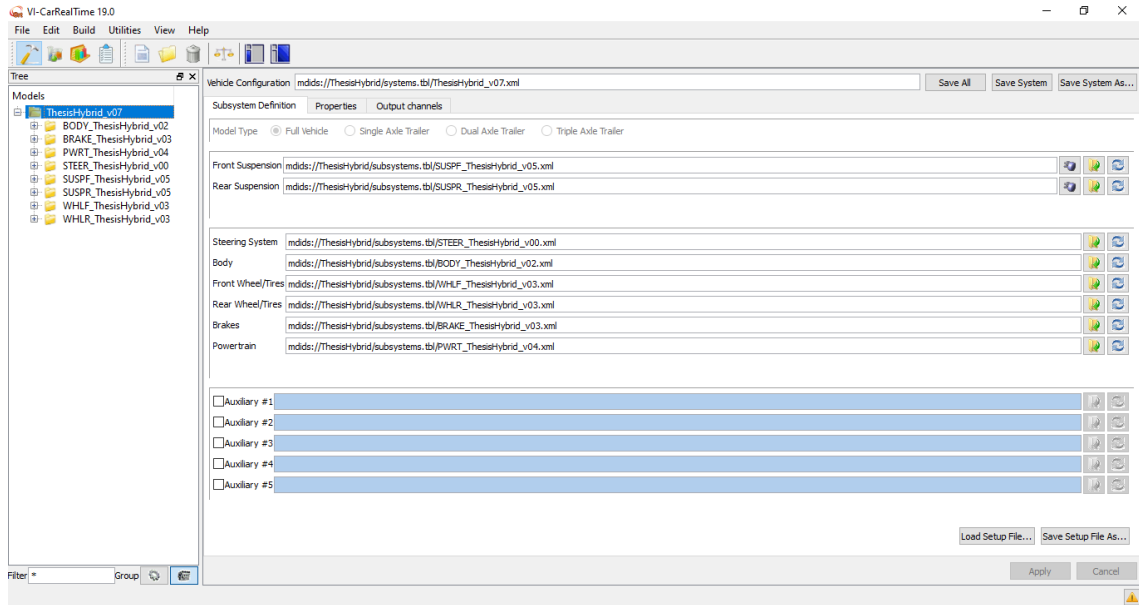


Figure 3.2: VI-CRT *Build Mode* and subsystem definition

Vehicle system files contain a set of information beyond the list of the subsystems. Without using imports from Adams Car, the vehicle model was created following a specific layout and objectives, modifying the data of the various subsystems.

3.2.2. *Body*

Table 3.1: Sprung mass properties

| Vehicle (kerb + 2 passengers + fuel) | |
|--|------|
| <i>Total mass [kg]</i> | 1850 |
| <i>Wheelbase [mm]</i> | 2600 |
| <i>CoG height [mm]</i> | 490 |
| <i>Weight distribution front [%]</i> | 48 |
| <i>Roll inertia I_{xx} [kgm²]</i> | 700 |
| <i>Pitch inertia I_{yy} [kgm²]</i> | 2600 |
| <i>Yaw inertia I_{yy} [kgm²]</i> | 2900 |

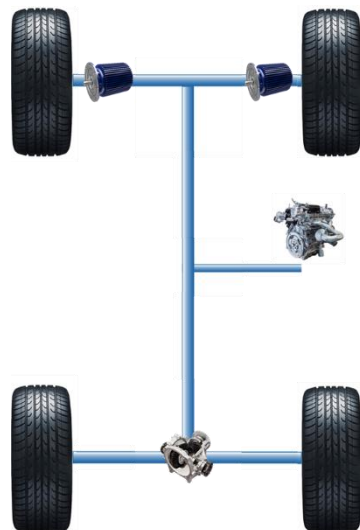
The body subsystem properties merge mass, inertia, setup and accessory information about the sprung mass part of VI-CRT. The “Sprung Mass” gives access to the sprung mass inertia, property of vehicle chassis and the wheelbase (Table 3.1).

In addition, the “Sensor Point” and the “Adams Car CG Point” must be located: the first is used to monitor position, velocity and acceleration during simulations; the second to set the position of chassis part CG. Position and orientation of these sensors are expressed in *Global Reference Frame*. Finally, because in common applications it is ordinary to test vehicle performance under load condition, in “Body Setup Data” masses and locations for driver, passenger and fuel were established, indicated in *Global Reference Frame*. All this information is contained in the Table 3.2.

Table 3.2: Position sensors, passengers and fuel

| | X location [mm] | Y location [mm] | Z location [mm] | Mass [kg] |
|---------------------------|--------------------|--------------------|--------------------|--------------|
| <i>Sensor Point</i> | -1364 | 0 | 538 | – |
| <i>Adams Car CG Point</i> | -1364 | 0 | 538 | – |
| <i>Driver</i> | -1100 | 350 | -1700 | 75 |
| <i>Passenger</i> | -1100 | -350 | 0 | 75 |
| <i>Fuel</i> | -1700 | 450 | 400 | 50 |

3.2.3. Powertrain



AWD powertrain:

- Front left electric motor (EM)
- Front right electric motor (EM)
- Rear axle ICE
- Rear differential (LSD)

Figure 3.3: Driveline layout

The powertrain subsystem includes data for the engine, electric motors, clutch, transmission and differential. It also includes information for gear shifting strategies.

The present hybrid vehicle driveline is an All-Wheel-Drive (AWD) and is shown in Figure 3.3. At the front each wheel is connected to an electric motor (on-board), while at the rear there is an internal combustion engine (ICE). Some simplifications have been made in their design: the fuel of the ICE and the energy of the battery of the electric motors were supposed to be infinite. The only differential implemented is at the rear, a Limited Slip Differential (LSD). In Table 3.3 are reported these data.

Table 3.3: Engine and motors data

| | Engine | LSD | Electric motors |
|------------------------------|--------|-----|-----------------|
| Transmission ratio [-] | 1 | 5.2 | 2.5 |
| Inertia [kgmm ²] | 70000 | 200 | 5000 |

Respectively, in the “Engine” and “Motors” panel, the torques have been set: the results are in Figure 3.4. The rear engine motor has two different trends of torque with speed rotation: the first curve “motor” is valid for the max throttle demand, the other for the minimum (“coasting”). The same concept applies to electric motors but braking torque (“motor brake”) is also added.

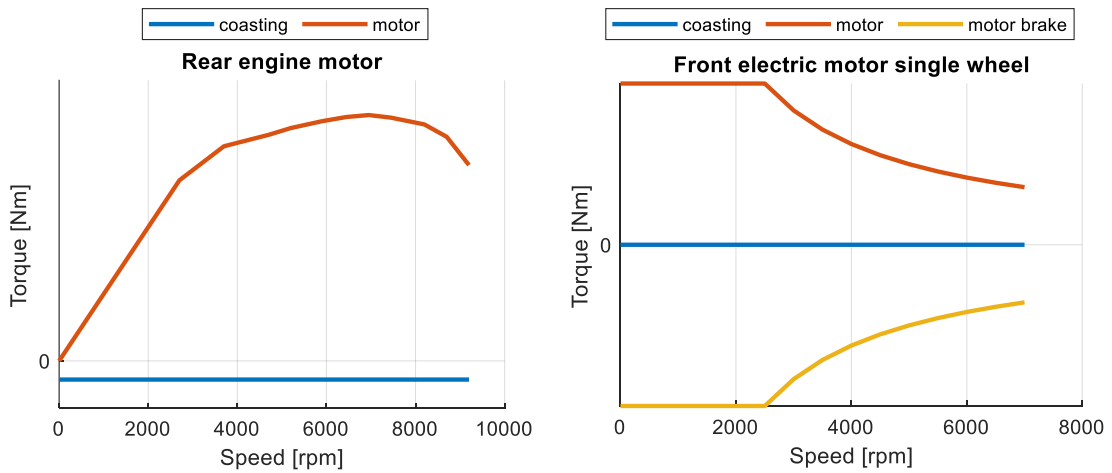


Figure 3.4: Rear engine and front electric motor torque map

These values have been chosen to allow this sports vehicle to reach a maximum speed of at least 300 km/h, a time not exceeding 4 s from 0 to 100 km/h and a longitudinal acceleration of at least 1 g.

3.2.4. Brakes

The brake model in this virtual vehicle represents a four-wheel disk brake configuration. The brake calipers and pistons were chosen by [9], with the dimensions expressed in the Figure 3.5.

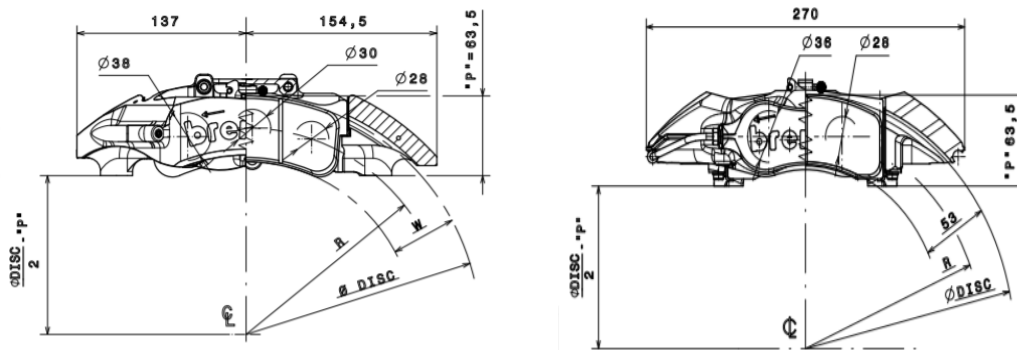


Figure 3.5: Calipers drawing to the front (at left) and to the rear (at right) [9]

The choice was made to have an area and an acting radius of the pistons such as to obtain a front brake distribution of 60%. The selection of the master cylinder is also in function of this target. The complete design of the brake system is in the Table 3.4.

Table 3.4: Brake specifics

| Brakes | Front | Rear |
|---------------------------------------|--------------|-------------|
| <i>Master cylinder diameter [mm]</i> | 39 | 39 |
| <i>Acting radius [mm]</i> | 152.5 | 140 |
| <i>Pistons number</i> | 6 | 4 |
| <i>Master Cylinder pressure [MPa]</i> | 12 | 1 |
| <i>Brake Line pressure [MPa]</i> | 6 | 6 |
| <i>Brake Torque [Nm]</i> | 3850 | 2570 |
| <i>Brake distribution [%]</i> | 60 | 40 |

3.2.5. Wheels

The wheels subsystem properties collect mass, inertia, tire property file information of unsprung mass pairs of VI-CRT vehicle model. The main information of the tires used are summarized in the Table 3.5.

Table 3.5: Unsprung mass data

| <i>Unsprung mass</i> | Front | Rear |
|---|--------------|-------------|
| <i>Spin inertia (one wheel) [kgm²]</i> | 1.00 | 1.00 |
| <i>I_{xx} (hub carrier + wheel) [kgm²]</i> | 0.92 | 1.61 |
| <i>I_{yy} (hub carrier + wheel) [kgm²]</i> | 1.03 | 1.10 |
| <i>I_{zz} (hub carrier + wheel) [kgm²]</i> | 0.91 | 1.58 |
| <i>Unsprung mass [kg]</i> | 56 | 60 |
| <i>Wheel center height [mm]</i> | 329 | 353 |
| <i>Vertical stiffness [kN/m]</i> | 294 | 348 |

In addition to the geometric and mass ones, it is available a data ASCII file where the tire is completely defined. For this vehicle, the scaling coefficients governed by Pacejka (Equation 2.29) were used to achieve the set objectives of handling and maximum accelerations.

The D factors regulates the peak of the longitudinal and lateral forces and consequently the maximum accelerations. Instead, B is the scaling factor of the F_y cornering stiffness: this controls the understeer and sideslip gradient, as seen in Equation 2.13 and 2.30 respectively.

Table 3.6: Pacejka tire model scaling coefficients

| <i>Tire scaling coefficients</i> | Front | Rear |
|---|--------------|-------------|
| $F_x \rightarrow D$ | - 3 % | 0 % |
| $F_y \rightarrow D$ | - 3 % | 0 % |
| $C_\alpha \rightarrow B$ | + 50 % | + 30 % |

3.2.6. Suspensions

In VI-CRT the suspensions subsystems are described using a conceptual approach: no physical part or linkage are present, the movement of the wheel is related to vertical jounce (independent variable in equations of motion) using a special constraint in order to define the position and orientation (5 DOF) by look-up tables.

The dampers and springs are the main elastic components in the suspension. The Figure 3.6 reveals the 2D damping curve: it is obtained with a non-linear method and defines the damper element force as a function of damper velocity.

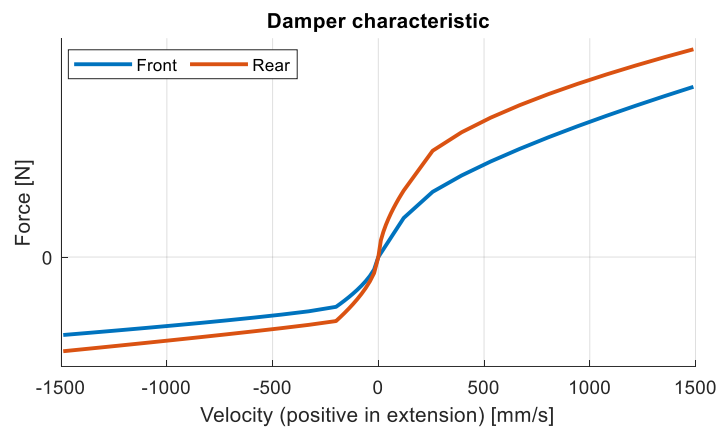


Figure 3.6: Damper characteristic

For the springs it is necessary to define a preload, the force acting at spring ends at design time, in order to have a static suspension jounce smaller than 3 mm . Furthermore, using a linear method the free length and stiffness were specified.

Another parameter to decide is the bumper, used to limit suspension jounce. In each VI-CRT suspension model there are two pairs of instances of bumpers, one for boundstop and the other for reboundstop.

To ensure a max bump travel at 5 g of 80 mm and a reboundstop travel of 90 mm , the bumpstop and reboundstop clearances have been changed. These describe the deformation that the component must undergo before engaging and applying a force.

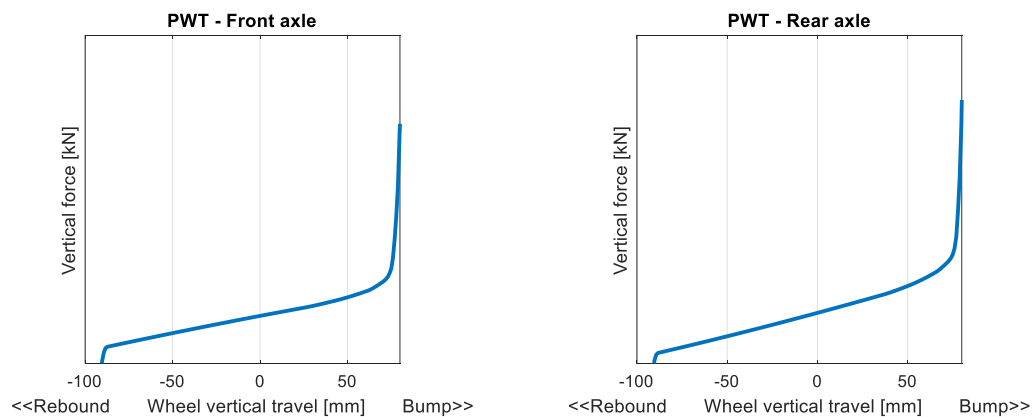


Figure 3.7: PWT suspension test

Figure 3.7 shows the result of the parallel wheel travel (PWT). This test indicates the trend of the vertical force acting on the wheel and its movements in the same direction: the linear part of the curve is regulated by the stiffness of the spring, previously defined, while the non-linear part depends on the intervention of the bumpstop and reboundstop.

The ride frequency f_r has been calculated considering a corner mass damper spring system with 1 DOF. Stiffness is the series of the tire (K_{tire}) with that of the wheel centre (K_{susp}).

$$f_r = \frac{1}{2\pi} \sqrt{\frac{K_{susp} \cdot K_{tire}}{K_{susp} + K_{tire}}} \frac{1}{m_{corner}} \quad (3.1)$$

To achieve the target roll gradient, the anti-roll bars must be considered: they are responsible of the effect of the elastic elements that connect the left and right coupled wheels. Depending on the conceptual suspension model, a pair of opposite vertical forces acts between the wheel (unsprung mass) and the body chassis: its intensity is due to the anti-roll bar stiffness.

Table 3.7: Suspension properties

| Suspensions | Front | Rear |
|---|--------------|-------------|
| <i>Springs preload [N]</i> | 6170 | 5550 |
| <i>Springs stiffness [N/mm]</i> | 85 | 80 |
| <i>Ride frequency [Hz]</i> | 1.25 | 1.44 |
| <i>Anti roll bar stiffness (SWT) [N/mm]</i> | 20.7 | 10.5 |
| <i>Bumpstop clearance [mm]</i> | 15.5 | 26.9 |
| <i>Reboundstop clearance [mm]</i> | 55 | 63 |
| <i>Max bump travel (@ 5g) [mm]</i> | 80 | 80 |
| <i>Rebound travel [mm]</i> | 90 | 90 |
| <i>Track width [mm]</i> | 1680 | 1650 |
| <i>Static toe angle [deg]</i> | -0.10 | 0.15 |
| <i>Static camber angle [deg]</i> | -1.0 | -1.5 |

All these variables are contained in the Table 3.7: there are also the track width, the distance among left/right wheel centres at design time (Y direction of *Global Reference System*), the static toe and camber angle (measured as shown in the Figure 3.8).

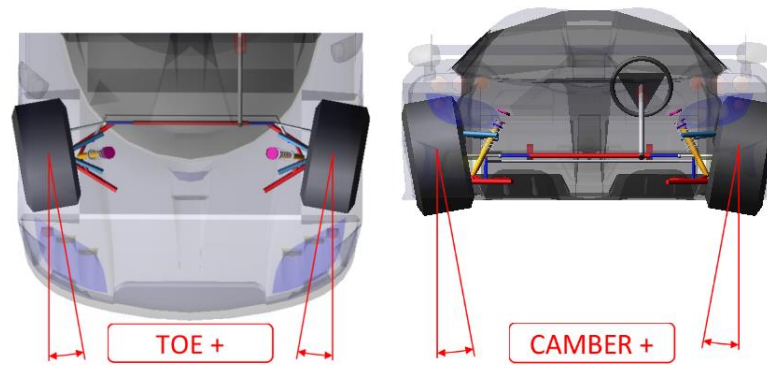


Figure 3.8: Toe and camber angle [8]

3.3. Test mode

In the VI-CRT *Test mode* simulations events can be created and run. The main window (Figure 3.9) is organized in *Events bookshelf*, that shows the list of the available event classes, in *Fingerprint treeview*, the tree of fingerprints present in session, and in *Property Editor*, where the parameter for the single event are set.

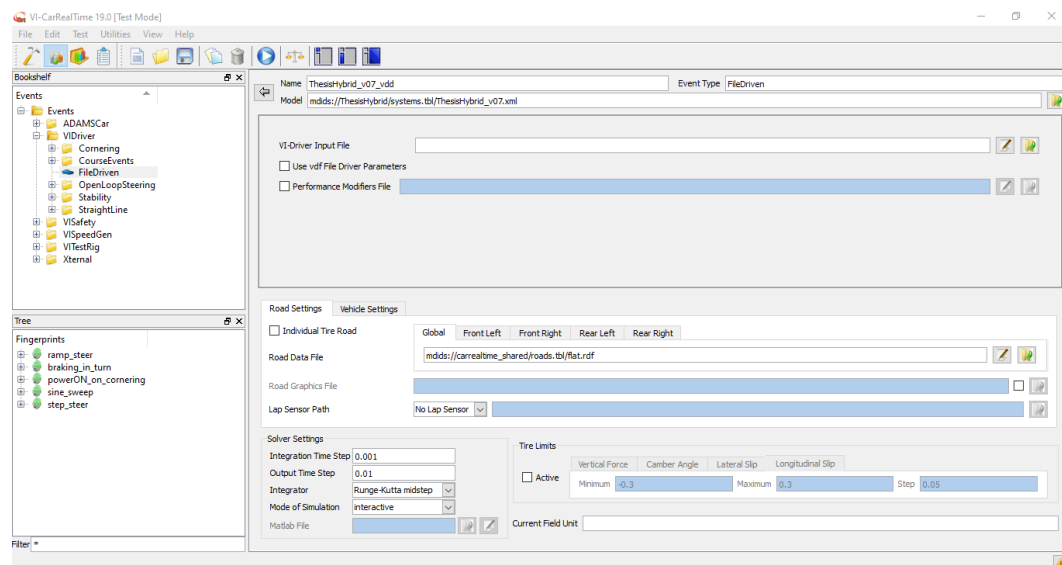


Figure 3.9: VI-CRT *Test Mode*

Although there were pre-set tests available, in this thesis the *File Driven* event was used to have complete customization. The geometric and physical characteristics (friction coefficient) of the road have been specified in *Road data file*, the event simulation parameters in *Solver setting* and the manoeuvre, that the virtual driver must execute, has loaded in *VI-Driver Input File*.

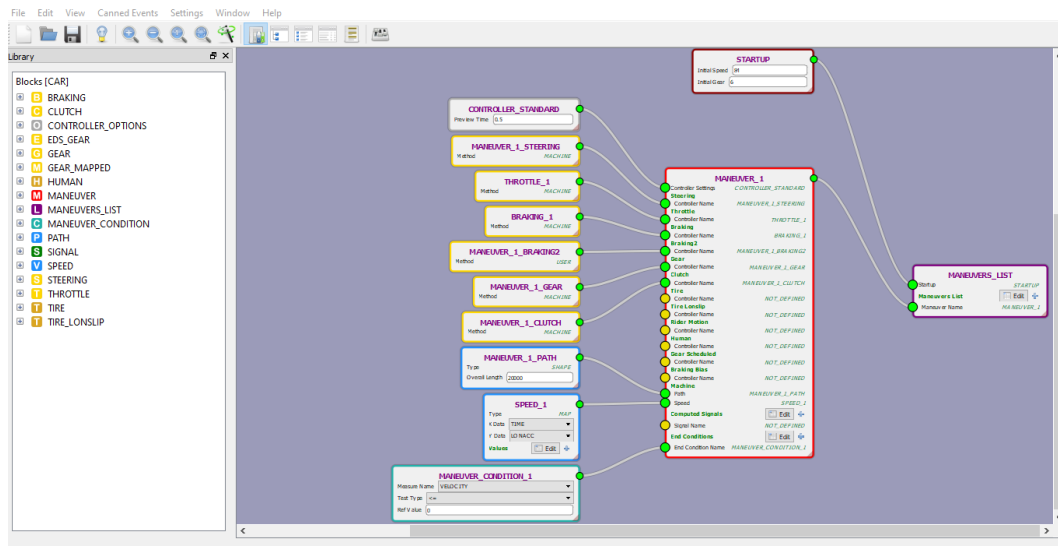


Figure 3.10: VI-CRT Event Builder

This last file was created in *VI-Event Builder* (Figure 3.10), defining a series of mini manoeuvres to be performed in succession. The test is modular from blocks such as braking, clutch, gear, steering and throttle. These commands can be open loop signals or indirectly established by modifying the trajectory, velocity and acceleration during the time manoeuvre.

Once the test configuration was ready, the event was started and the *xml* file to be used for the co-simulation was generated, as explained in paragraph 3.4.

3.4. Co-simulation VI-CRT and Simulink

A particular VI-CRT interface enables users to easily connect their vehicle model to several accessories, plugin or systems developed in MATLAB/Simulink. The latter possibility was exploited to activate the TV system: co-simulation between the vehicle built in VI-CRT and the control in Simulink was used.

Once the vehicle setup has been prepared and event started, the file `<event_name>_send_svm.xml` is created. The VI-CRT car model is made available in the MATLAB/Simulink environment as an s-function, that represents the car plant with inputs and outputs that can be connected to other blocks in the Simulink (Figure 3.11).



Figure 3.11: Block of VI-CRT in Simulink [8]

The VI-CRT car data is retrieved from a string variable called `vicrt_inputfile` through the field Input file. When the Simulink computation starts, the “xml” file is used to recover the model and event parameters.

The VI-CRT MATLAB/Simulink interface is now a unique Simulink block that can be completely configured to set up a co-simulation or run the VI-CRT solver directly from Simulink.

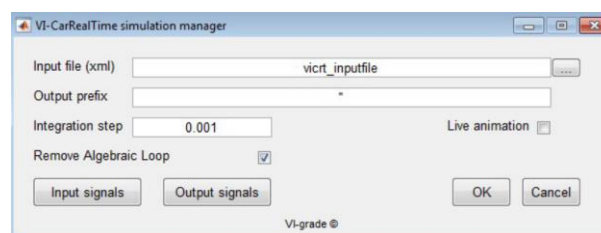


Figure 3.12: Window for `vicrt_inputfile` [8]

In the window of Figure 3.12 can not only to recall the input file xml, but also to choose the *Input* and *Output* signals (I/O). After the input file selection, the interface automatically updates the I/O bus according to the current solver information. From a hierarchical list, available in [8], it is possible to select the channels of interesting for input and output.

The selection process can be understood from Figure 3.13: the important difference between the I/O signal is that the input is used to be overwritten, while the output is used as a result file.

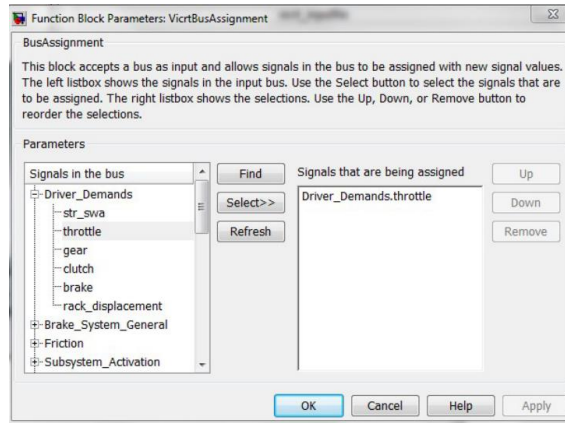


Figure 3.13: Window to select I/O channels [8]

At this point it is possible to connect these ports to the various blocks or systems created in Simulink (as in the TV control in chapter 5) and, when the model is completed, to start the co-simulation.

4. Torque-vectoring

Torque-vectoring (TV) actively controls the lateral dynamics of the vehicle through an appropriate distribution of the torques to be applied to the wheels. These, in fact, translate into longitudinal forces causing a yaw moment on the vehicle. This technology can be developed to reach different targets, including improve vehicle stability, safety, handling capability and energy efficiency. TV is applicable to any vehicle regardless of the type of transmission (AWD, FWD or RWD), if it is equipped with a device capable of varying the distribution of torque between the wheels (differentials, brakes, electric motors, etc).

4.1. History and state of art

The phrase “Torque Vectoring” was first used by Ricardo in 2006 SAE 2006-01-0818 in relation to their driveline technologies. The technological idea was built on the basic principles of a standard differential, conducting both basic differential tasks and transmitting torque independently between the wheels: this transferring ability improved handling and traction in almost any situation. Originally TV differentials were used in racing: Mitsubishi rally cars were some of the earliest to use the technology [10].

The TV with the ICE provided for a torque distribution starting from the total one imposed by the operating conditions of the engine: therefore, the torque split had quite limited operating ranges. Following the progressive diffusion of electric motors in the automotive sector, the potential of vehicle control systems and of TV have expanded ever more: in particular, more flexible solutions are preferred with individual wheel electric motors. If a single or double speed gearbox is placed between the electric motor and wheel, the configuration is commonly defined as *on-board motors* architecture. While if the motors are mounted directly inside the wheels, it is referred as *in-wheel motors* configuration which further increases the driveline packaging effect with

respect to conventional one [11]. The first solution is used for the present hybrid vehicle.

Current electric vehicle studies are investigating several powertrain configurations constituted by one, two, three or four electric motors individually controlled with different performances in terms of handling in steady state and dynamic conditions.

In Figure 4.1 all these possible layouts are visible. Vehicles are referred as $n_{mot}F - n_{mot}R$, where $n_{mot}F$ is the number of motors on the front axle and $n_{mot}R$ is that on the rear axle. As already mentioned in paragraph 3.2.3, the architectural solution of this car for electric motor is 2F-0R: hence, two single motors rather than an active differential [12].

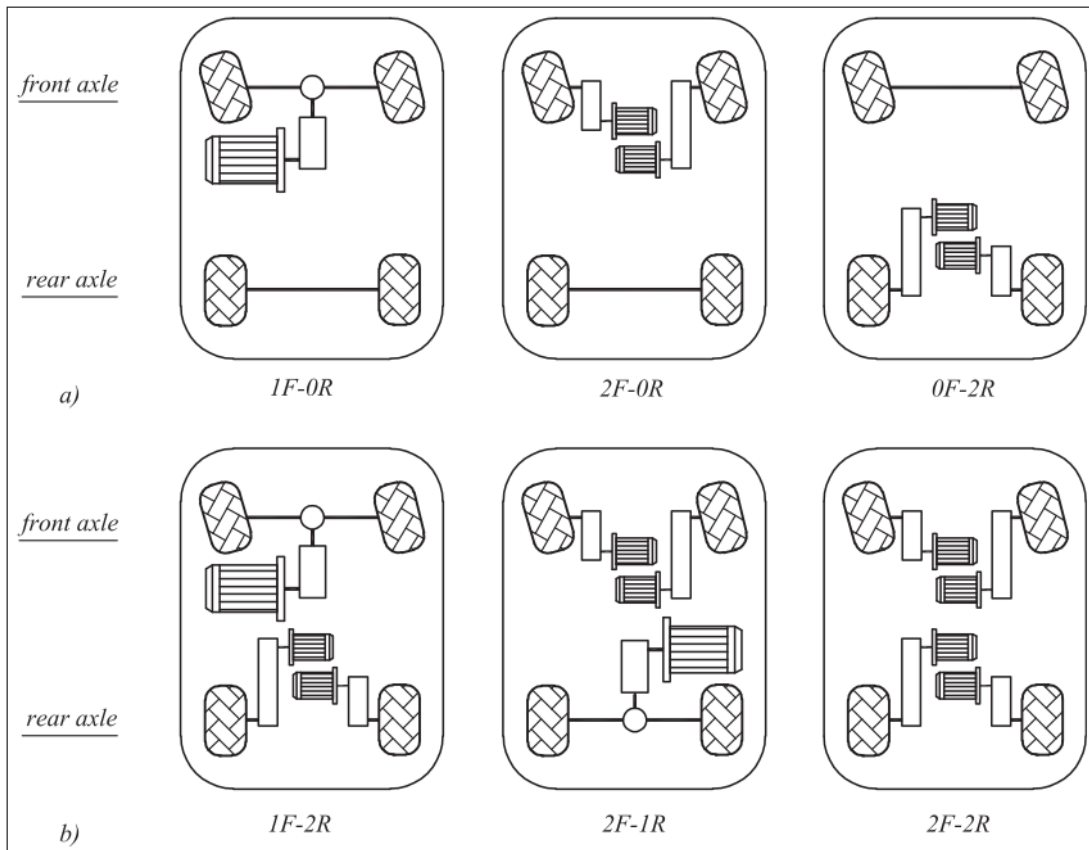


Figure 4.1: Examples of vehicle layouts with one to four electric powertrains [12]

The TV actuated through individual motor control is more effective than active differentials: in fact, the latter have limitations in terms of dynamic response, maximum allowable torque transfer, efficiency and flexibility in the torque transfer direction in the case of a significant speed difference between the sun gears.

The design of the cornering response of fully electric vehicles (FEVs) can be carried out mainly at the control level as the traditional tools for handling tuning (e.g. the adjustment of the suspension parameters) produce a marginal effect compared with the continuous TV actuation of the electric motor drives. Individually controlled powertrains in FEVs allow significant improvements also in terms of vehicle architecture, packaging, and energy management [13].

The TV can be considered an active safety function: these systems change the vehicle behaviour in such a manner as to make it less likely that the driver will experience an accident [14]. In fact, it is an evolution of the electronic stability control (ESC), introduced as a vehicle control system in parallel with the electronic differentials, but with limited capabilities since the control actuators, the brakes, reduce the torque on the wheels: hence, they can work in one direction only [11].

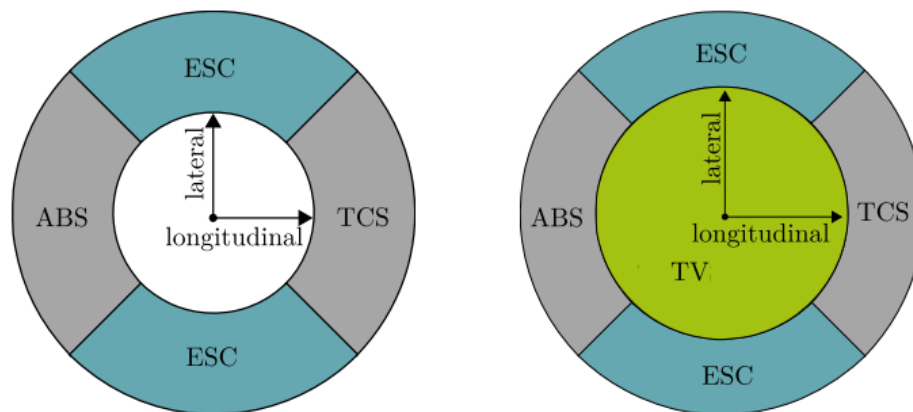


Figure 4.2: Active safety activation using ABS, TCS and ESC. At right also including TV [14]

Others active system are traction control system (TCS) and anti-lock braking system (ABS). All these systems have safety functions aim to boost vehicle movement given the physical constraints arising from limited tire forces. The active safety tasks for improving vehicle behaviour can be combined, as graphically indicated with the left circle in Figure 4.2: ABS is active during demanding braking manoeuvre, while ESC for strong lateral requests. Instead, the TV can be employed in most operating ranges (at right of Figure 4.2): not only used in safety-critical situations, but also together with ABS, TCS and ESC [14].

4.2. Control strategies

As argued in the previous paragraph, the implementation of the TV can take place according to different layouts: for this reason, also depending on the objectives to be achieved, in the literature there are various control strategies.

Before analysing the controller algorithm, it is useful to review the inputs and outputs of different TV designs [14]. Most of the papers available on this topic control the yaw rate r of the vehicle, in combination with the sideslip angle β especially for sports cars. The first is realized to achieve a desired handling behaviour, the second to maintain vehicle stability during emergency conditions. Other less popular applications try to minimize tire forces in longitudinal and lateral directions or to intervene on the vehicle speed.

Almost all these systems have the yaw moment M_z as their output variable, generated by wheel force differences between the left and right side of the vehicle. These forces are created depending on the layout and control: they can be produced by different actuators, differentials, brakes or a combination of these.

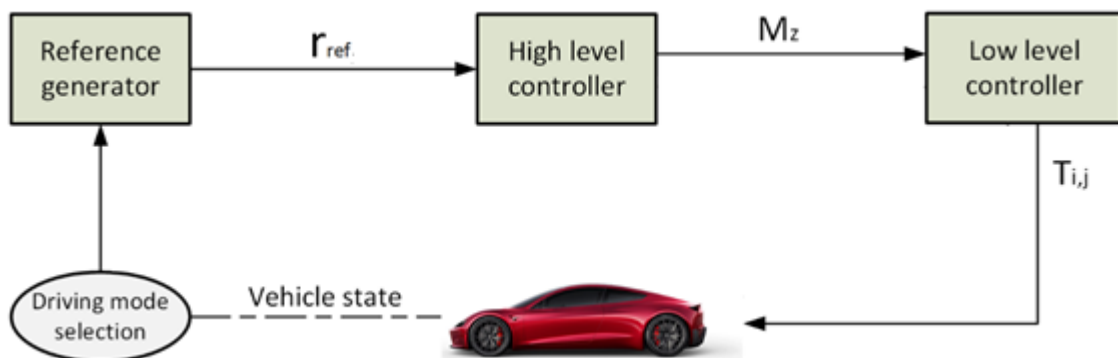


Figure 4.3: Typical structure of a TV controller (adapted from [15])

The passage from inputs to outputs is determined precisely by the chosen control strategy. In Figure 4.3 is illustrated the typical structure of a TV controller according to the scientific literature. It mainly consists of three blocks: *reference generator*, *high level controller* and *low level controller*. A series of data is extrapolated or estimated from the *vehicle* to achieve the target that the driver chooses with the *driving mode selection* [16].

Merging the vehicle parameters with inputs the driver's command, in the *reference generator* is calculated the desired quantity that the controller tries to follow applying TV. To modify the response during cornering, the design of this first block can happen through the understeer characteristic with the objectives [17]:

1. to reduce the understeer gradient with respect to the passive vehicle (i.e. the same vehicle plant without the TV controller);
2. to extend the region of linear cornering response;
3. to expand the range of possible lateral accelerations for the available tire-road friction conditions.

In general, the vehicle response to a steering input is linear within about 0.5 g of lateral acceleration [18]. In Figure 4.4 it is shown with the two dashed curves as targets just explained can be achieved through the implementation of individual electric motor control.

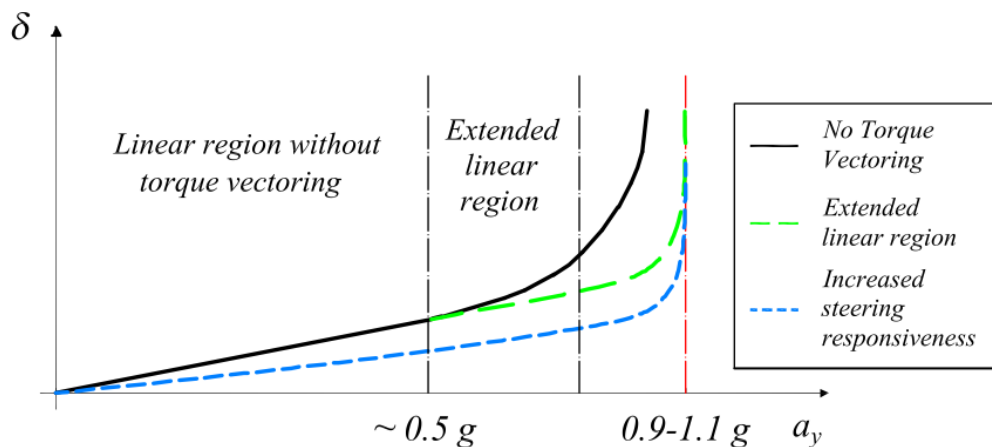


Figure 4.4: Potential modifications of vehicle understeer characteristic achievable through TV [18]

By several settings of the reference generator can be ensured distinct car behaviour and obtained different driving configurations as in [16]. Depending on environmental conditions and personal preference, a change of modes by the driver could enhance the fun-to-drive, improve energy efficiency or ensure more safety for low friction conditions. In the latter case, a reference sideslip angle β or its control may be necessary in order to cope with critical conditions, extend the limit of stable cornering and allow high values of β [17].

Various strategies for calculating this reference have been presented in the literature: some as [19] exploit the single track model, while other papers as [20] are based on a quasi-static model, which requires the time derivatives of the roll angle θ , sideslip angle β and longitudinal slip ratio of the i -th wheel σ_i are zero. In this work the reference is obtained as in [16], through an analytical formulation of the understeer gradient.

The *high level controller* takes the references, compares them with the current values of the vehicle and tries to minimize the difference between them, by means an appropriate control law: the result is the yaw moment M_z . A TV controller is particularly sensible to the error estimation of the vehicle state [15]: indeed, if incorrect the command produced may lead to vehicle instability due to wrong reference generation. In [14] the different controllers used in the literature for TV are briefly discussed: feed forward, PID, sliding mode, predictive, fuzzy, LPV, optimal and robust control.

The *low level controller* is responsible for the allocation of the yaw moment M_z , calculated in previous, to the actuators present in the car connected to the wheels (brakes, differentials or electric motors). If multiple actuators are chosen to implement the TV, an optimization method is needed to allocate M_z between them. So, it is important to establish which physical phenomena are to contemplate in the control torque allocator: the most important is to respect the relation with the desired reference.

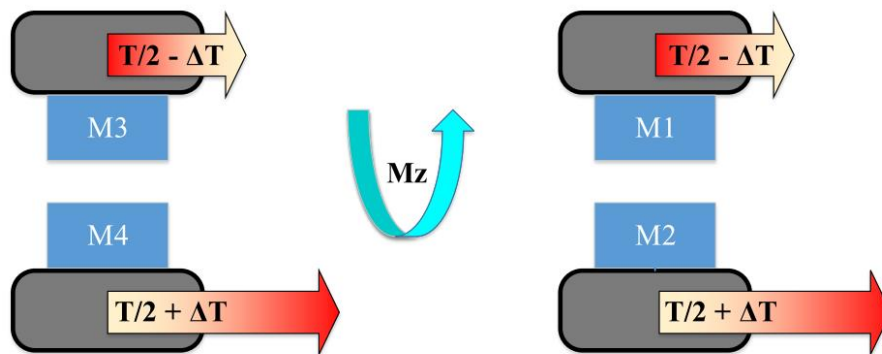


Figure 4.5: Scheme of TV application for a 4WD FEV with individual onboard electric motors [11]

To influence the dynamic behaviour of the vehicle, a generic scheme like the one in the Figure 4.5 applies: this shows the effect of the right-and-left TV system for a 4WD FEV and valid also for the hybrid vehicle in question where the TV is possible only at the front, since here the electric motors are present. The process works by controlling the direction and magnitude of torque transmitted between the left and right wheels (this is called “Torque vectoring”), which results in driving force ΔT acting on one wheel and braking force $-\Delta T$ acting on the other [11].

To realize this operation, first M_z must be transformed from torque around the vertical direction z of the vehicle to the wheel ΔT and after to combine this torque with the total drive/brake request $T/2$ that comes from the driver’s action.

To achieve this handling objective, the allocation strategy could also be different: add only torque to the right wheel or remove it from the left one. Of course, it depends on the type of actuator, but if there are electric motors in the vehicle it is convenient to add ΔT on one side and remove it on the other so as not to modify the total torque required by the driver [15].

The distribution factor between right and left in the case of Figure 4.5 is kept at 0.5 which means the same ΔT is added on one side and subtracted from the other. In [20], for example, it is explained that this coefficient can be found by minimizing through cost functions or with the approximated computation of equations that asymptotically tend to the optimal one. These solutions try to minimize various aspects: the overall input motor power, the longitudinal tire slip with respect to the average slip k of the four wheels, the total longitudinal slip power loss and the sum of tire force coefficients.

Finally, in the *low level controller* can be considered a set of constraints including the torque and power limitations of the electric drivetrains, the power restriction of the energy storage unit and the limitations relating to the tire friction ellipse starting from a simplified estimation of the load transfers [20].

5. Control system

Once the bibliographic search of the various strategies was completed, a TV logic was devised for the vehicle examined in paragraph 3.2. The control, built in Simulink (Figure 5.1), is composed of the three macro blocks described in chapter 4 and for each of them one of the previously presented solutions has been chosen.

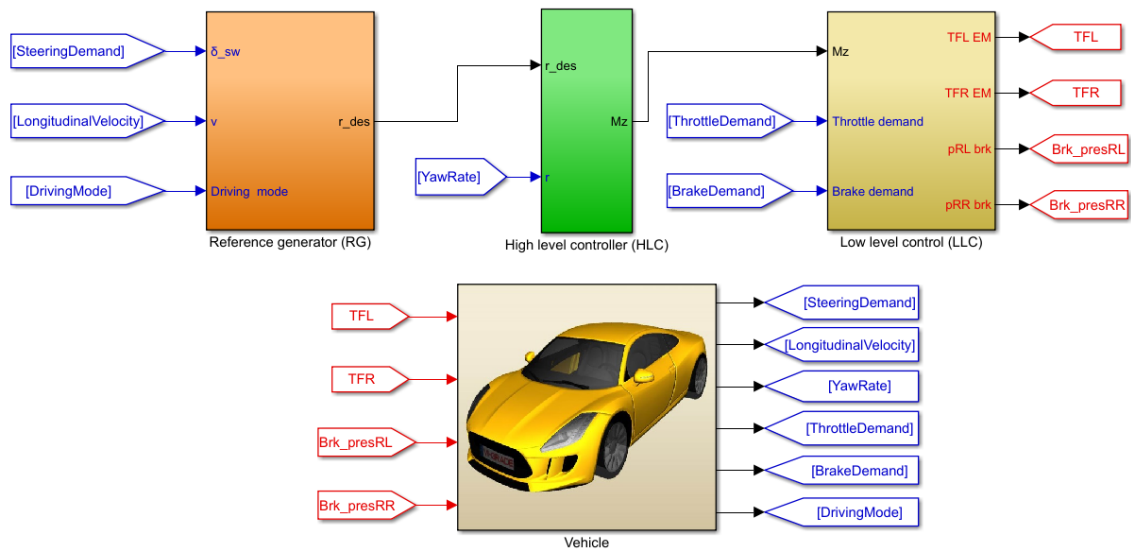


Figure 5.1: TV controller Simulink model

In the *reference generator (RG)* is produced the desired yaw rate r_{des} in function of SWA input of the driver δ_{sw} , the longitudinal velocity v and the driving mode. In fact, this system provides a modular control logic, with the possibility of switching between three different positions and each of them corresponding to a reference understeer characteristic. The name and goal of each configuration are:

- *Normal*, to have an identical steady state behaviour and a greater dynamic action than the passive vehicle;
- *Sport*, to obtain a better behaviour both in stationary and in transient compared to the passive car;
- *Wet*: to ensure stability and safety to the vehicle in conditions of low grip.

In the *high level controller (HLC)* the error is computed, i.e. the difference between the desired r_{des} and actual yaw rate r . The error e_r is elaborated by a PI controller obtaining the yaw moment M_z , which represents the corrective action to follow the reference.

With the criterion of influencing the dynamics of the vehicle, in the *low level controller (LLC)* M_z is distributed to the front to control the electric motors in torque. If the latter saturate, the residual yaw moment is given to the rear and transformed into braking pressure.

In the *vehicle* block there is a Simulink s-function of the VI-CRT car model: as already highlighted in paragraph 3.4, with this element the co-simulation between the two software takes place. Moreover, inputs and outputs useful for the operation of the control are connected.

5.1. Reference generator

In the *RG* is computed the desired yaw rate r_{des} in order to reach a reference understeer characteristic and so to modify the handling behaviour of the car.

As anticipated in the chapter 4, in this report the reference is determined through an analytical formulation based on the correlation with experimental data from different vehicles, where the lateral acceleration a_y is function of the dynamic SWA δ_{dyn} [16]. Equation 5.1 describes the linear part of the reference understeer characteristic and Equation 5.2 delineates the non-linear part of the understeer characteristic, which derives from tire saturation:

$$a_y = \frac{1}{K_U^{lin}(a_x, \mu)} \delta_{dyn} \quad \text{if } \delta_{dyn} < a_y^*(a_x, \mu) K_U^{lin}(a_x, \mu) \quad (5.1)$$

$$a_y = a_{y_{MAX}}(a_x, \mu) + \left(a_y^*(a_x, \mu) - a_{y_{MAX}}(a_x, \mu) \right) e^{\frac{K_U^{lin}(a_x, \mu) a_y^*(a_x, \mu) - \delta_{dyn}}{\left(a_{y_{MAX}}(a_x, \mu) - a_y^*(a_x, \mu) \right) K_U^{lin}(a_x, \mu)}} \quad (5.2)$$

if $\delta_{dyn} \geq a_y^*(a_x, \mu) K_U^{lin}(a_x, \mu)$

Where:

$$\bullet \quad \delta_{dyn} = \delta_{sw} - \left(\tau_{\delta} \cdot l \cdot \frac{a_y}{v^2} \right) \quad (5.3)$$

with the actual SWA δ_{sw} , the steering ratio τ_{δ} , the wheelbase l and the longitudinal velocity v ;

- $K_U^{lin}(a_x, \mu) = \frac{\partial \delta_{dyn}}{\partial a_y}$, is the understeer gradient in the linear region of the understeer characteristic (already debated in paragraph 2.3.1 and 2.5);
- $a_y^*(a_x, \mu)$, is the maximum lateral acceleration in the linear region of the understeer characteristic;
- $a_{y_{MAX}}(a_x, \mu)$, is the maximum lateral acceleration of the vehicle. Also, like the previous two, this variable is a function of the longitudinal acceleration a_x and tire-road friction coefficient μ .

Continuous TV control enables to achieve and design a notably different vehicle behaviour without changing the hardware [16]: in particular, different software-enabled driving modes can be offered to the driver. In this thesis, three positions are implemented and each corresponds to a understeer characteristic, setting different terms of a_y^* , $a_{y_{MAX}}$ and K_U^{lin} .

To choose these parameters, in high ($\mu = 1$) and low grip ($\mu = 0.4$) some steady state circular manoeuvres were executed on the passive vehicle through the numerical simulations of VI-CRT *Test Mode* (paragraph 3.3).

To evaluate the maximum cornering speed corresponding to the maximum lateral acceleration was carried out a steering pad. During the test the driver progressively increases the throttle demand, hence the vehicle speed, and simultaneously it adjusts the steering input in order to follow a circular trajectory with a defined radius: following the standard recommended by ISO 4138 [21], a radius of 100 m has been chosen.

The results are shown in the Figure 5.2: with $\mu = 1$ the maximum speed $v = 120 \text{ km/h}$ with $a_{y_{MAX}} = 1.02 \text{ g}$, while at low grip $v_{MAX} \cong 90 \text{ km/h}$ with the maximum lateral acceleration of 0.44 g . This last value was sampled before the trend reversal of lateral acceleration: from 28 s , in fact, due to the low μ , the vehicle becomes unstable and cannot increase speed.

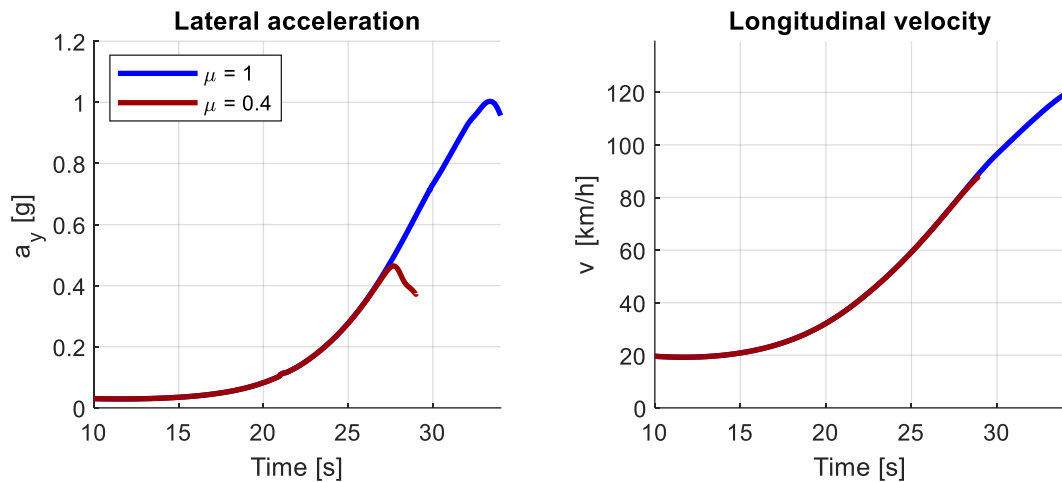


Figure 5.2: Steering pad on the passive vehicle – Lateral acceleration and longitudinal velocity

A ramp steer, instead, was performed to estimate the dynamic understeer gradient on the passive vehicle (Figure 5.3): the parameters are a SWA rate $\dot{\delta}_{sw} = 3 \text{ deg/s}$ and a speed $v = 90 \text{ km/h}$. This last value derives from the previous test because it has been seen that both in high and low grip this speed is achieved in a stable manner.

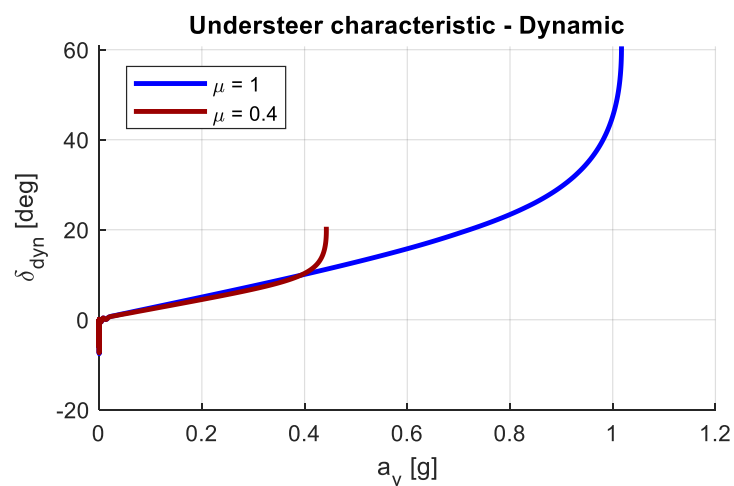


Figure 5.3: Ramp steer on the passive vehicle – Dynamic understeer characteristic

The parameters obtained from this handling diagram were fundamental in designing the reference understeer characteristic in the various driving configurations. In the Table 5.1 are reported these values.

Table 5.1: Understeer characteristic parameters for each driving mode

| Driving modes | a_y^* [g] | $a_{y_{MAX}}$ [g] | $K_U^{lin} \left[\frac{deg}{g} \right]$ | μ [-] |
|---------------|-------------|-------------------|--|-----------|
| Normal | 0.58 | 1.02 | 24.7 | 1 |
| Sport | 0.58 | 1.02 | 17.0 | 1 |
| Wet | 0.34 | 0.44 | 24.7 | 0.4 |

In *Normal*, the understeer characteristic of the vehicle without control with $\mu = 1$ is assigned. The friction coefficient is assumed to be known: in fact, a part of the control where μ is estimated has not been foreseen. Without modifying K_U^{lin} , an identical stationary behaviour and a better one in transient is obtained.

In *Sport*, a reduced understeer gradient is set, such as to increase the performance at low a_y . The other parameters are the same of *Normal* version.

Under low road/wheel friction conditions, the driver can select *Wet* mode. As in *Normal*, the understeer characteristic of the passive vehicle is assigned with the limited accelerations reached at the assumed $\mu = 0.4$. The understeer gradient, on the other hand, turned out to be slightly lower than that reached in high grip: to be in conditions of greater safety, the same K_U^{lin} of the first mode presented is required.

From the set of target understeer characteristics (Figure 5.4), the look-up tables of the desired yaw rate r_{des} , which represent the actual control variable, are computed *offline* as function of SWA δ_{sw} and vehicle speed v with the following steps:

- for the specific value of δ_{sw} and v , the lateral acceleration a_y is obtained by solving the system with Equations 5.1, 5.2 and 5.3;
- with the values of a_y and v is determined r_{des}

$$r_{des} = a_y/v \quad (5.4)$$

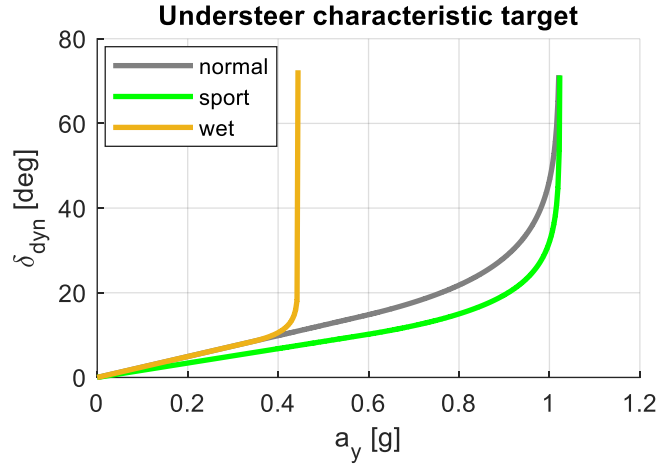


Figure 5.4: Desired dynamic understeer characteristics

To have maps independent of the steering direction, the yaw rate extracted from the look-up table (Figure 5.5) is multiplied by the δ_{sw} sign: in fact, the vehicle's behaviour must be symmetrical.

$$r_{des} = r_{des} \cdot \text{sgn}(\delta_{sw}) \quad (5.5)$$

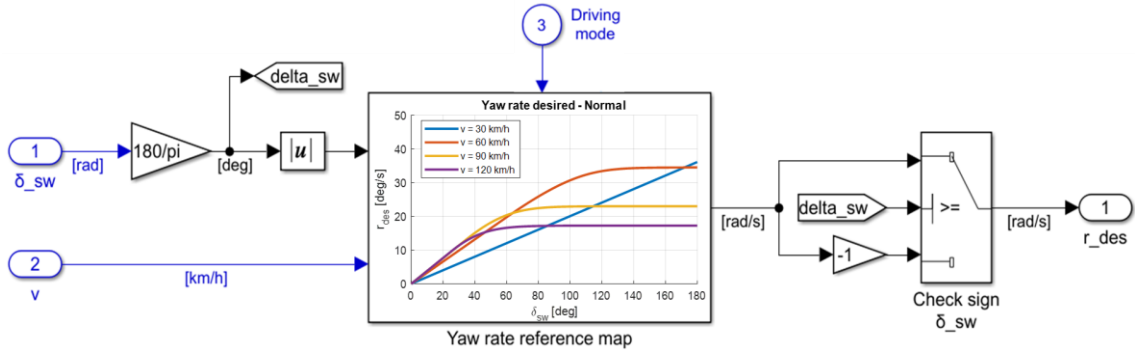


Figure 5.5: Reference generator

Since a_y^* , $a_{y_{MAX}}$ and K_U^{lin} change, the map r_{des} is also a function of the selected driving mode. Figure 5.6 shows the map for the *Normal* position. In general, since the yaw rate is function of the lateral acceleration, this map is a sort of understeer characteristic with inverted axes: a linear one, depending on the parameters a_y^* and K_U^{lin} , follows a part in which the yaw rate value remains constant since saturation has been reached (due to $a_{y_{MAX}}$). Furthermore, the dependence of the reference on the longitudinal velocity is observed: an increase in v implies a greater slope but the maximum value of r_{des} decreases (saturates first).

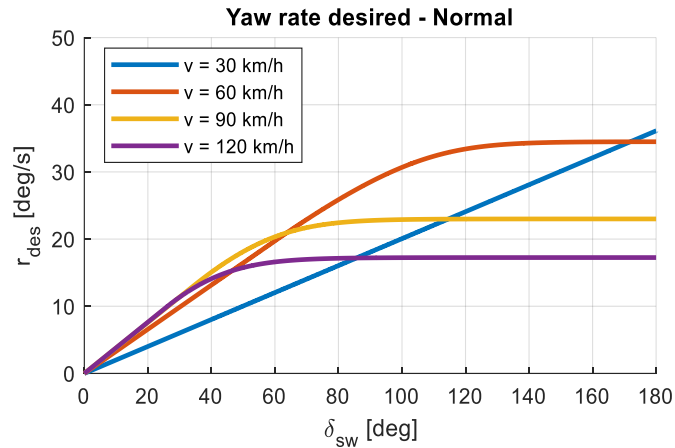


Figure 5.6: Map of the desired yaw rate – Normal mode

In Figure 5.7 the yaw rate maps for the various configurations can be compared. Having set a different K_U^{lin} , it is possible to see that the slope of the curves in the *Normal* map are smaller than in the *Sport* map, i.e. with the same SWA there is a lower yaw rate in *Normal* compared to *Sport*: consequently, in the latter the saturation limit value is reached first. This is consistent with the objective required because a vehicle with more performance is desired: setting a lower understeer gradient it takes a smaller SWA than the passive vehicle to achieve the same lateral acceleration. Having the same a_y^* and $a_{y_{MAX}}$ in the two modes, r_{des} at the same velocity ends the linear and saturation parts at the same value.

The *Wet* map, on the other hand, presents again in the linear part a slope as the *Normal* one, while the limits reached at various v are lower.

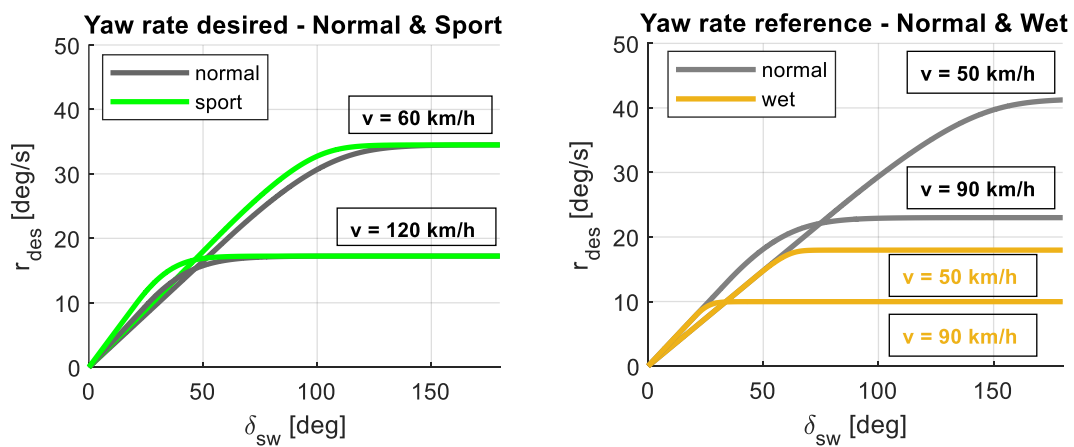


Figure 5.7: Comparison between map of the desired yaw rate

5.2. High level controller

The goal of the *HLC* consists in the calculation of the required yaw moment to follow the reference. Comparing r_{des} with the current yaw rate of the vehicle r gives an indication of an excessive or insufficient ability to follow the curvilinear path, based on the K_U^{lin} set in the *RG* for the selected mode. Making a confront means calculating the error e_r instant by instant:

$$e_r = r_{des} - r \quad (5.6)$$

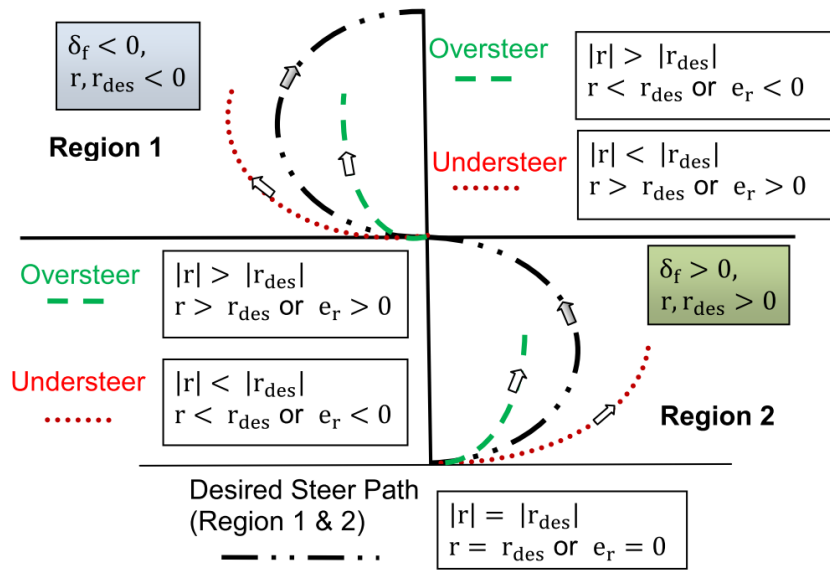


Figure 5.8: Scheme of vehicle in various scenarios and adopted sign conventions [22]

Figure 5.8 presents the car in different scenarios, including left or right hand turning and exhibiting possible understeering and oversteering behaviours [22]. Moreover, also reveals the sign conventions adopted in this thesis. Considering the example of a vehicle that curves to the left ($\delta_{sw} > 0$):

- in the case of oversteer, the yaw rate is higher than the reference ($e_r < 0$). To counteract this functioning, it is possible to increase the torque on the left wheel and decrease the right one, creating a yaw moment that opposes the steering of the vehicle and, theoretically, reduces the oversteer;

- in the case of understeer, the car has a yaw rate lower than the desired ($e_r > 0$). Reversing the sense of transfer of the previous torques generates a yaw moment on the vehicle which helps it to be less understeer.

The error e_r is processed by a proportional-integral (PI) controller. It is a control loop device that from the error, difference between a desired setpoint and a measured process variable, applies a correction based on a proportional K_p and integral K_i gain. The corrective action out of the PI is the yaw moment M_z :

$$M_z = K_p \cdot e_r + K_i \cdot \int e_r dt \quad (5.7)$$

Figure 5.9 shows the Simulink blocks that make up the *HLC* subsystem. The adjustment of the gains K_p and K_i was conducted with an iterative cycle: they were kept fixed both when the velocity and the driving mode changed.

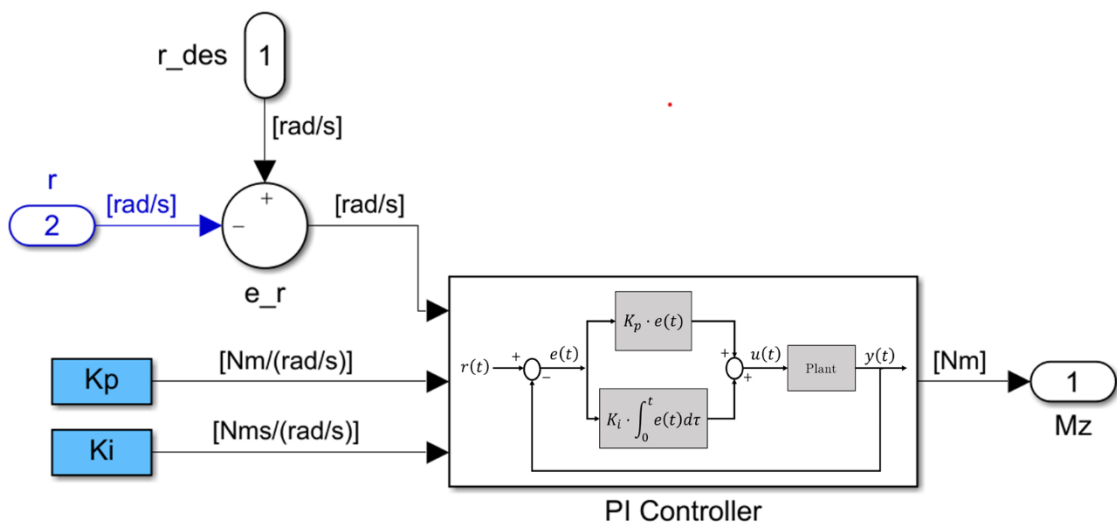


Figure 5.9: High level controller

5.3. Low level controller

The *LLC* receives the yaw moment M_z from the PI and converts it in torque to the wheels. The distribution strategy is established in such a way as to reduce the error calculated in the *HLC* and thus influence the behaviour of the vehicle depending on the driving configuration chosen. The Figure 5.10 exhibits the *LLC* structure built in Simulink.

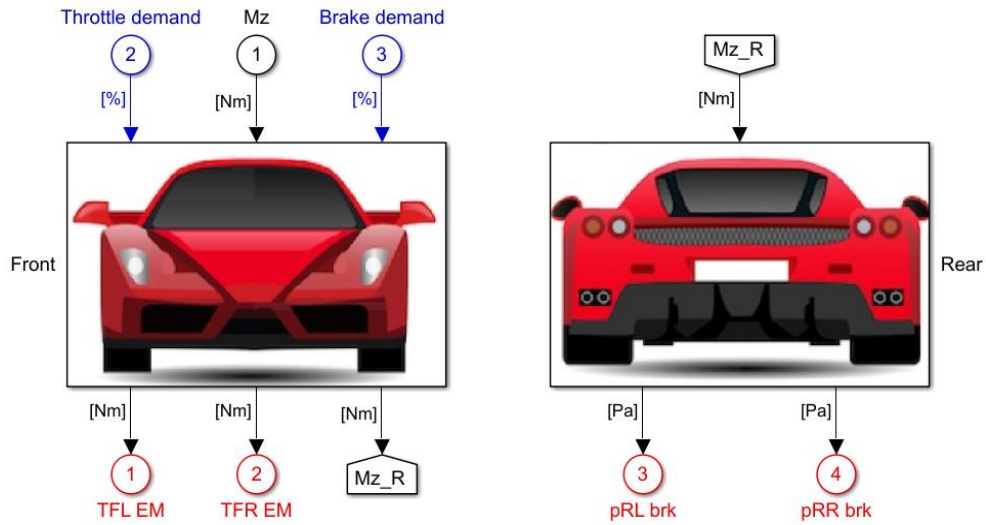


Figure 5.10: Low level controller

The actuators assigned to this task are mainly the electric motors present at the front: in fact, here the torque transfer takes place between the left and right wheel according to the value of M_z (this is the “torque-vectoring”). If the electric motors saturate, the yaw moment not exploited at the front is transferred to the rear (M_{zR}). Here there are no electric motors: therefore, the torque at the wheel obtained by rear yaw moment is translated into braking pressure. This is applied to one of the two wheels, always with the aim of following the reference calculated in the RG.

To distinguish the various parameters common to the four wheels, as in chapter 2 the subscript ij will be used, where i is F (front) or R (rear) while j is L (left) or R (right).

5.3.1. Front

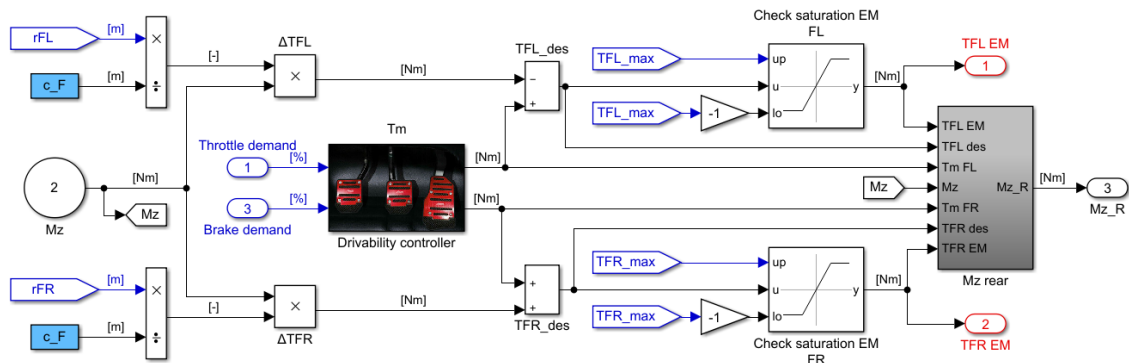


Figure 5.11: Front – Low level controller

To calculate the torque T_{Fj} to be supplied to the electric motor of each wheel, the following aspects were considered:

- the torque T_m required by the driver. Using the pedal map of the electric motors (at right of Figure 3.4), the desired torque is obtained by entering in a 2D look-up table with the driver demand throttle or brake and with the angular speed of the motors. All this part is contained in the *Front drivability controller* subsystem of Figure 5.12.

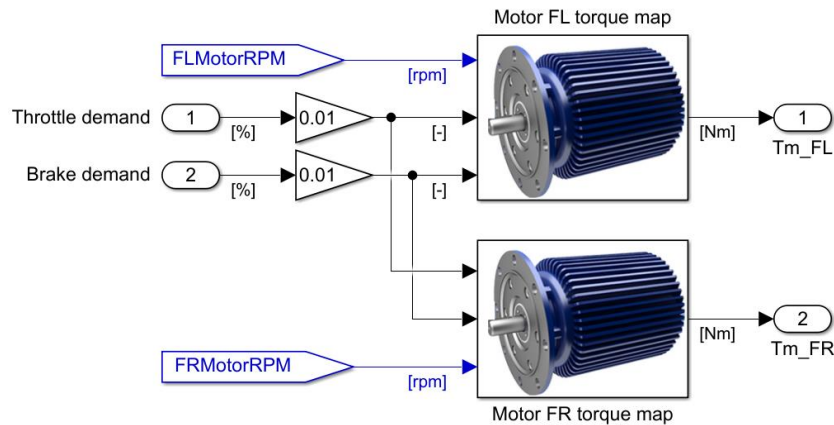


Figure 5.12: Drivability controller – Front – Low level controller

- the torque variation ΔT_{Fj} . This is calculated by translating the yaw moment M_z in torque to the wheel, by means of the front track c_F and the rolling radius of the front tire r_{Fj} .

$$\Delta T_{Fj} = \frac{M_z \cdot r_{Fj}}{c_F} \quad (5.8)$$

As seen in paragraph 2.3.1, usually a vehicle in a curve has an understeering or oversteering behaviour: both situations can be modified thanks to suitable stabilizing yaw moments and depending on the driving mode selected.

Figure 5.13 shows the torque increase that the TV control system makes on the red wheel, using the yaw moment that stabilizes the vehicle.

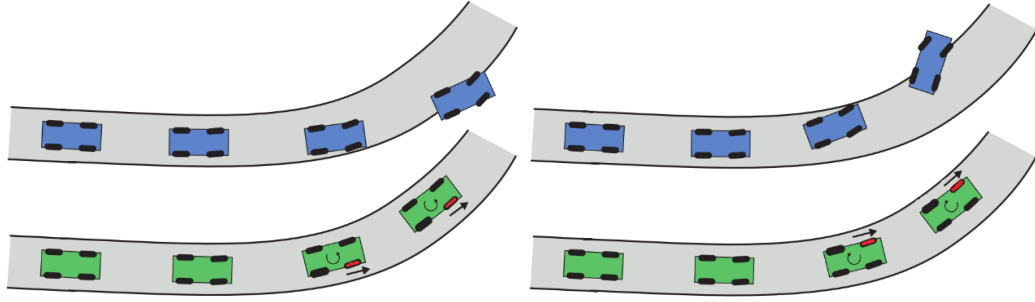


Figure 5.13: The comparison of understeer (at left) and oversteer (at right) manoeuvre without (in blue) and with (in green) TV control system (adapted from [19])

According to the convention adopted in the *HCL*, in a curve to the left ($\delta_{sw} > 0$) if M_z is positive to the driver's request $T_{m_{Fj}}$, the contribution ΔT_{Fj} is added for the outer wheel, while it is subtracted for the inner one. From this reasoning derives Equation 5.9:

$$\begin{cases} T_{FL\ des} = T_{m_{FL}} - \Delta T_{FL} \\ T_{FR\ des} = T_{m_{FR}} + \Delta T_{FR} \end{cases} \quad (5.9)$$

Not having adopted an energy criterion or another logic in addition to that of handling, no coefficient was used for ΔT_{Fj} . Furthermore, transferring this quantity from one wheel to another does not alter the total torque required by the motors (there is not a big difference between r_{FL} and r_{FR}).

Finally, with Equation 5.10 it is checked that $T_{Fj\ des}$ do not exceed the maximum and minimum torque limits imposed by the electric motor (EM) for the current rotation speed. In Simulink, this is done with a saturation block.

$$|T_{Fj\ des}| \leq T_{Fj\ MAX} = T_{Fj\ EM} \quad (5.10)$$

The check is carried out in absolute value because the electric motors have the minimum torque equal to the maximum with the same speed of rotation ($T_{Fj\ MAX} = |T_{Fj\ MIN}|$).

In the subsystem of Figure 5.14 the yaw moment actually exploited by the front wheels is calculated ($M_{z_{Fj\ act}}$), by inverting Equations 5.8 and 5.9. The only difference is in 5.8 where $T_{Fj\ EM}$ is used instead of $T_{Fj\ des}$. The residual front yaw moment is then calculated $M_{z_{Fj\ res}}$:

$$M_{z_{Fj\ res}} = M_z - M_{z_{Fj\ act}} \quad (5.11)$$

If saturation is reached with both electric motors, the maximum of the two residual front yaw moment is calculated. Since the maximum is taken as an absolute value, then the sign of M_z must be reapplied to have the true M_{zR} .

$$M_{zR} = \text{sgn}(M_z) \cdot \max(|M_{zFL\text{ res}}|, |M_{zFR\text{ res}}|) \quad (5.12)$$

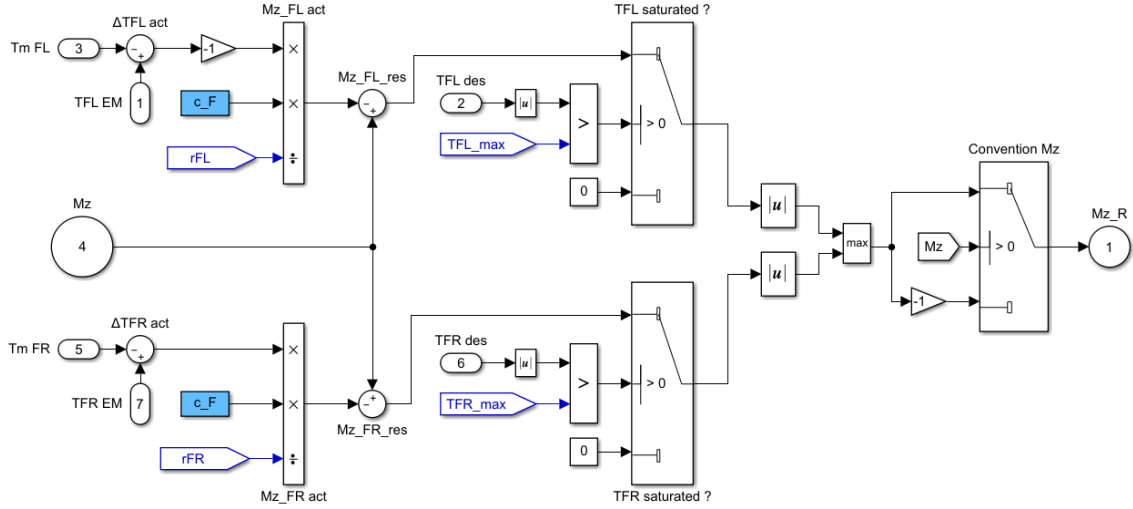


Figure 5.14: Rear yaw moment calculation – Front – Low level controller

5.3.2. Rear

The system intervenes on the rear when one of the two electric motors is in saturation. Here it is not possible to fulfil a torque control as both wheels are connected to the ICE via the differential: for this reason, the brakes are checked (Figure 5.15).

First, the moment M_{zR} is transformed into braking torque at the wheel $T_{Rj\text{ brk}}$, with an equation similar to 5.8:

$$T_{Rj\text{ brk}} = \frac{M_{zR} \cdot r_{Rj}}{c_R} \quad (5.13)$$

Where c_R is the rear track and r_{Rj} is the rolling radius of the rear tire. Furthermore, with the same convention used at the front on the left side there is a change of sign.

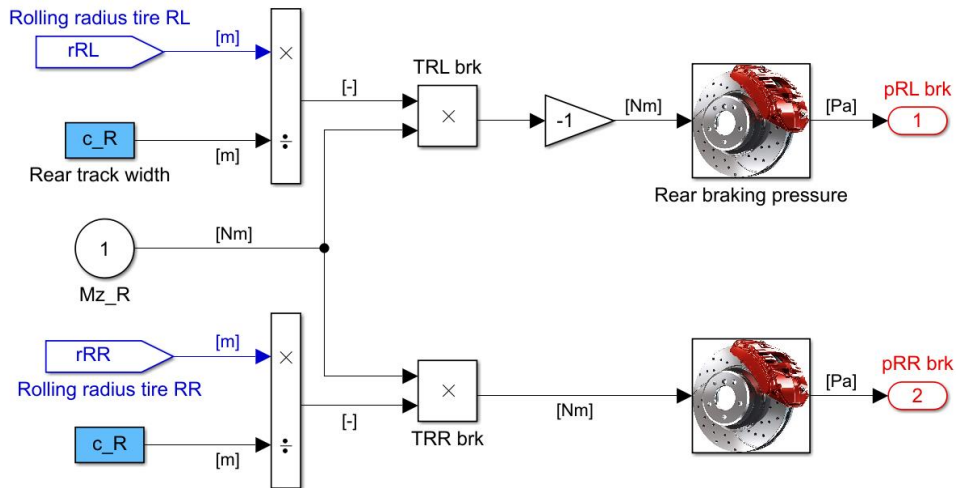


Figure 5.15: Rear – Low level controller

At this point the *Rear braking pressure* blocks in Figure 5.16 are activated: braking pressure $p_{Rj\ brk}$ will be generated only on the side where the torque is negative.

After checking that $T_{Rj\ brk}$ does not exceed the maximum rear braking moment, $p_{Rj\ brk}$ is processed with Equation 5.14, the same implemented in the VI-CRT brake model [8].

$$p_{Rj\ brk} = \frac{T_{Rj\ brk}}{2 \cdot A_{p_{brk}} \cdot \mu_{brk} \cdot R_{eff\ brk}} \quad (5.14)$$

Where $A_{p_{brk}}$ is the brake piston area, μ_{brk} is the friction pads coefficient and $R_{eff\ brk}$ is the effective piston radius.

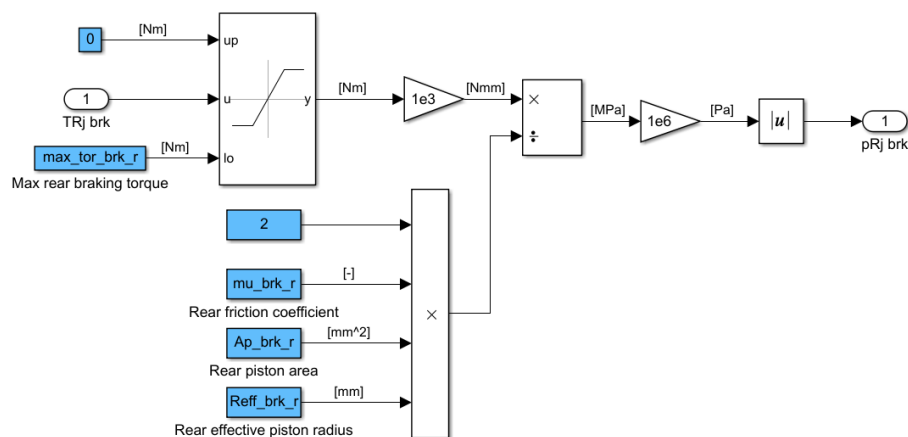


Figure 5.16: Braking pressure – Rear – Low level controller

6. Simulation results

The benefit of the TV was analysed by means of numerical simulations with *Test mode* of VI-CRT. The aim was to validate the control in steady state and transient conditions.

The manoeuvres performed are *ramp steer*, *step steer*, *sweep steer*, *powerON on cornering* and *braking in turn*. All of these are classified as *open-loop* test, which means the driver gives specific inputs to obtain the desired response, but he does not act as in a *closed-loop* to modify the control inputs to accomplish a specific task. Then, after giving the command, the driver detects the response of the vehicle as a passive spectator. The *open-loop* manoeuvres are not representative of real driving situations but are nonetheless useful for obtaining measurements of vehicle behaviour under strictly controlled and repeatable test conditions.

Each result, in the various driving modes, was compared with that obtained on the *Baseline* vehicle (called in the legends *bas*) under the same road conditions: the manoeuvres for *Normal* and *Sport* were performed at $\mu = 1$, for *Wet* at $\mu = 0.4$.

6.1. Ramp steer

Ramp steer is one of three methods for determining the steady state behaviour of the car [21]. In this test, the speed is kept constant at $v = 90 \text{ km/h}$ and the SWA is varied by $\dot{\delta}_{sw} = 3 \text{ deg/s}$. The manoeuvre time has been calibrated in order to have a maximum SWA, the input, that allows to reach the maximum lateral acceleration $a_{y_{MAX}}$ the measured variable. In *Wet* condition this time is shorter because with low friction a situation of instability is reached earlier than in the other driving configurations. As can be seen in Figure 6.1, for the convention used, steering to the left means that $\delta_{sw} > 0$.

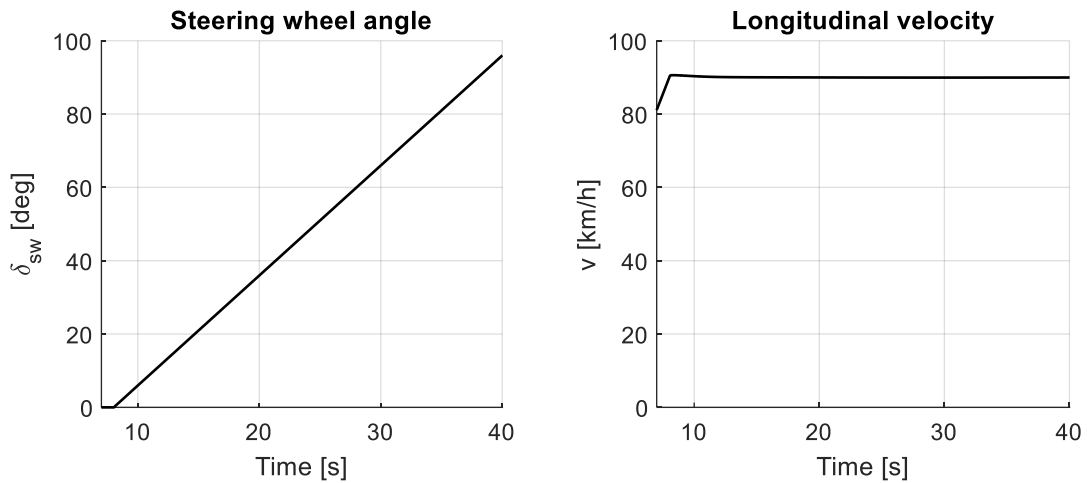


Figure 6.1: Ramp steer – SWA and longitudinal velocity

With the instantaneous v and δ_{sw} and depending on the selected driving mode, the desired yaw rate r_{des} is extracted from the look-up table of the RG . In Figure 6.2 the various trends of the yaw rate are compared.

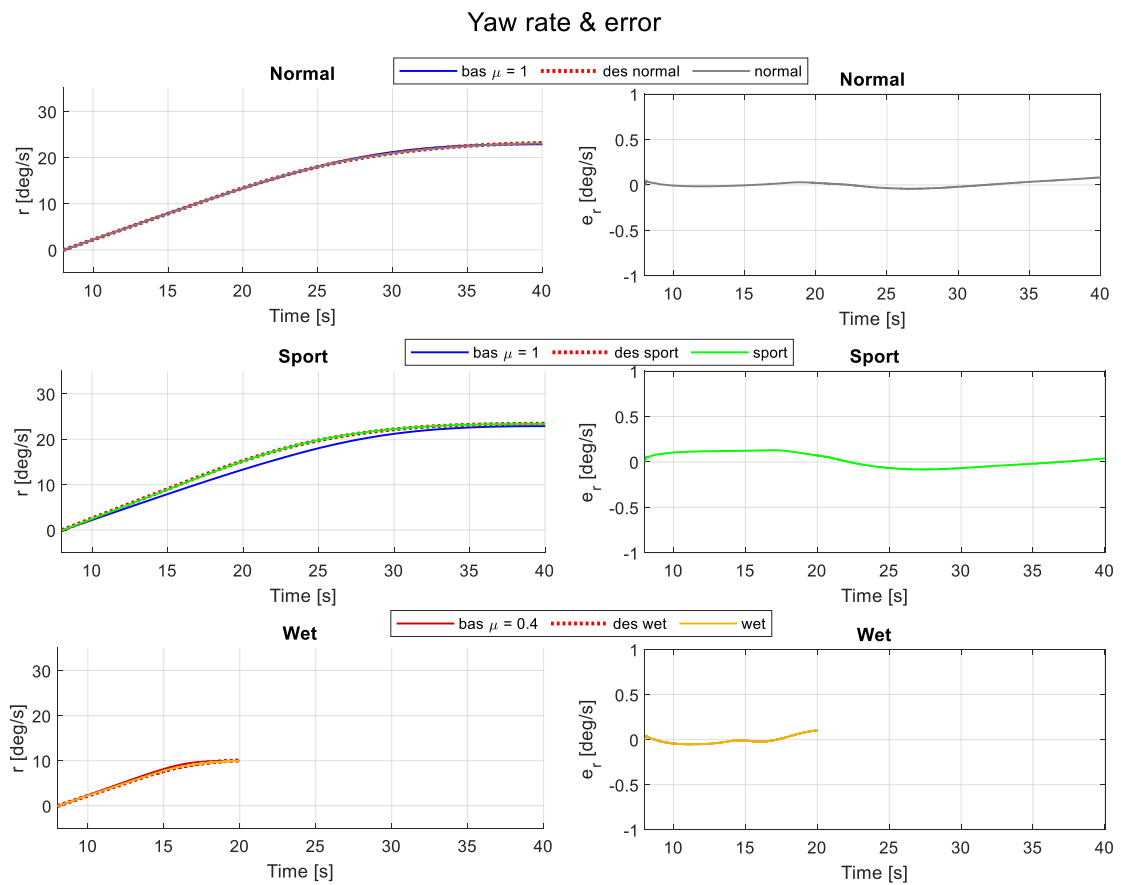


Figure 6.2: Ramp steer – Yaw rate and error

In *Normal*, the three curves are overlapped because here the same characteristic of the passive vehicle is assigned. Instead, consistently with what was designed in the *RG*, r_{des} higher than the *Baseline* (r_{bas}) are returned from the *Sport* maps due to the understeer gradient target set. In *Wet*, arguments similar to *Normal* apply. In reality, r_{des} is slightly smaller than r_{bas} , because K_U^{lin} at $\mu = 0.4$ is a little lower than that of $\mu = 1$, as already mentioned in paragraph 5.1. Then the same understeer gradient obtained with the vehicle in high grip was set.

In all driving modes the current yaw rate value overlaps the reference: the natural consequence is that the error always tends to zero.

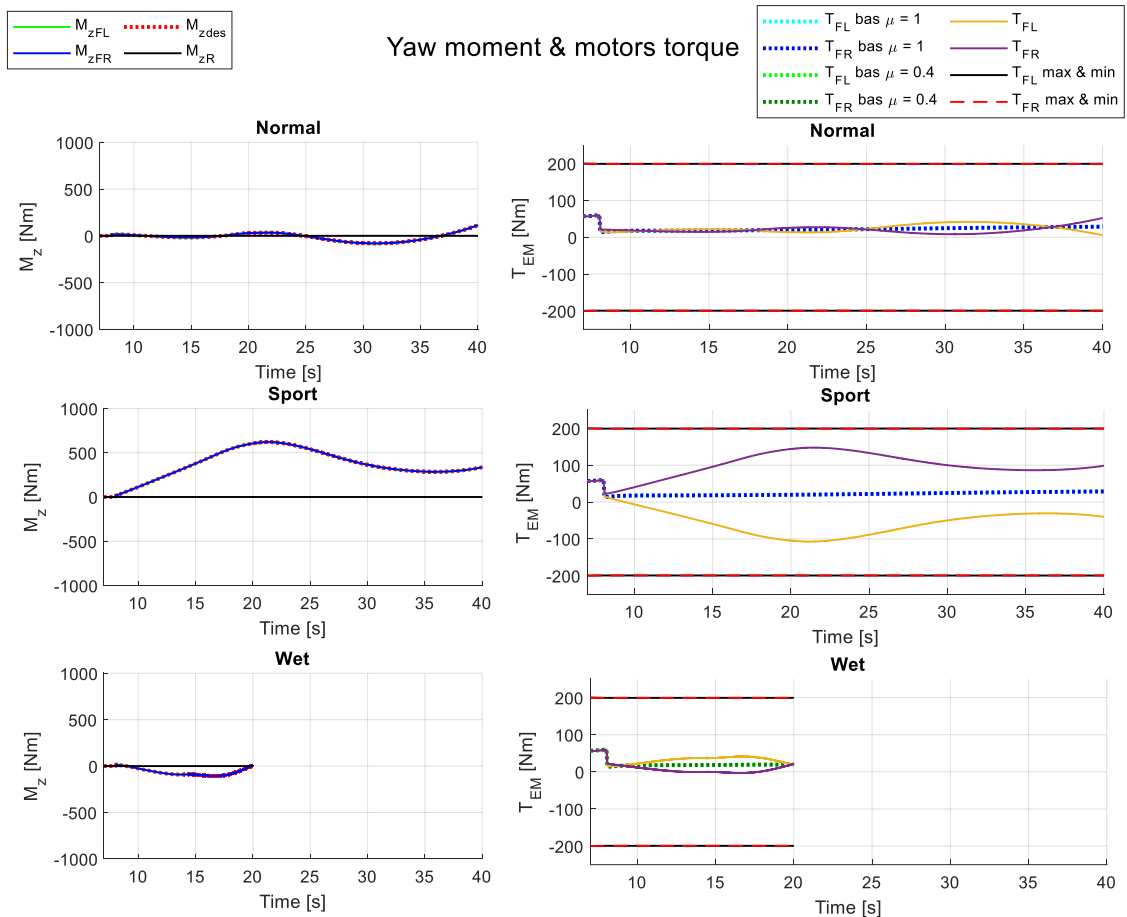


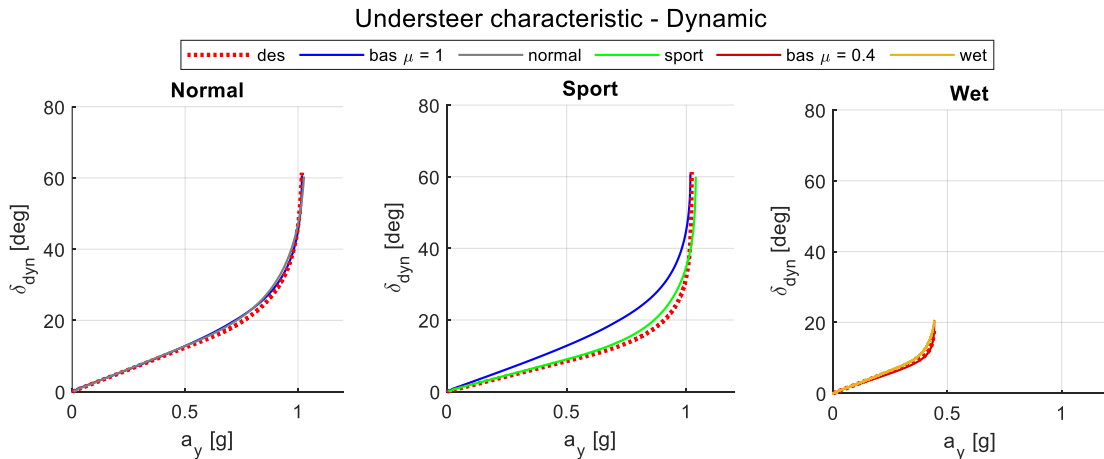
Figure 6.3: Ramp steer – Yaw moment and electric motors torque

The yaw moment M_z changes the torque of the electric motors connected to the front wheels (Figure 6.3).

In *Normal*, M_z is around zero and so also the torques of the electric motors are similar to those with the control disabled (T_{Fjbas}) because the reference is generated on the understeer characteristic of the passive vehicle. In *Sport* M_z is positive: for the *LLC* logic it means that the controller is trying to get more oversteer than *Baseline*. For this reason, more torque is delivered to the outer wheel (T_{FR}) and less to the inner one (T_{FL}). In *Wet* the yaw moment is negative because a more understeer reference is followed: then the torque of the inner wheel is higher than the outer one.

Finally, it is observable that the curves M_{zdes} , M_{zFL} and M_{zFR} are overlapped for each driving mode: this means that no electric motor is saturating, the yaw moment M_{zR} is zero and rear brakes do not intervene.

As discussed in [18], the analysis of the vehicle cornering capability is conducted through the trend of the understeer characteristic. As requested in the *RG*, in the linear part the characteristic of the passive vehicle and the *Normal* one is coincident. In *Sport*, on the other hand, more oversteer was desired and was achieved because a lower δ_{dyn} is needed to reach the same a_y as the *Baseline*. The opposite occurred in *Wet* for the reasons explained above. Furthermore, these curves in Figure 6.4 are compared to the desired understeer characteristic, designed in the *RG*.



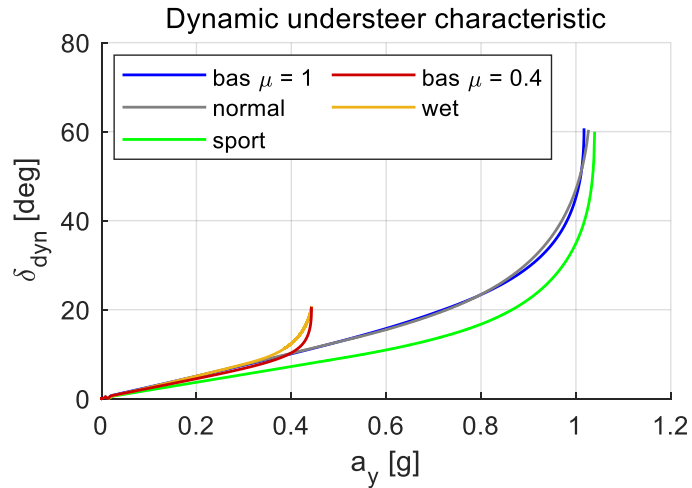


Figure 6.4: Ramp steer – Dynamic understeer characteristic

From the car's trajectory (Figure 6.5), these behaviours described above are clearer: after the initial straight stretch, the curve drawn by the vehicle is completely overlapped on that of the *Baseline* in *Normal*, more closed in *Sport* and slightly more open in *Wet*.

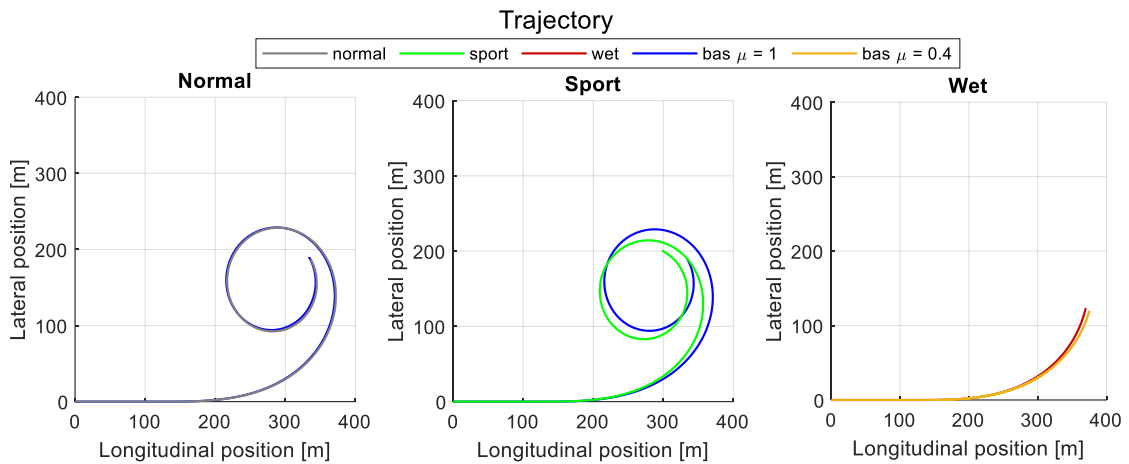


Figure 6.5: Ramp steer – Trajectory

The Table 6.1 quantitatively shows the understeer gradients referred to the dynamic SWA δ_{dyn} for each configuration. These were measured in a linear field of lateral acceleration, that is from $0.15 g$ to $0.3 g$. It is noted that the errors with respect to the targets set (Table 5.1) are between 1.5% and 3.5%, another sign that the control is actually working.

Table 6.1: Ramp steer – Resulting dynamic understeer gradient

| Driving modes | $K_U^{lin} \left[\frac{deg}{g} \right]$ | $e_{K_U^{lin}} [\%]$ |
|---------------|--|----------------------|
| Normal | 27.0 | 1.5 |
| Sport | 20.4 | 1.9 |
| Wet | 27.5 | 3.4 |

In Figure 6.6 are presented the other handling diagrams. The sideslip, roll and yaw angles take on values that do not lead to instability: in fact, they fall within the range recommended in [21]. In each version the trends are also regular until maximum lateral acceleration is reached. The absolute value of steady state sideslip angle is barely larger in *Sport*, a desirable feature of this driving mode.

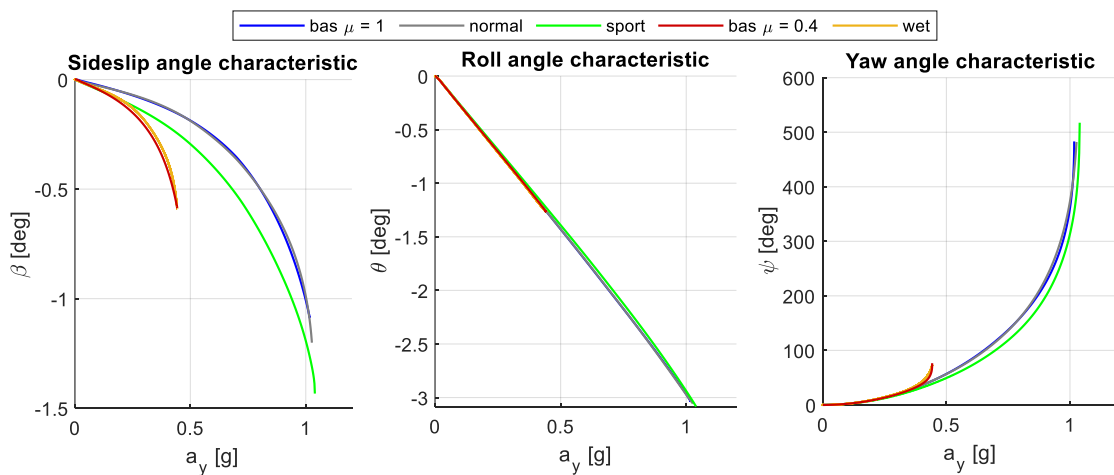


Figure 6.6: Ramp steer – Sideslip, roll and yaw angle characteristic

Figure 6.7 exhibits the curves of the longitudinal forces on the wheels. Their trend follows that of the torques of motors: at the front like the electric ones and at the rear like the ICE one. Since the control takes place only for the front when the manoeuvre begins between the different modes the values of the forces $F_{x_{FL}}$ and $F_{x_{FR}}$. In *Sport*, the forces of the right wheels (external part) increase and the left one (internal part) decreases to have more oversteer.

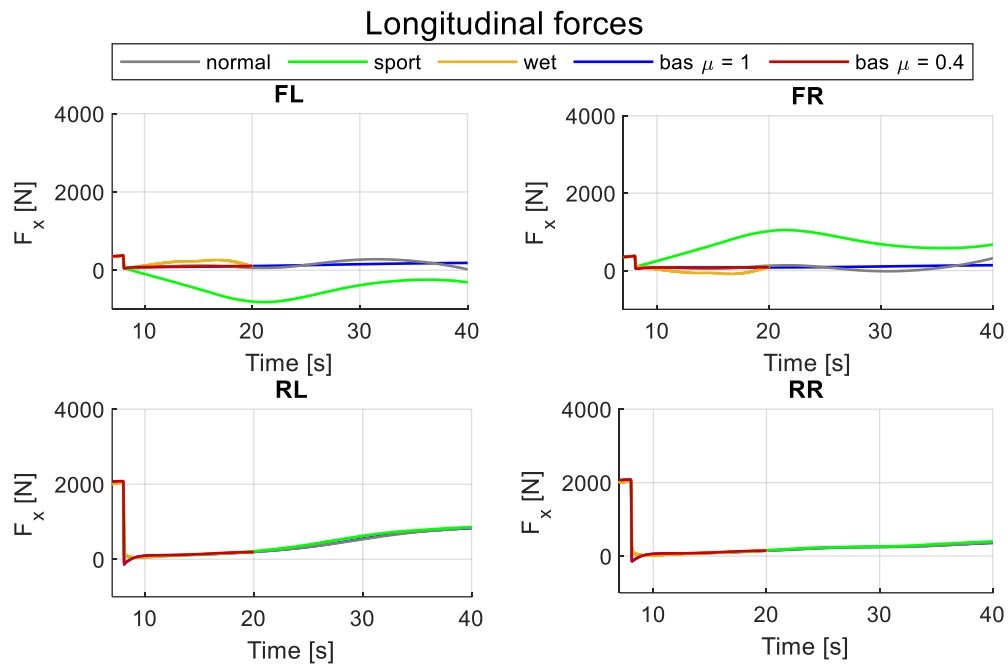


Figure 6.7: Ramp steer – Longitudinal forces

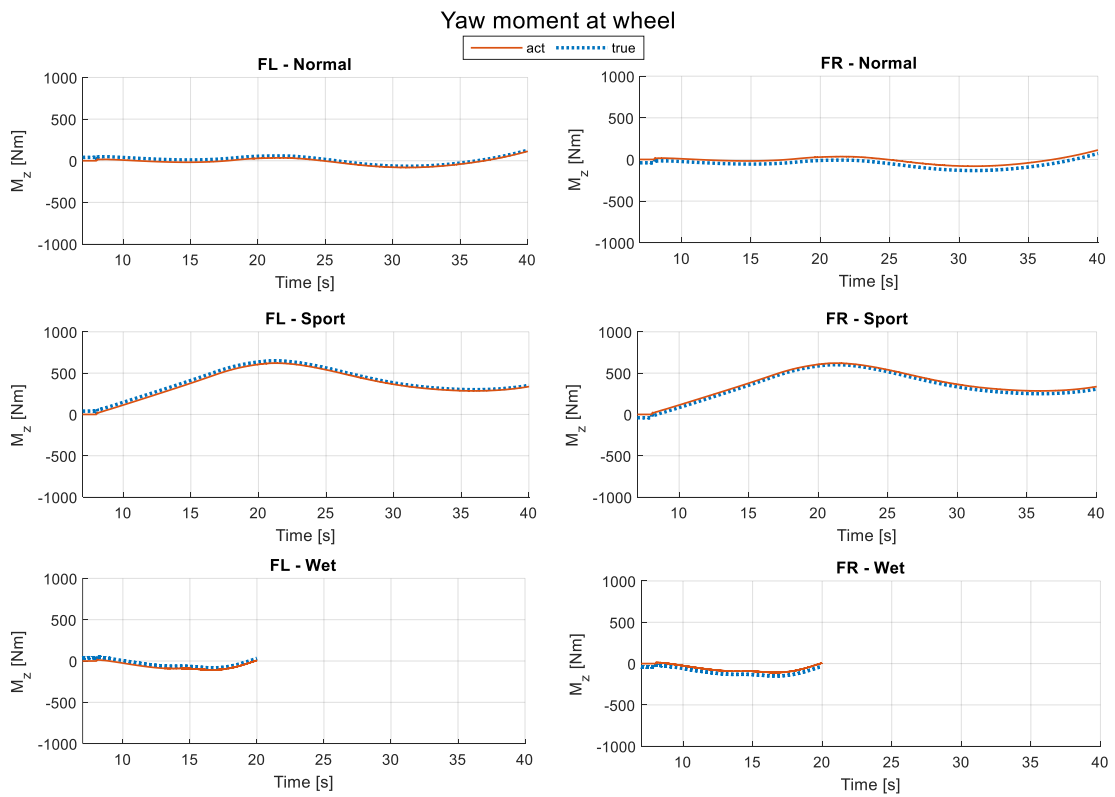


Figure 6.8: Ramp steer – Comparison between desired and actual yaw moment

Knowing the longitudinal forces, the yaw moment actually generated on the front wheels ($M_{zFj\ true}$) was calculated:

$$M_{zFj\ true} = \left(\frac{F_{x_{Fj}}}{\tau_{EM}} \cdot r_{Fj} - T_{m_{Fj}} \right) \cdot \frac{c_F}{r_{Fj}} \quad (6.1)$$

Where τ_{EM} is the transmission ratio between electric motor and wheel. The other parameters have already been introduced in paragraph 5.3.1. In Figure 6.8 it emerges that the curves $M_{zFj\ true}$ are in practice superimposed on the $M_{zFj\ act}$, an indication that what was desired in the *HLC* has been achieved.

The curves of F_y are proportional to the lateral acceleration a_y (Figure 6.9): when the driver begins to steer, these become larger and larger until they reach saturation (in correspondence with $a_{y\ MAX}$). The values are higher for the outer wheels due to load transfers.

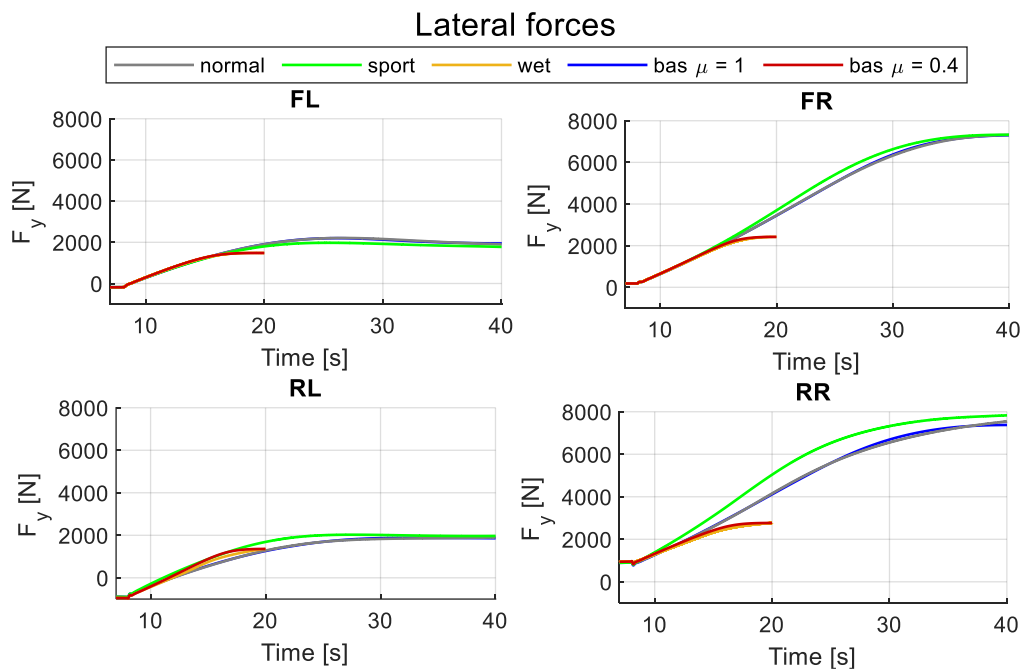


Figure 6.9: Ramp steer – Lateral forces

6.2. Step steer

With the step steer evaluates the ability of TV controller in a transient condition [18].

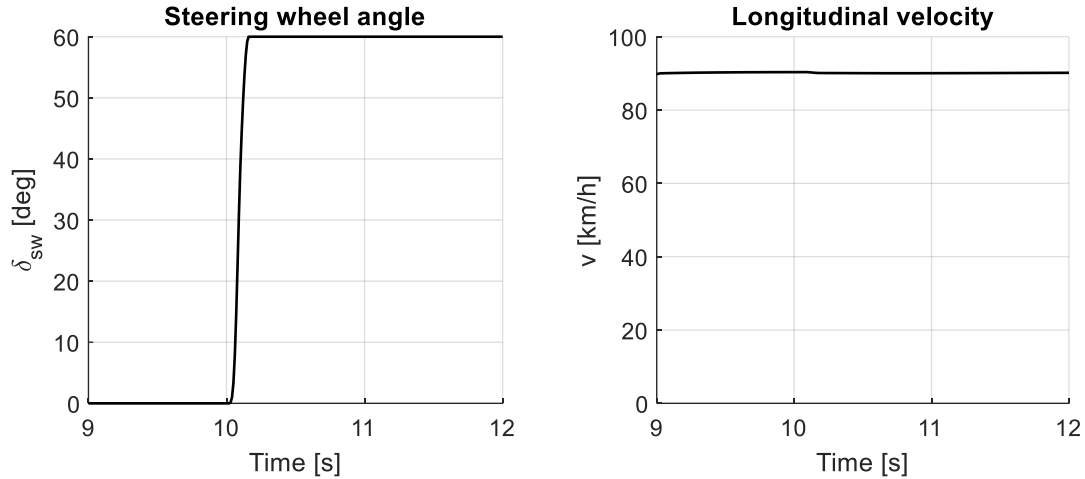


Figure 6.10: Step steer – SWA and longitudinal velocity

The vehicle is driven at constant speed $v = 90 \text{ km/h}$ and the step is applied with a rate of 400 deg/s . The final steering value, 60 deg , is held for 5 s and has been chosen to reach the maximum lateral acceleration allowed by the friction coefficient (Figure 6.10).

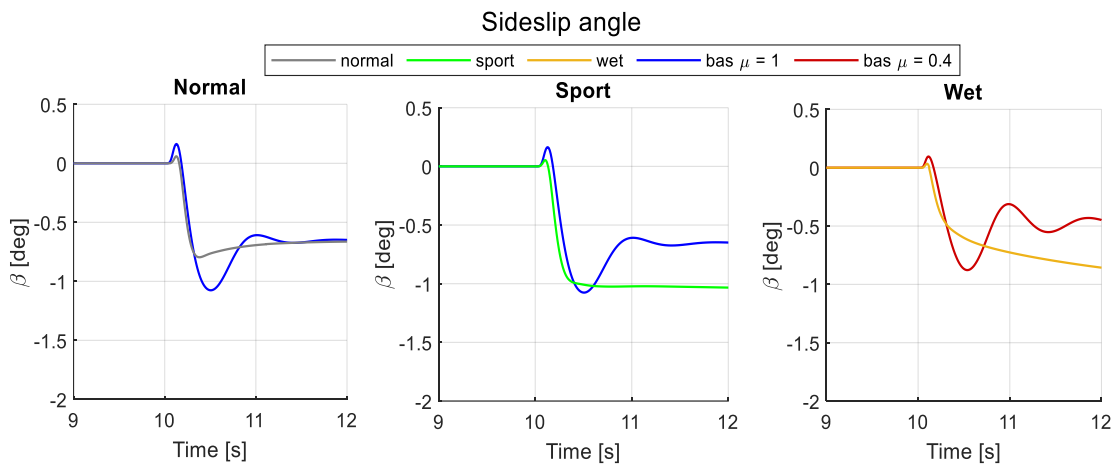


Figure 6.11: Step steer – Sideslip angle

In Figure 6.11 it is clear how the control allows to reduce the overshoot that occurs in *Baseline*: consequently, the settling time is much shorter. In *Sport*, after the transient, β is bigger but is a result already achieved with the ramp steer.

In *Wet*, it is not possible to guarantee a sideslip angle lower than *Baseline*, in any case it does not appear to be a value that brings instability.

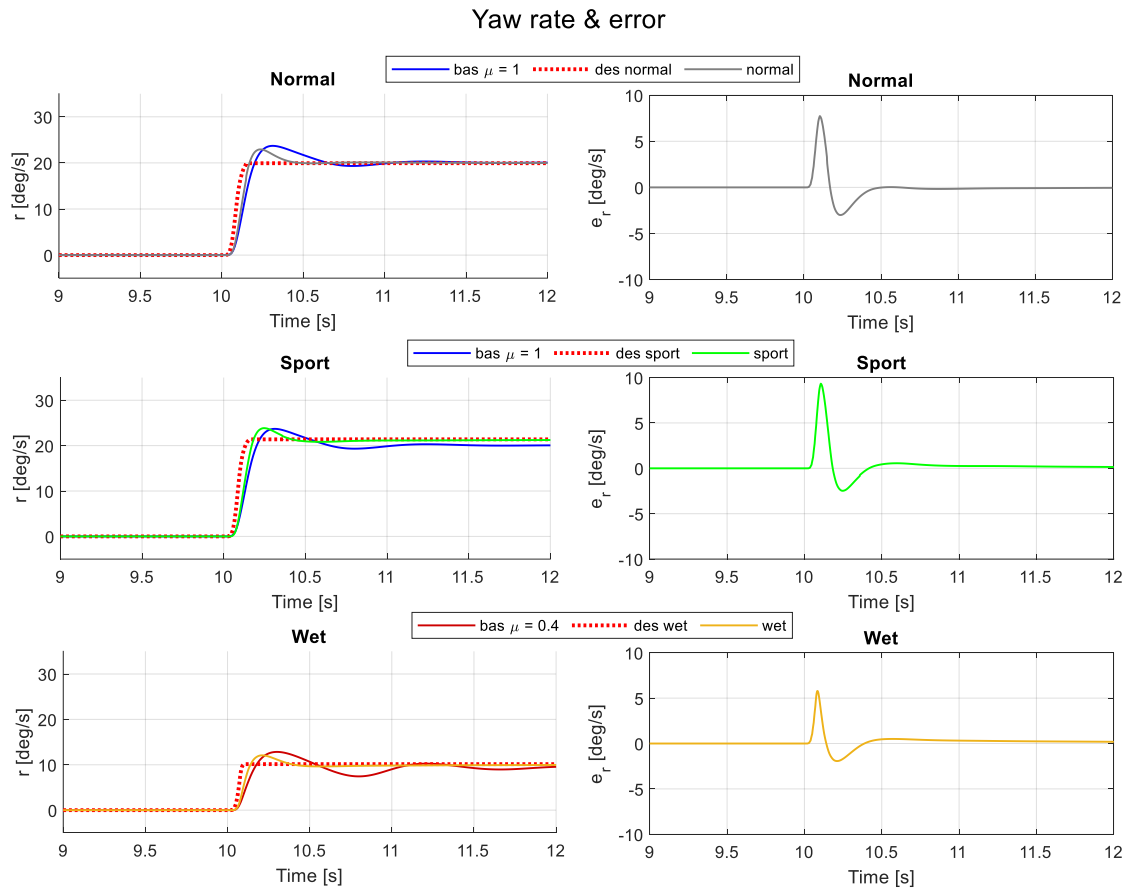


Figure 6.12: Step steer – Yaw rate and error

In Figure 6.12 a remarkable error is observed when the step is imposed. During the ramp steer this was more contained because the steering variation was gradual, a peculiarity of a steady state manoeuvres. The biggest difference is in *Sport* because the reference has a higher value than the other driving modes. Once the transient is passed, the target is followed correctly because the error is zero: since δ_{sw} and v are constant, this is also an expected result.

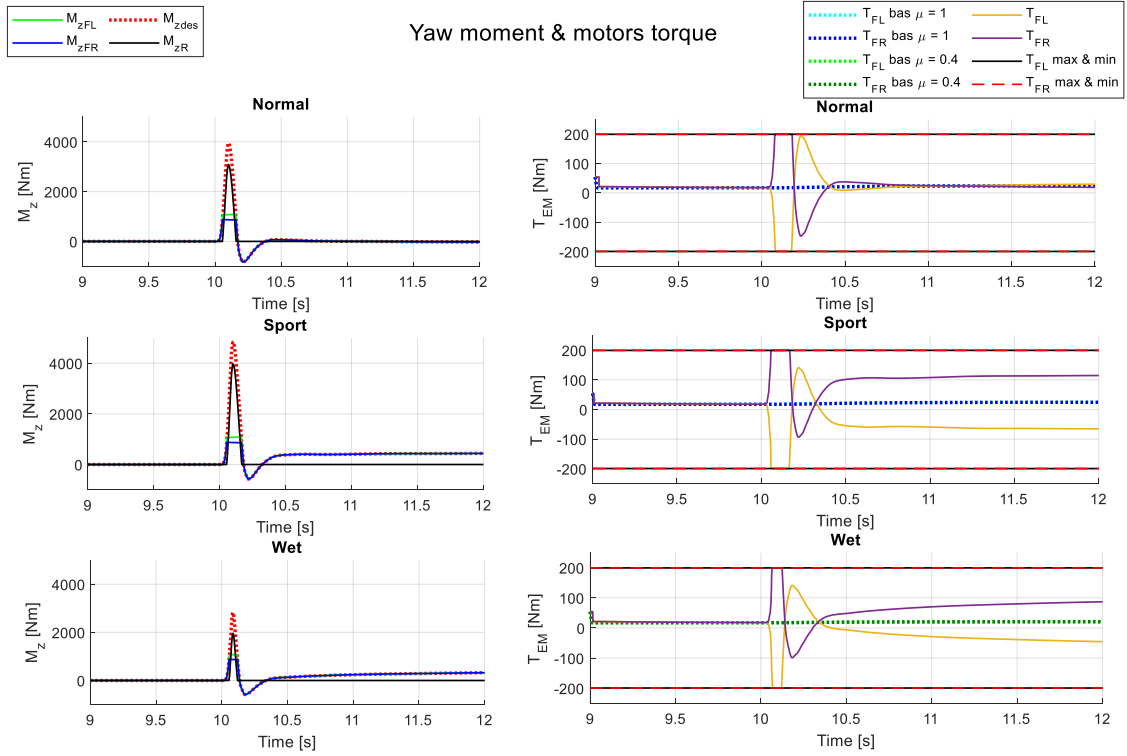


Figure 6.13: Step steer – Yaw moment and electric motors torque

Figure 6.13 shows the results of the control for the front electric motors. The moment M_z has a strong positive peak that saturates the electric motors in every driving mode: it is a predictable result knowing the trend of the yaw rate error. Due to the saturation, it is not possible to exploit all M_{zdes} , indeed the residual quantity is very large as is clear from the value of M_{zR} when the driver applies the steering wheel step (10 s). Later the yaw moment becomes negative as the e_r .

Once the transitory has been overcome, it returns to a steady state condition. In *Normal*, having assigned the understeer characteristic of the passive vehicle, the same torques as for the *Baseline* are obtained. In *Sport* and *Wet* T_{EM} are different from the passive vehicle due to the different K_U^{lin} established for these configurations.

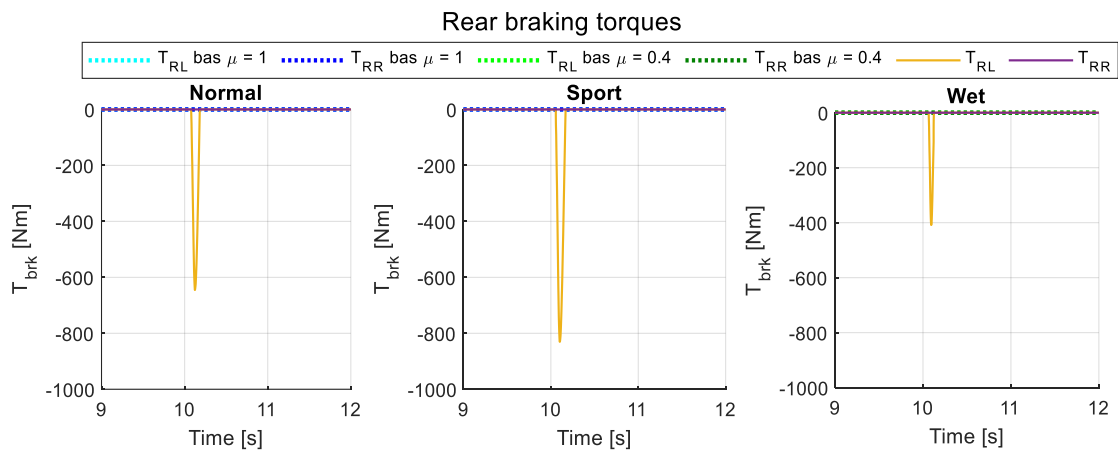


Figure 6.14: Step steer – Rear braking torques

When the steering step is applied, the electric motors saturate: this means that the intervention of the rear brakes is required. In Figure 6.14 it is evident that the braking moment is active only for the left wheel due to the yaw moment convention (if $M_z > 0$ the part to be braked is the internal one). Braking is stronger in *Sport* because M_{zR} is higher.

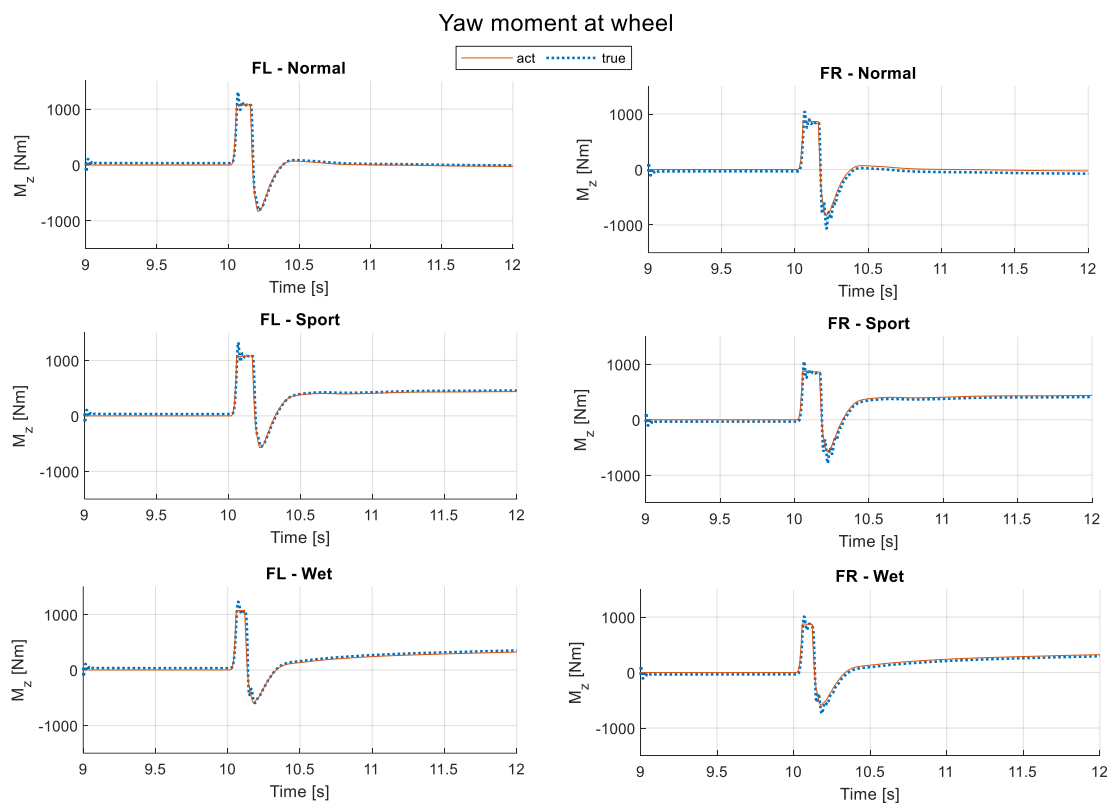


Figure 6.15: Step steer – Comparison between desired and actual yaw moment

In Figure 6.15 $M_{zFj\ true}$ and the one calculated with Equation 6.1 were compared. From the graph it has been examined that the two curves are slightly different at the transient, while they are overlapped in the steady state part (as already verified with the ramp steer).

6.3. Sweep steer

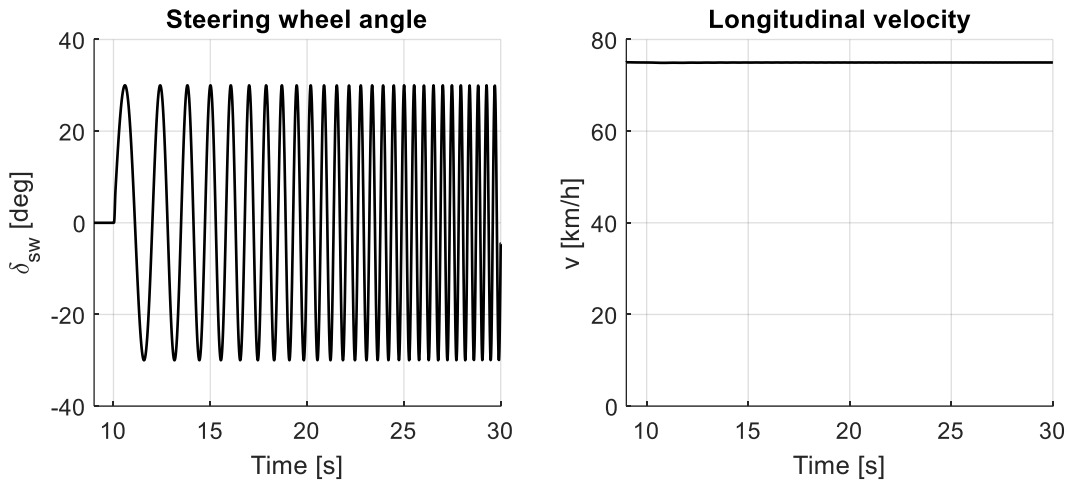


Figure 6.16: Sweep steer – SWA and longitudinal velocity

This test consists in the application of SWA with a sinusoidal signal with constant amplitude, variable frequency and speed kept constant (Figure 6.16). The parameters of the manoeuvre were set are reported in Table 6.2, to obtain $a_y = 0.4 g$ through the first steering input. With this simulation it is possible to evaluate the operation of the control both in transient and for continuous left and right turns.

Table 6.2: Sweep steer – Parameters of the manoeuvre

| Sweep steer | | |
|-------------------|---------------|----------|
| Speed | v | 75 km/h |
| SWA | δ_{sw} | 30 deg |
| Initial frequency | f_I | 0.4 Hz |
| Final frequency | f_F | 3 Hz |
| Frequency rate | f_R | 0.1 Hz/s |

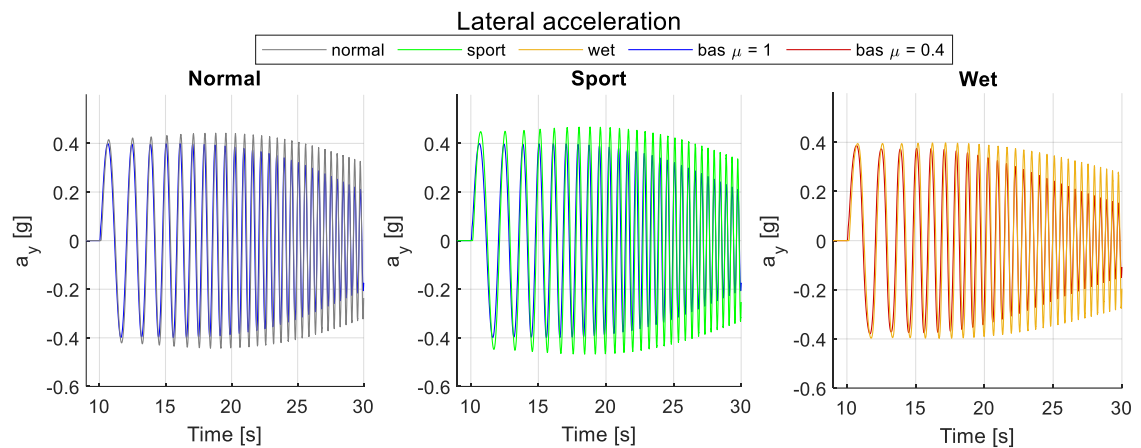


Figure 6.17: Sweep steer – Lateral acceleration

In Figure 6.17 with the passive vehicle, both in high and low grip, lateral acceleration a_y tends to decrease from the value of $\mp 0.4 g$ with increasing frequency, while in *Normal* and *Sport* mode it is possible to reach and overcome this value with the first turns.

In *Wet* position, instead, it is not practicable to maintain this $a_{y_{MAX}}$: the cause is to be attributed to the friction coefficient, since in these conditions $0.4 g$ represents the physical limit that can be get from the vehicle. More generally, from 20 s onwards, a_y also decreases with active control.

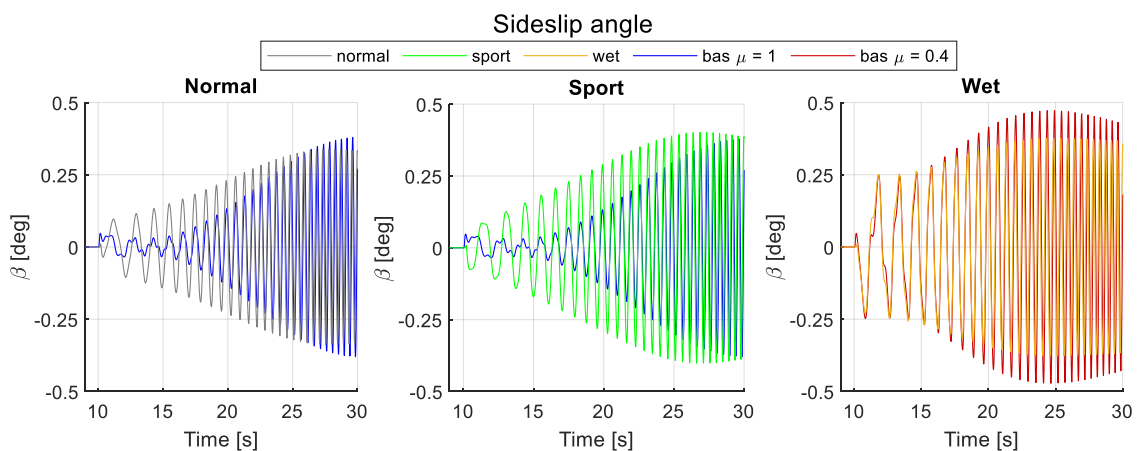


Figure 6.18: Sweep steer – Sideslip angle

The advantage of the TV for the more conservative modes, *Normal* and *Wet*, can be noticed with the variation of the sideslip angle over time (Figure 6.18): this has a more gradual increase with the various turns and a slightly smaller value at the end of the manoeuvre. In *Sport*, on the other hand, it increases compared to the *Baseline*, as already discussed in the other tests carried out.

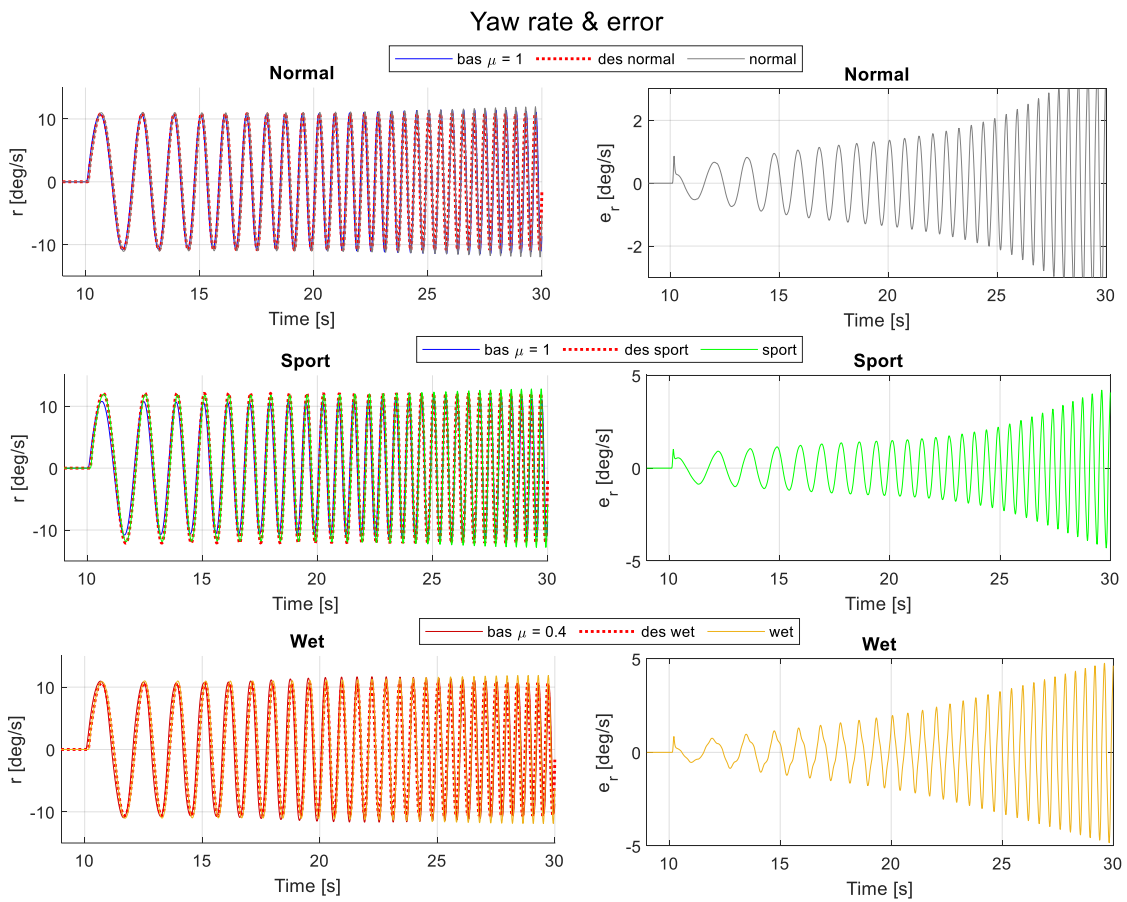


Figure 6.19: Sweep steer – Yaw rate and error

Figure 6.19 shows the yaw rate curves. The reference in *Normal* and *Sport* is followed well at low frequency. After 20 s, when the SWA is changed more quickly, the r exceeds r_{des} because it has difficulty in following it: this is repeated in all driving modes. The confirmation of these remarks is given by the error: initially it is small, but then its amplitude increases over time following the sinusoidal signal seen so far. In absolute value, e_r is greater in *Wet*.

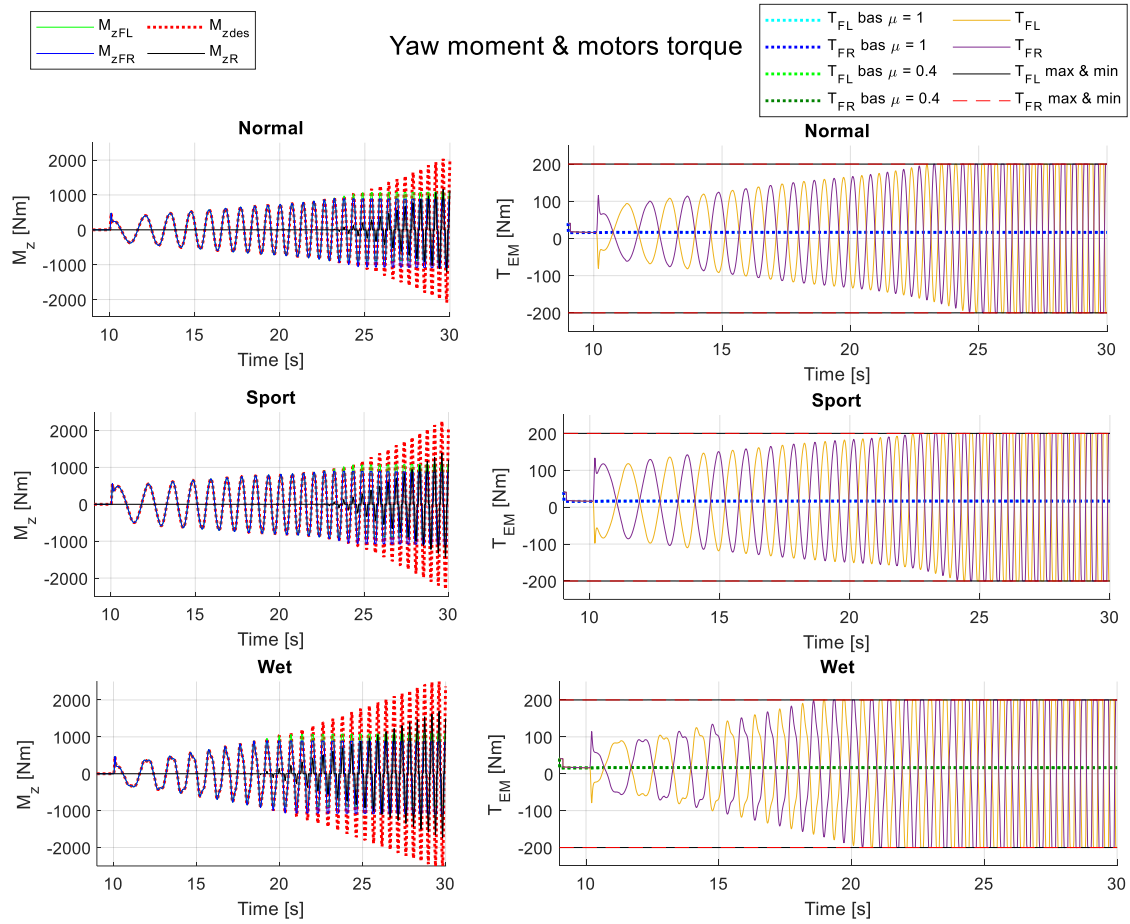


Figure 6.20: Sweep steer – Yaw moment and electric motors torque

The desired yaw moment $M_{z_{des}}$ has the same development as the error (Figure 6.20). The amplitude of this sinusoid increases over time, bringing the electric motors to saturation (after 20 s in *Wet* and about 24 s in *Normal* and *Sport*).

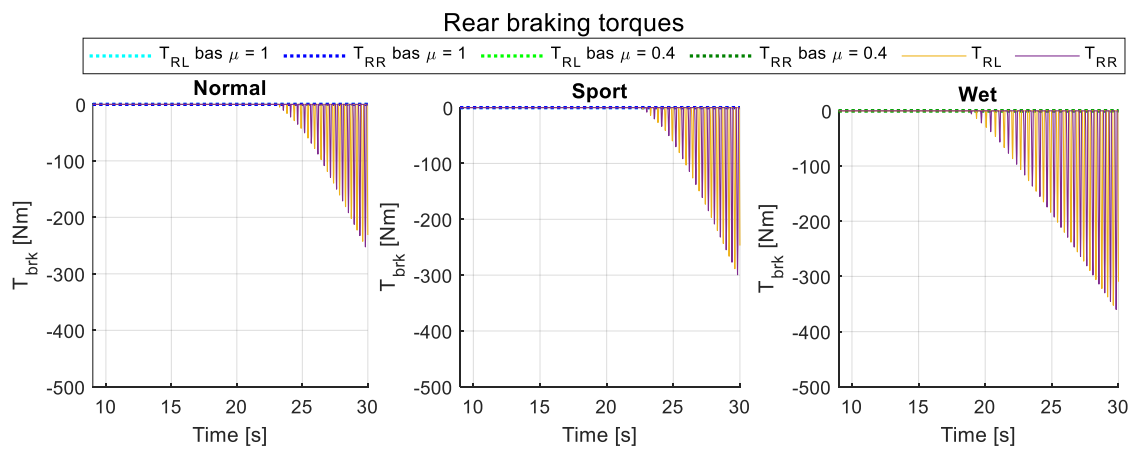


Figure 6.21: Sweep steer – Rear braking torques

At this point the rear brakes come into action (Figure 6.21): their intervention is stronger over time because the yaw moment M_{zR} increases, which cannot be used by the electric motors.

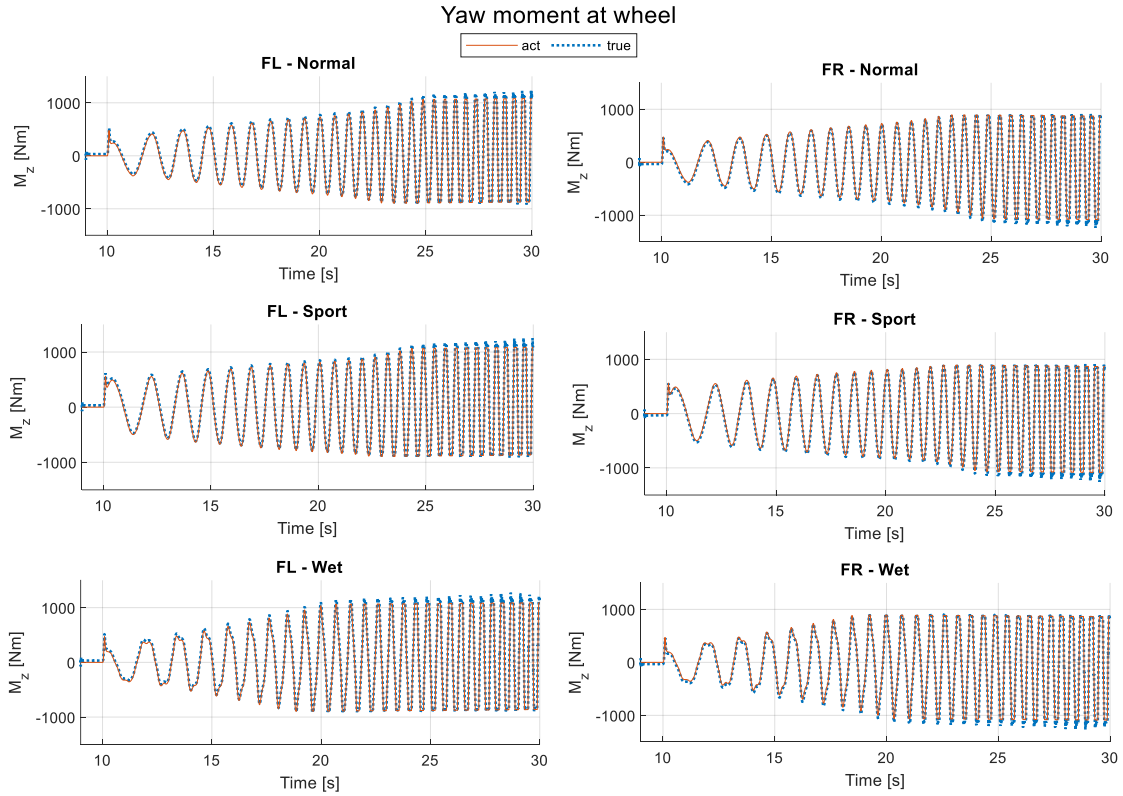


Figure 6.22: Sweep steer – Comparison between desired and actual yaw moment

Despite these continuous left and right turns, the yaw moment on both wheels is effectively delivered as the $M_{Fj act}$ curve is overlapped with $M_{Fj true}$ (Figure 6.22).

6.4. PowerOn on cornering

The purpose of the powerOn on cornering (PON) is to evaluate the response of the vehicle during cornering to a variable longitudinal acceleration. It is characterized by:

- A straight phase where a target speed $v = 60 \text{ km/h}$ is reached;
- A curvilinear section with the imposition of a certain SWA maintaining the previous velocity;

- A part where the driver applies a throttle step, after the car has stabilized during cornering.

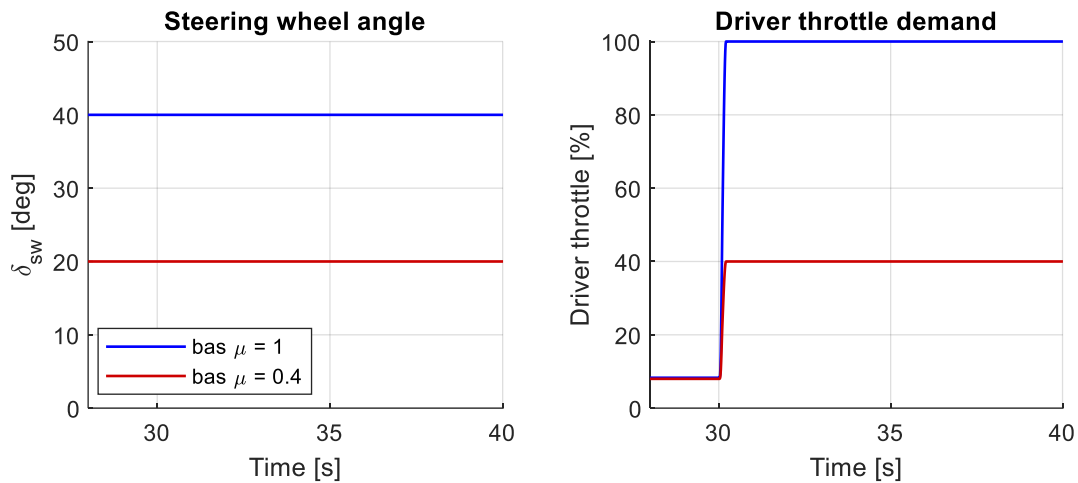


Figure 6.23: PowerOn on cornering – SWA and driver throttle demand

From Figure 6.23 it is possible to extract the PON parameters in the various versions: in high grip. Therefore, in *Normal* and *Sport* the final SWA is $\delta_{sw} = 40 \text{ deg}$ and the acceleration request is 100%. In *Wet* $\delta_{sw} = 20 \text{ deg}$ and the throttle is at 40%.

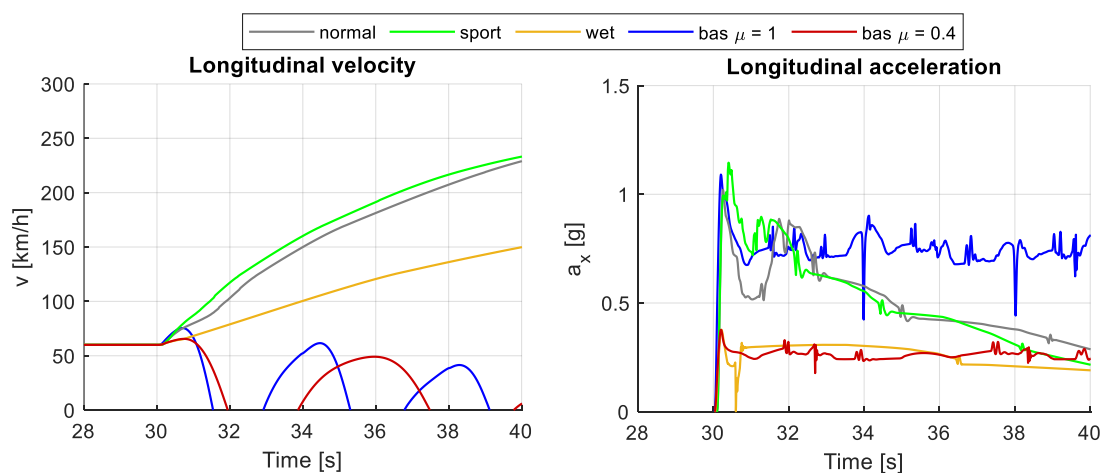


Figure 6.24: PowerOn on cornering – Longitudinal velocity and acceleration

Figure 6.24 shows the speed and longitudinal acceleration trend of the vehicle. After reaching 60 km/h (and consequently $a_x = 0$), the throttle step is applied and a different behaviour is noted between the passive vehicle and the one in *Normal* and *Sport*:

- in the first case, despite the acceleration pedal being pressed all the way down, the speed cannot be increased and there are oscillations of v and a_x ;
- with the control running, the car has a progressive increase in speed without exhibiting irregular action.

In *Wet* there is a lower speed of about 80 km/h compared to the maximum of the other two positions. The longitudinal acceleration is also less.

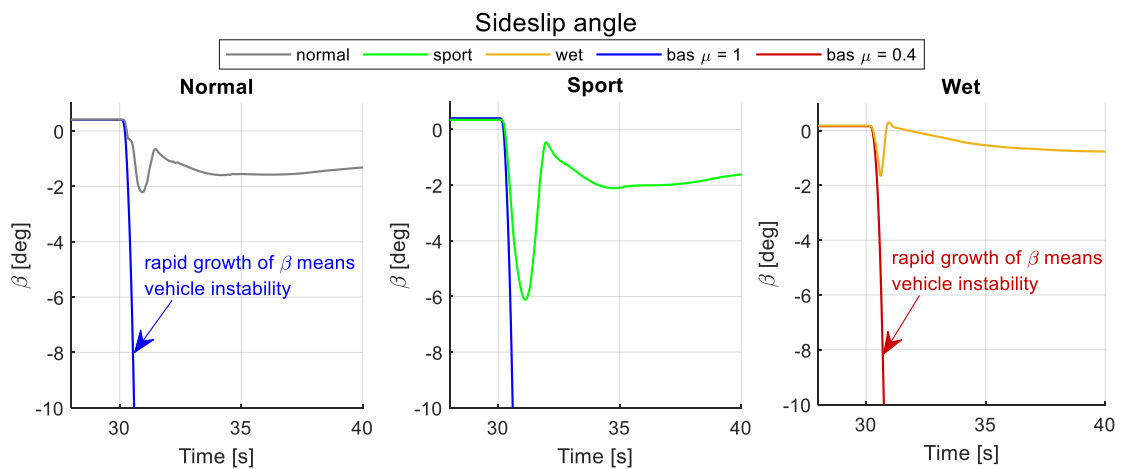


Figure 6.25: PowerOn on cornering – Sideslip angle

The previous speed oscillations in passive vehicle are explainable by the sideslip angle graph (Figure 6.25): when the driver accelerates at 30 s , β assumes very high values in *Baseline* (about $\mp 180 \text{ deg}$). This means that the driver has lost control of the car, while with the TV active the sideslip angle it has more contained numbers, never exceeding -2 deg in *Normal/Wet* and -6 deg in *Sport*.

In Figure 6.26 the trajectory of the vehicle and the trend of lateral acceleration are plotted. Up to 10 s the car travels in a straight line, then in the next 20 s it starts to turn left with a constant SWA (consequently a_y is constant). When the acceleration step is applied, the passive vehicle no longer follows the previous trajectory but undergoes unwanted changes of direction, confirmed by the change in sign of the lateral acceleration: this is another index of loss of stability.

Instead, with the TV active, the trajectory is maintained and a_y gradually reaches the value of $1g$: this is consistent with the increase in vehicle speed. Finally, it is noteworthy that the trajectory in *Sport* is tighter: therefore, correctly the vehicle has a more oversteer behaviour. In *Wet* the trajectory is wider because the imposed SWA is lower (consequently also the lateral acceleration).

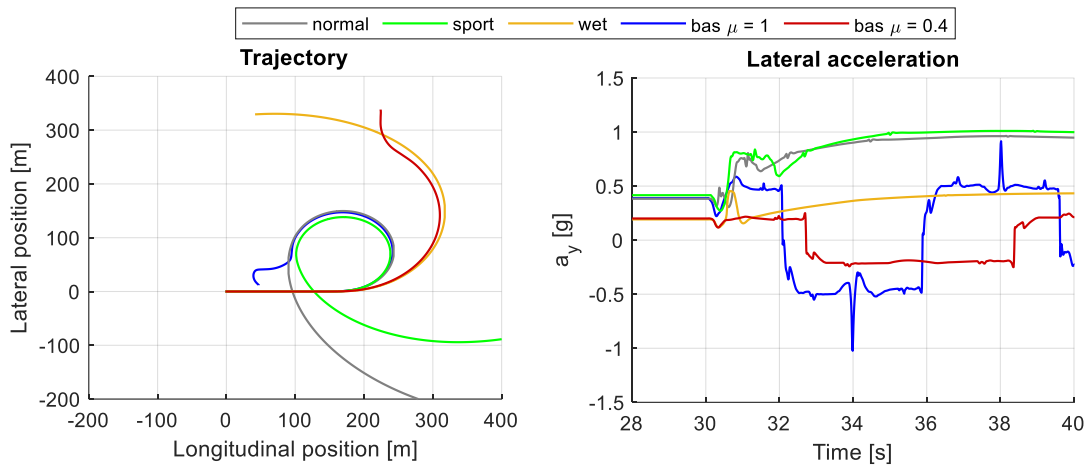


Figure 6.26: PowerOn on cornering – Trajectory and lateral acceleration

When $a_x \neq 0$, even the yaw rate (Figure 6.27) has values in *Baseline* that exceed the recommended range in [23]. In particular, the yaw rate is first positive, then negative and finally positive again: this is congruent with the trajectory in Figure 6.26 because the car first oversteers and then understeers. With the TV, on the other hand, after the transient due to the throttle step, r_{des} is practically superimposed on the current r .

The error remains approximately zero because the steering step is set slowly and therefore the reference is followed well. In the part where the throttle is applied, e_r initially assumes a value strongly negative, then positive and finally returns to zero again.

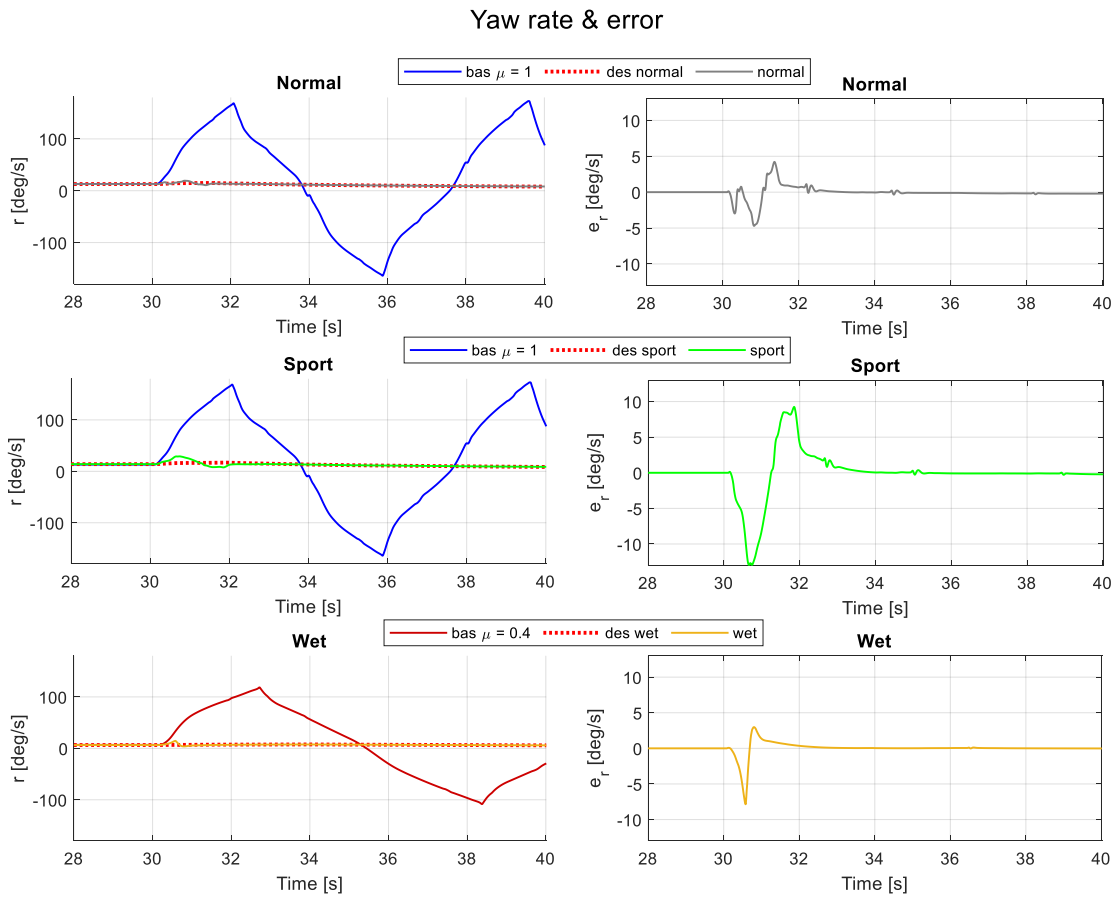


Figure 6.27: PowerOn on cornering – Yaw rate and error

The trend of the yaw moment M_z follows exactly that of the error until the latter becomes different from zero (Figure 6.28). Subsequently M_z it is slightly different from e_r due to the integral gain that recalls the “history” of the error.

As in the step steer manoeuvre, when $\delta_{sw} \neq 0$ the motor torques vary with respect to those delivered in *Baseline* for the action of M_z . In the section where the car is accelerating, unlike the passive vehicle, the torques are not the same but assume such values to follow the reference and execute the desired trajectories (for example, more oversteer in *Sport*).

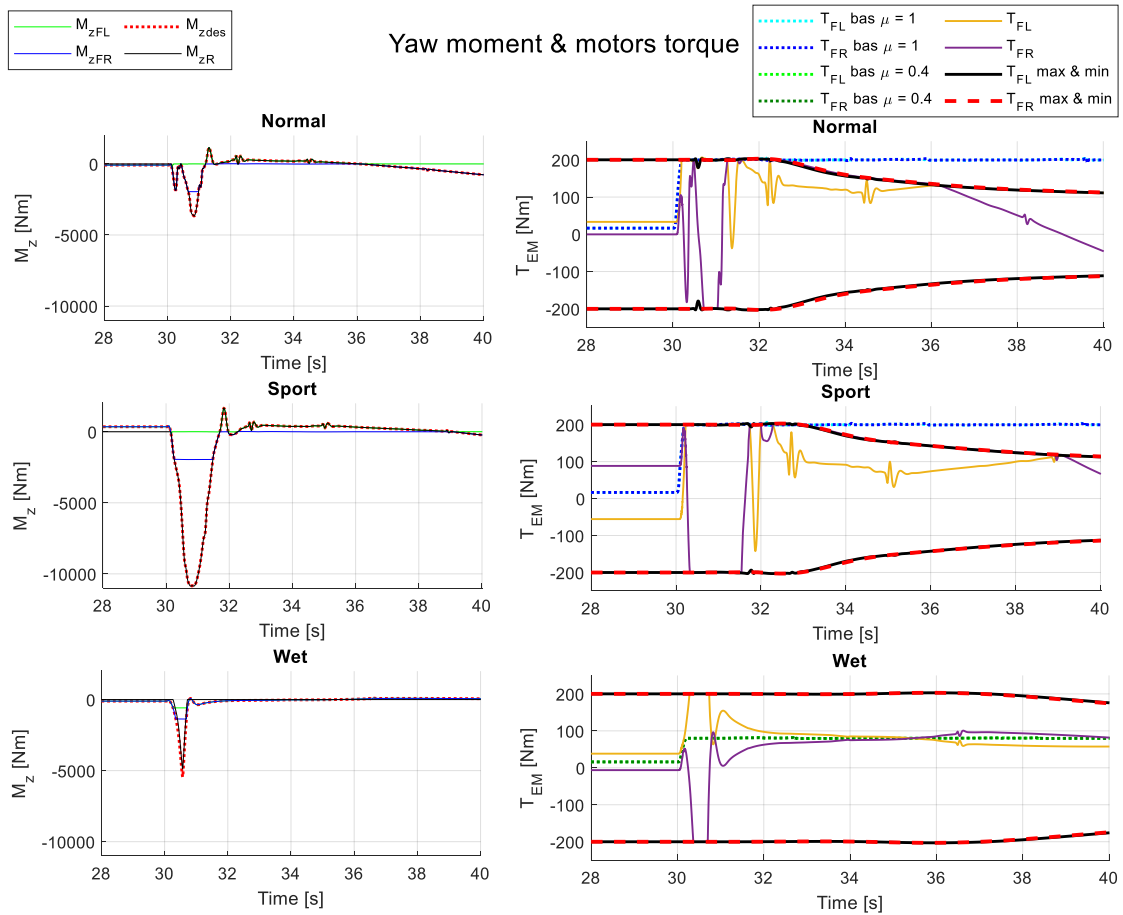


Figure 6.28: PowerOn on cornering – Yaw moment and electric motors torque

Another aspect that can be noticed is that the maximum and minimum torques of the electric motors, in *Normal* and *Sport*, become lower with the request of 100% throttle. This is due to the increase in the angular speed of the electric motors (Figure 6.29): the motor map imposes a lower torque than ω_{EM} .

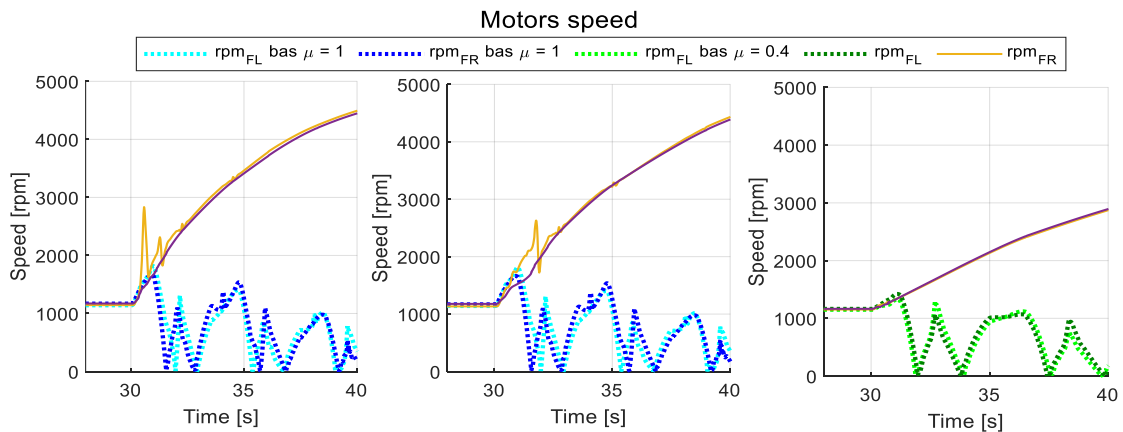


Figure 6.29: PowerOn on cornering – Electric motors speed

Figure 6.30 shows the braking torques of the rear: the brakes are correctly active when the electric motors are in saturation. The activated rear brake is that of the side where there is a negative torque demand.

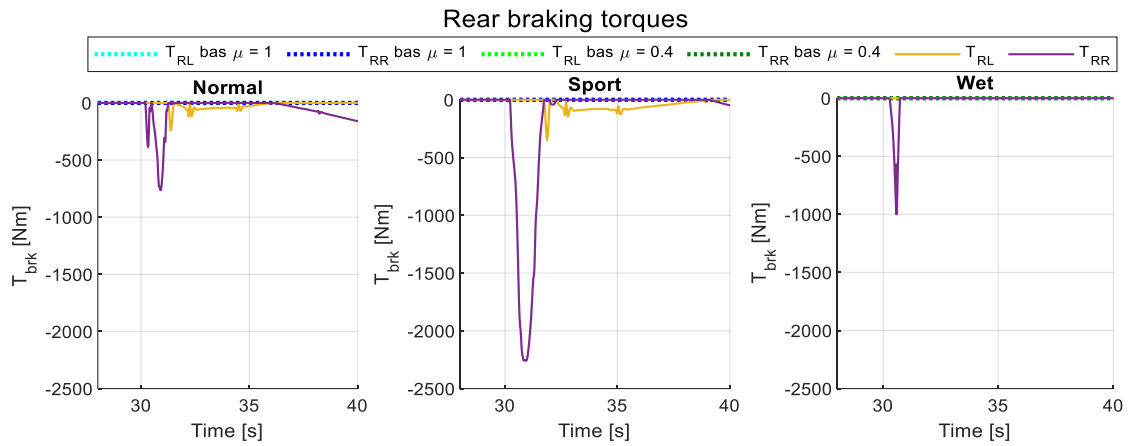


Figure 6.30: PowerOn on cornering – Rear braking torques

Unlike the previous manoeuvres, when the longitudinal acceleration becomes different from zero here it is more difficult to guarantee $M_{zFj act}$ (Figure 6.31).

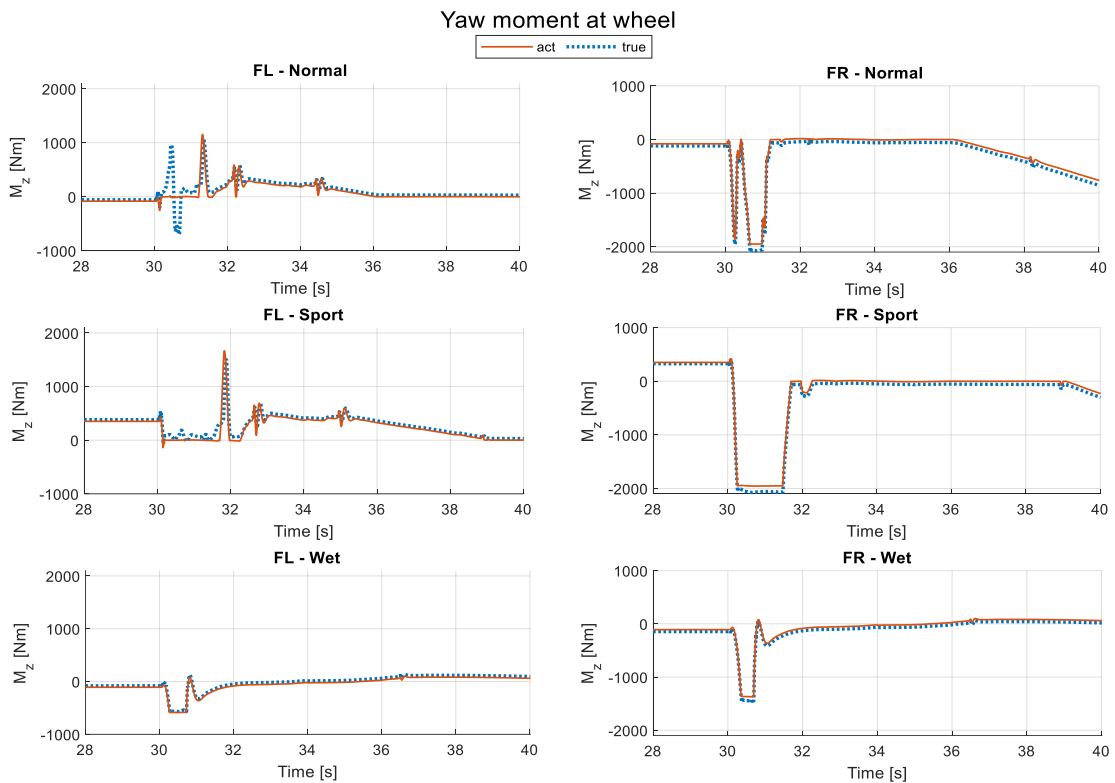


Figure 6.31: PowerOn on cornering – Comparison between desired and actual yaw moment

6.5. Braking in turn

The goal of the braking in turn (BIT) is to examine the effect of sudden braking during a curve, therefore with negative longitudinal acceleration.

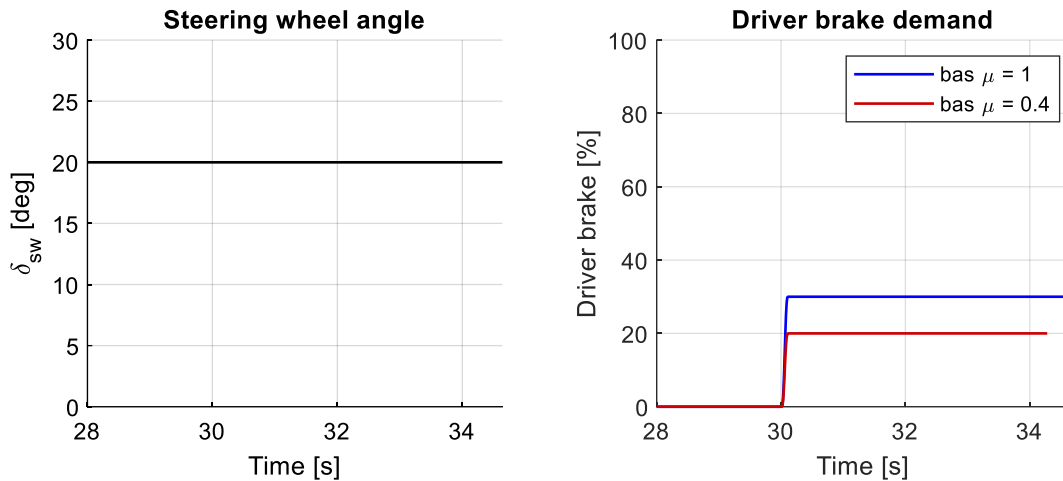


Figure 6.32: Braking in turn – SWA and driver brake demand

The test can be divided into:

- A straight part where a speed of 120 *km/h* is reached in high grip and 70 *km/h* with $\mu = 0.4$;
- A curved portion with the imposition of SWA $\delta_{sw} = 20 \text{ deg}$ and maintaining the previous velocity;
- After the car has stabilized in the corners, a phase where the driver applies a braking step of 30 % in *Normal* and *Sport* and 20 % in *Wet* (Figure 6.32).

The simulation is stopped when the speed is below 10 *km/h*.

In Figure 6.33 are indicated the longitudinal velocity and acceleration. During braking, the deceleration that the vehicle undergoes is constant with the active control, while it is irregular in *Baseline* (there is an overshoot that lowers the deceleration).

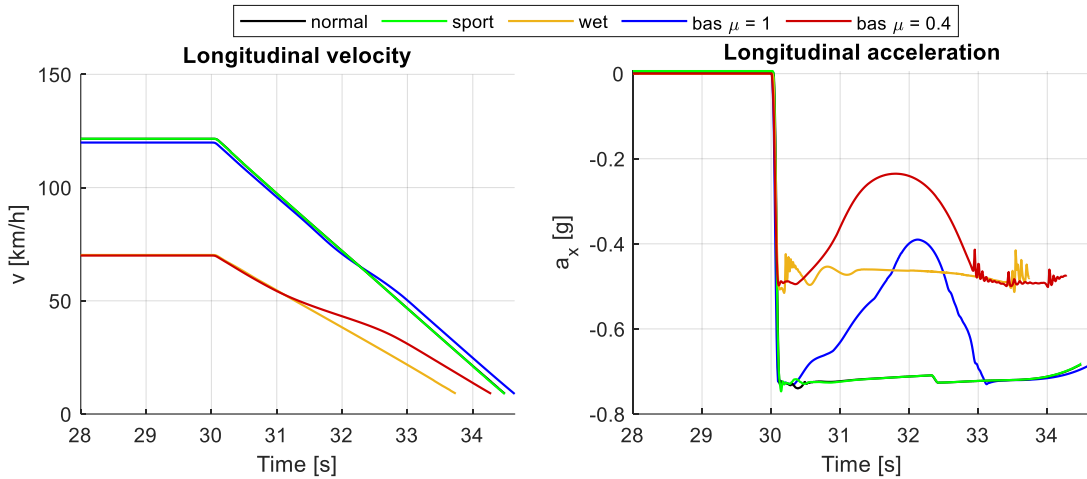


Figure 6.33: Braking in turn – Longitudinal velocity and acceleration

The justification for this anomalous behaviour of the a_x can be found in the sideslip angle: in Figure 6.34 there is a peak of β in *Baseline* which is attenuated by the activation of the control.

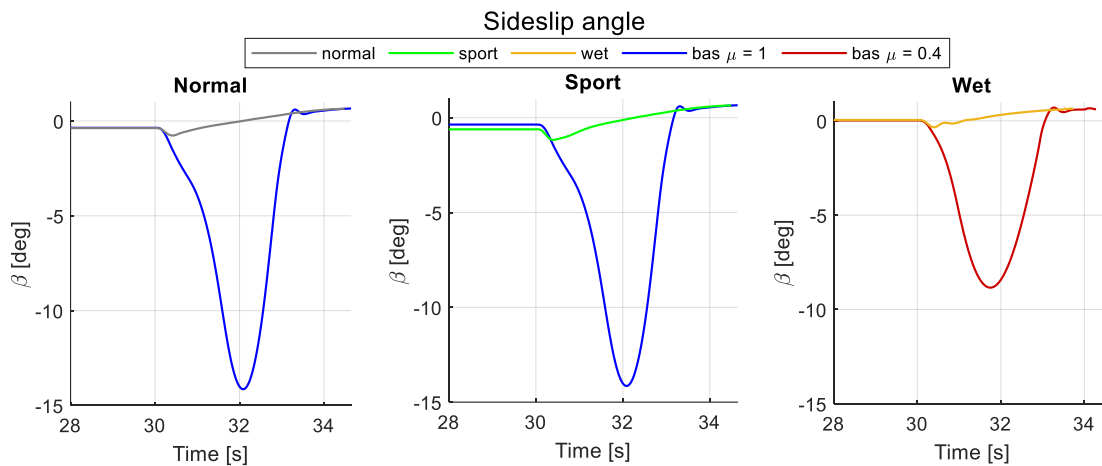


Figure 6.34: Braking in turn – Sideslip angle

Like the sideslip angle, the yaw rate (Figure 6.35) also has overshoots in correspondence with the braking request, which are then dampened by the TV. In *Wet* configuration r decrease due to the lower velocity at the start of the manoeuvre.

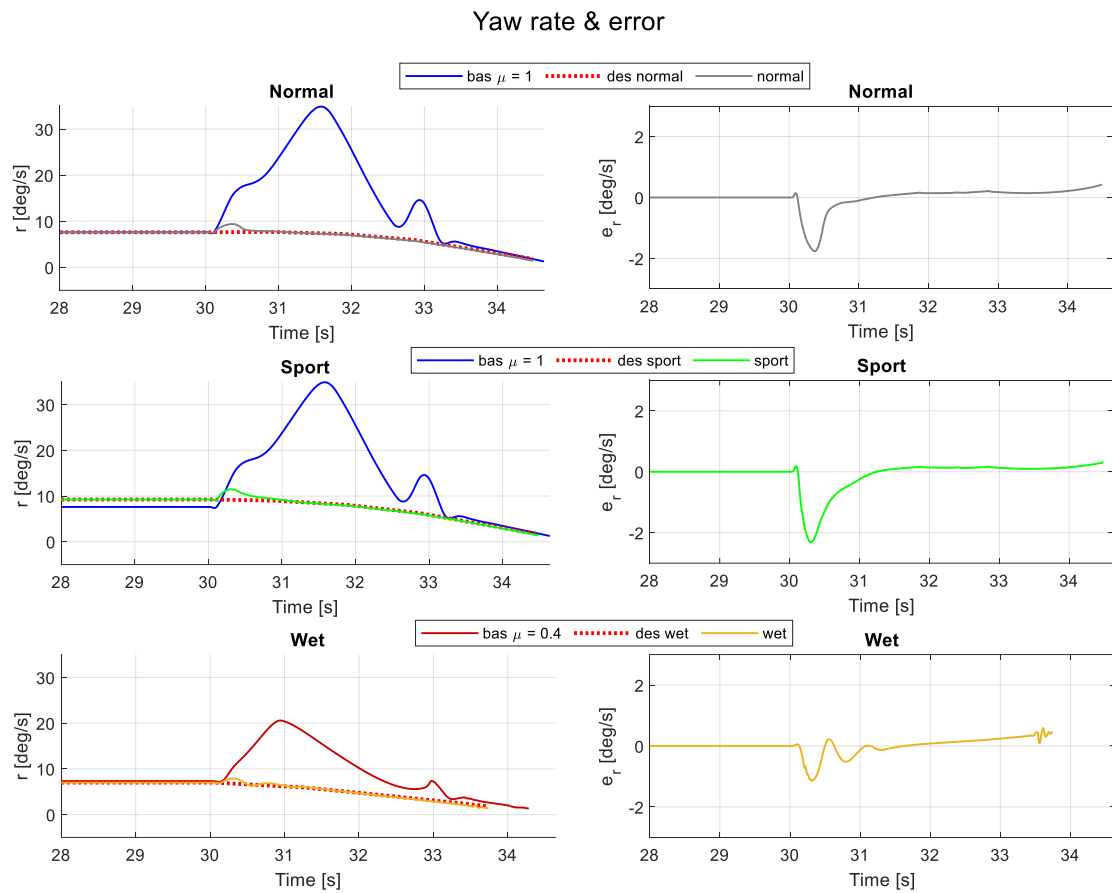


Figure 6.35: Braking in turn – Yaw rate and error

The peaks just highlighted lead to an increase in lateral acceleration and a slightly oversteer effect of the passive vehicle, as seen from the trajectory in *Baseline* (Figure 6.36). All these trends are attenuated with control.

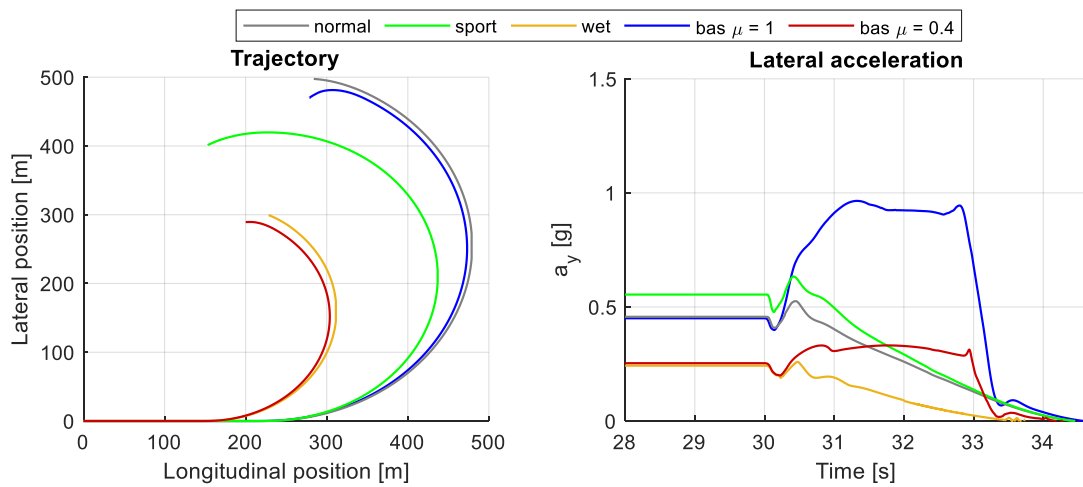


Figure 6.36: Braking in turn – Trajectory and lateral acceleration

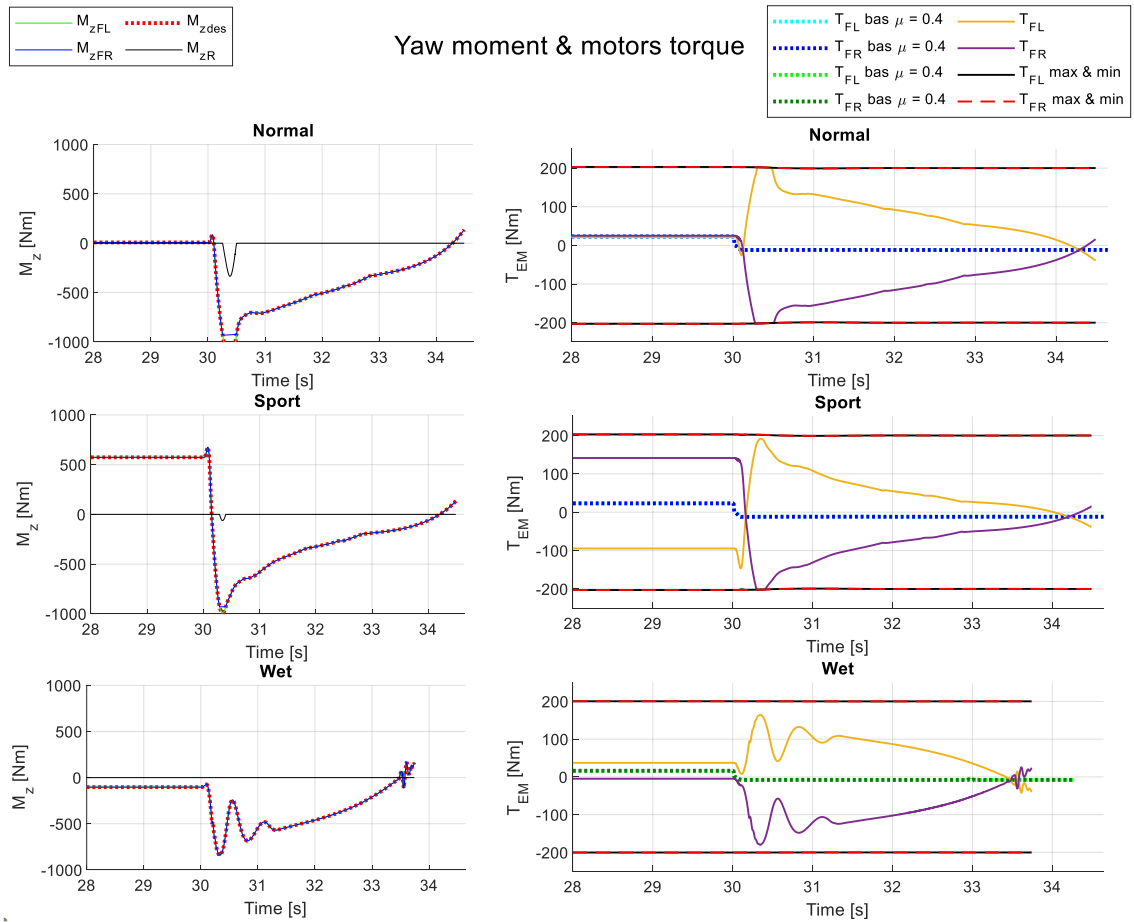


Figure 6.37: Braking in turn – Yaw moment and electric motors torque

If there is no driver braking, the yaw moment plot is similar to what has already been seen with the PON manoeuvre. After 30 s this braking is applied and, in all modes, M_z becomes negative because there is oversteer with respect to the reference: so more torque is supplied to the inner (left) wheel and less to the outer (right) one, in an attempt to correct oversteer (Figure 6.37).

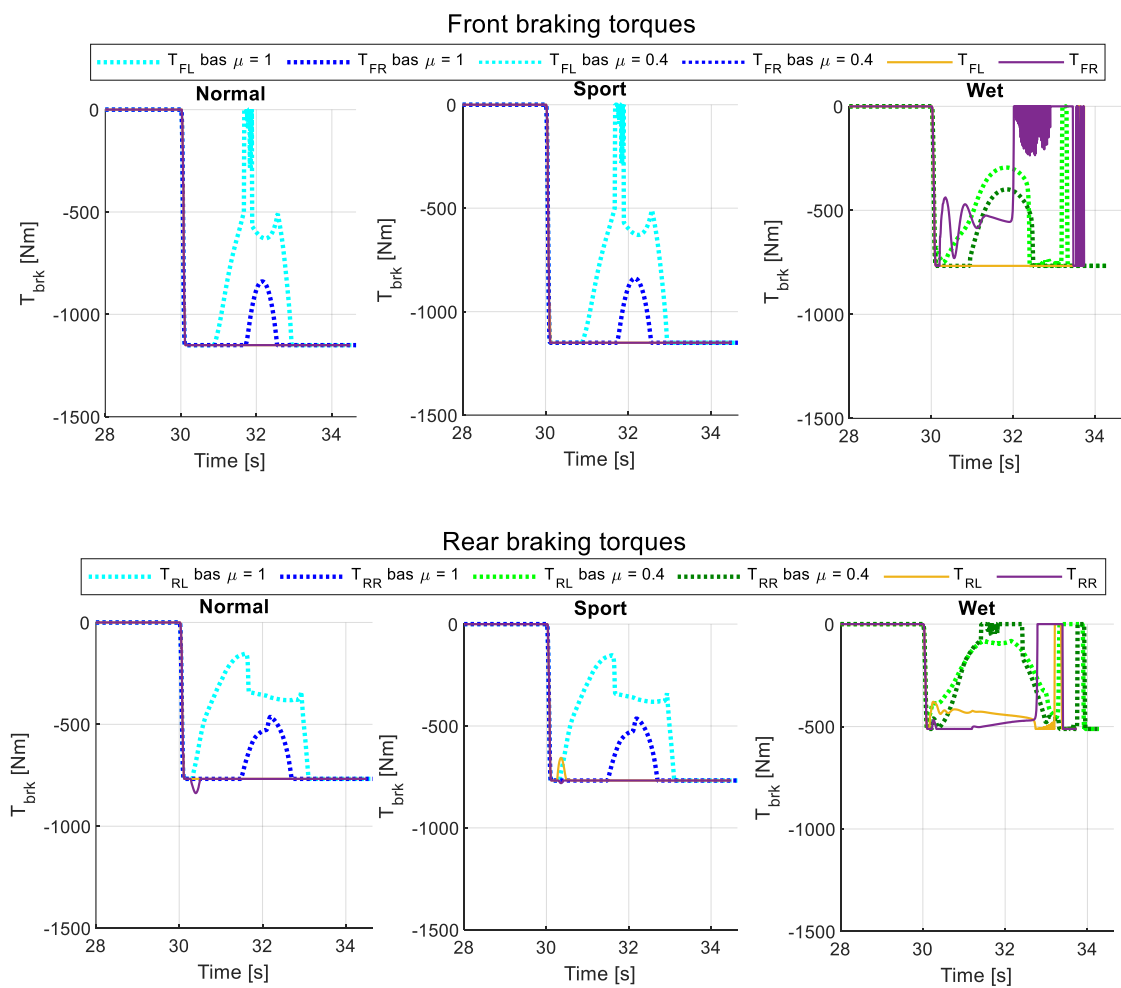


Figure 6.38: Braking in turn – Braking torques

Having pressed the brake pedal, in this manoeuvre there are braking torques on the wheels of both axles (Figure 6.38).

At the front, even if there is no direct intervention of the control, the braking torque with the TV becomes constant and does not have an irregular stretch like in *Baseline*. In *Wet* mode the torque, on the other hand, remains irregular due to the intervention of the ABS.

The reasoning just expressed also applies to the rear but must be considered that here the control actively intervenes and further brakes one of the two wheels, choosing it with the criteria explained in paragraph 5.3.2.

Despite the noticeable improvements due to the TV strategy in this BIT manoeuvre, the yaw moment calculated in the *HLC* is not correctly delivered to the wheels when the driver applies the braking step (Figure 6.39).

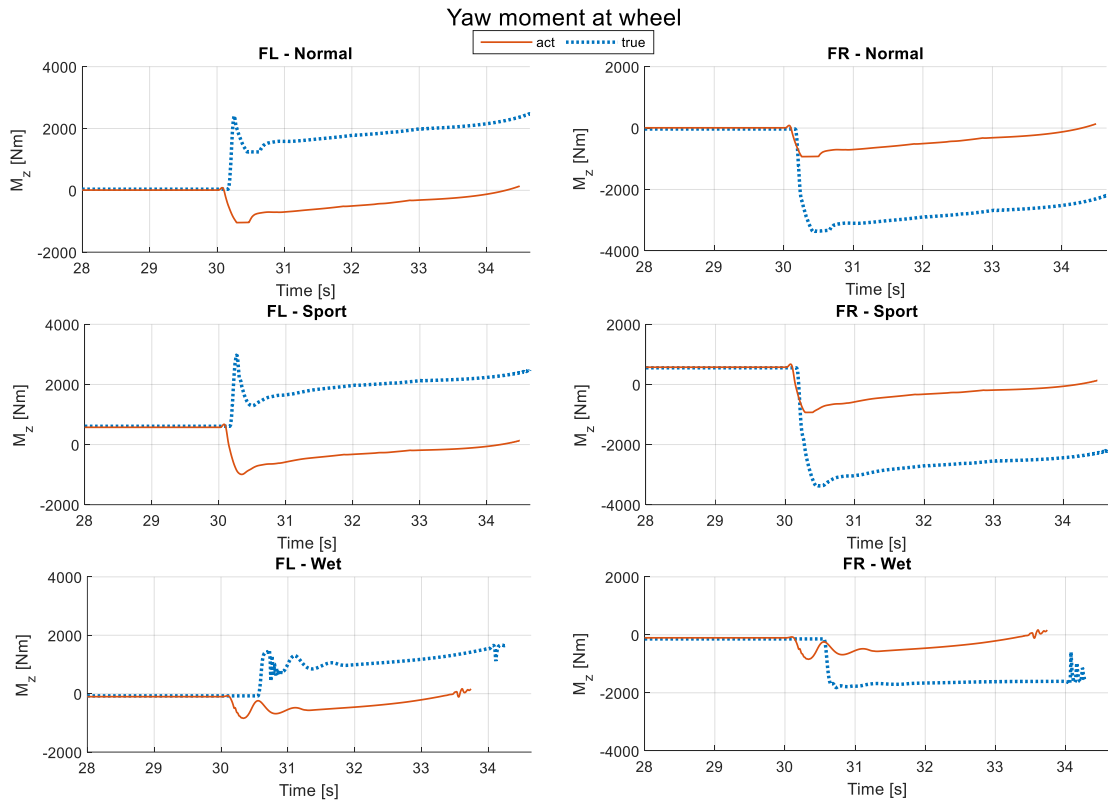


Figure 6.39: Braking in turn – Comparison between desired and actual yaw moment

7. Conclusions

Recent developments in the automotive world are focused both on making cars more sustainable, from an environmental point of view, and more efficient, in terms of performance and safety. The present thesis work concerned the construction of a torque-vectoring (TV) system applied to an All-Wheel-Drive (AWD) hybrid vehicle, formed by two electric motors on the front wheels and an internal combustion engine (ICE) on the rear axle. The use of independent electric motors encompasses the aspects just mentioned and allows for a TV logic, which improves the response of the car mainly in lateral dynamics.

The key point of this project was the *reference generator (RG)*, one of the three macro systems of a typical TV structure: here the desired set point is produced, i.e. the yaw rate, which intrinsically corresponds to a certain understeer characteristic. Through this diagram it was possible to analyse the car's cornering behaviour: the one resulting from the passive vehicle (*Baseline*) was modified by integrating three different driving modes (*Normal*, *Sport* and *Wet*) into the same control algorithm. The targets of each configuration were established with several parameters of the experimental formula of the understeer characteristic.

The *RG* must provide a solution consistent with two other macrosystems, the *high level controller (HLC)* and the *low level controller (LLC)*. The yaw moment M_z , generated through the proportional-integral (PI) of the *HLC*, is distributed to the front electric motors by varying the torque on each wheel (this is the “torque-vectoring”) but, if one of the two saturates, the rear brakes are also activated.

The effectiveness of the TV was evaluated through numerical tests, with the co-simulation between VI-CRT and Simulink. Ramp steer, step steer, sweep steer, powerON on cornering (PON) and braking in turn (BIT) were the manoeuvres performed: these are open loop tests, therefore objectively repeatable, which brought the TV to its limit in various conditions.

In steady state simulations, as desired, identical action with respect to the passive vehicle was obtained in *Normal* and *Wet*. In *Sport* for low lateral accelerations a_y the car submits higher performance, i.e. a lower steering wheel angle (SWA) is required to achieve the same a_y as the *Baseline*.

In transient manoeuvres, the presence of a reference helped the active vehicle to eliminate oscillations and reduce overshoots in terms of a_y and sideslip angle β : thus, greater stability was ensured, which was impossible to obtain with high values in *Baseline*. The settling time was also reduced, which means a faster response of the car. The absolute value of β is larger in *Sport* but is a desirable feature of this driving mode. Even for non-zero longitudinal accelerations, the presence of a TV has led to profits on vehicle stability: in addition to the β , it is evident from the regularization of the speed, in the PON manoeuvre, and of the deceleration, in the BIT test.

In conclusion, the realization of a control system able to distribute torque between the two sides of the car has brought clear benefits both in terms of lateral dynamics and active safety.

7.1. Future works

The adoption of some simplifying hypotheses and the lack of time allow room for improvement discussed below.

The simulations performed at $a_x \neq 0$ have certainly given some progress, but it has not been possible to take full advantage of the TV, as was clear from Figure 6.31 and Figure 6.39. In the *RG* an analytical formula based on experimental tests was used to produce the desired yaw rate maps and the parameters of these equations were obtained from stationary simulations on the passive vehicle. For non-zero longitudinal accelerations, it would have been more appropriate to exploit a quasi-static model [20]: based on the intended objective, this theory allows to calculate analytically the understeer characteristic and to procure the consequent look-up tables.

As discussed in paragraph 4.2, different choices might have been preferred for the other two macro systems. In the *HLC* another type of controller could bring some improvements, in particular if several variables were to be controlled simultaneously [14]. In the *LLC* the torque allocation took place without introducing coefficients, but optimization algorithms such as in [20] could help with consumption, especially if one were to consider a real battery of not infinite capacity.

In a virtual vehicle model, all the outputs are known: in a real one, however, some of these would require very expensive sensors. To enable the implementation of the TV, these parameters can be estimated: for example, the forces acting on the wheels, sideslip angle β and friction coefficient μ . The knowledge of the latter two could lead to the addition of further control logics: above all μ that has been hypothesized in this thesis.

Finally, before commercializing such a control logic it is necessary to test the TV on the road. With numerical simulation projects can be evaluated quickly and economically, but these software do not represent reality and some aspects are neglected. Preliminarily, further tests could be carried out on a driving simulator: in this phase, extra adjustments to the control can be made by exploiting the sensors present and the driver's feedback.

Acknowledgments

All the activity was carried out in a difficult historical period. Despite the problems due to the unexpected worldwide pandemic, the DIMEAS research group gave me the opportunity to undertake this work in collaboration with the Danisi Engineering company.

For this I want to thank prof. Alessandro Vigliani for the opportunity and his technical support throughout the thesis period, with the invaluable help of the engineer Antonio Tota. From the staff of *Danisi Engineering* (Nichelino, Torino, Italy) I thank the engineer Salvatore Calanna, who followed me daily on the experimental side and who, together with the engineer Claudio Ricci, helped me to grow professionally. Finally, I want to thank all the people in the Advanced Vehicle Dynamics (AVD) department and the other undergraduates with whom I shared this experience: even from them there was never lack of help when it was needed.

Bibliography

- [1] J. D. Setiawan, M. Safarudin, A. Singh, «Modeling, simulation and validation of 14 DOF full vehicle model,» International Conference on Instrumentation, Communication, Information Technology, and Biomedical Engineering 2009.
- [2] S. Sulaiman, P. M. Samin, H. Jamaluddin, R. A. Rahman, «Modeling and Validation of 7-DOF Ride Model for Heavy Vehicle,» International Conference on Automotive, Mechanical and Materials Engineering ICAMME'2012.
- [3] T. Gillespie, «Fundamentals of Vehicle Dynamics,» Warrendale: SAE, 1992.
- [4] M. Velardocchia, E. Galvagno, «Appunti di fondamenti di Meccanica del Veicolo,» 2019.
- [5] T. Goggia, A. Sorniotti, L. De Novellis, A. Ferrara, «Torque-vectoring Control in Fully Electric Vehicles via Integral Sliding Modes,» American Control Conference 2014.
- [6] H. B. Pacejka, «Tyre and Vehicle Dynamics,» Oxford: Butterworth-Heinemann, 2002.
- [7] W. F. Milliken, D. L. Milliken, «Race Car Vehicle Dynamics,» Warrendale: SAE, 1995.
- [8] «VI-CarRealTime 19.0 Documentation».
- [9] Racing Brembo, «Catalogue brake systems,» 2015-2016. [Online]. Available: https://www.brembo.com/de/Varie/Brembo_RacingAutoCatalogue.pdf.

-
- [10] «Torque vectoring - Wikipedia,» [Online]. Available: https://en.wikipedia.org/wiki/Torque_vectoring#cite_note-2.
- [11] A. Tota, «Integration of Active Systems for a Global Chassis Control Design,» 2017.
- [12] L. De Novellis, A. Sorniotti, P. Gruber, «Design and Comparison of the Handling Performance of Different Electric Vehicle Layouts,» Proceedings of the Institution of Mechanical Engineers, Part D: Journal of Automobile Engineering 228.2, 2014.
- [13] L. De Novellis, A. Sorniotti, P. Gruber, A. Pennycott, «Comparison of Feedback Control Techniques for Torque-Vectoring Control of Fully Electric Vehicles,» IEEE Transactions on Vehicular Technology 63.8, 2014.
- [14] G. Kaiser, «Torque Vectoring - Linear Parameter-Varying Control for an Electric Vehicle,» Verlag Dr. Hut München, 2015.
- [15] A. Mangia, «Torque vectoring control strategies for electric vehicles with multiple motors,» 2018-2019.
- [16] L. De Novellis, A. Sorniotti, P. Gruber, «Driving modes for designing the cornering response of fully electric vehicles with multiple motors,» Mechanical Systems and Signal Processing, 64:1–15, 2015.
- [17] B. Lenzo, A. Sorniotti, P. Gruber, K. Sannen, «On the experimental analysis of single input single output control of yaw rate and sideslip angle,» International Journal of Automotive Technology, 18(5):799–811, 2017.
- [18] L. De Novellis, A. Sorniotti, P. Gruber, L. Shead, V. Ivanov, K. Höpping, «Torque Vectoring for Electric Vehicles with Individually Controlled Motors: State-of-the-Art and Future Developments,» 26th Electric Vehicle Symposium. 2012.

-
- [19] M. Mondek, «Active torque vectoring systems for electric drive vehicles,» 2018.
- [20] L. De Novellis, A. Sorniotti, P. Gruber, «Optimal Wheel Torque Distribution for a Four-Wheel-Drive Fully Electric Vehicle,» SAE Int. J. Passeng. Cars - Mech. Syst. 6(1):2013.
- [21] ISO, «Passenger cars — Steady-state circular driving behaviour — Open-loop test methods,» ISO 4138:2012.
- [22] I. Karogal, B. Ayalew, «Independent Torque Distribution Strategies for Vehicle Stability Control,» 2009.
- [23] ISO, «Road vehicles — Lateral transient response test methods — Open-loop test methods,» ISO 7401:2011.